

March 2022

THE ROLE OF EXTRACELLULAR POLYMERIC SUBSTANCES IN THE ACCUMULATION AND TRANSPORT OF POLYSTYRENE NANOPARTICLES IN BIOFILMS

Joann Marie Rodríguez Suarez
University of Massachusetts Amherst

Follow this and additional works at: https://scholarworks.umass.edu/dissertations_2



Part of the [Environmental Engineering Commons](#)

Recommended Citation

Rodríguez Suarez, Joann Marie, "THE ROLE OF EXTRACELLULAR POLYMERIC SUBSTANCES IN THE ACCUMULATION AND TRANSPORT OF POLYSTYRENE NANOPARTICLES IN BIOFILMS" (2022). *Doctoral Dissertations*. 2471.

<https://doi.org/10.7275/27078907.0> https://scholarworks.umass.edu/dissertations_2/2471

This Open Access Dissertation is brought to you for free and open access by the Dissertations and Theses at ScholarWorks@UMass Amherst. It has been accepted for inclusion in Doctoral Dissertations by an authorized administrator of ScholarWorks@UMass Amherst. For more information, please contact scholarworks@library.umass.edu.

**THE ROLE OF EXTRACELLULAR POLYMERIC SUBSTANCES IN THE
ACCUMULATION AND TRANSPORT OF POLYSTYRENE NANOPARTICLES
IN BIOFILMS**

A Dissertation Presented

by

JOANN MARIE RODRIGUEZ SUAREZ

Submitted to the Graduate School of the
University of Massachusetts Amherst in partial fulfillment
of the requirements for the degree of

DOCTOR OF PHILOSOPHY

February 2022

Civil and Environmental Engineering

©Copyright by Joann M. Rodríguez Suárez 2022

All Rights Reserved

**THE ROLE OF EXTRACELLULAR POLYMERIC SUBSTANCES IN THE
ACCUMULATION AND TRANSPORT OF POLYSTYRENE NANOPARTICLES
IN BIOFILMS**

A Dissertation Presented

by

JOANN MARIE RODRIGUEZ SUAREZ

Approved as to style and content by:

Caitlyn S. Butler, Chair

Boris Lau, Member

Anne Gershenson, Member

Vincent M. Rotello, Member

John Tobison, Department Head
Civil and Environmental Engineering

DEDICATION

To my grandmother Mami Loles.

*You left this world without seeing me finish my journey towards my doctoral degree,
but I know that wherever you are right now, you are proud of me.*

One day we will see each other again.

ACKNOWLEDGMENTS

I want to thank God for helping me to complete this journey, everything at His perfect timing. I would like to thank my excellent advisor Caitlyn Butler for her academic guidance, mentorship, and dedication to my success. Thanks to Boris Lau, for giving me the opportunity to work with him. Thanks to Anne Gershenson for her mentoring and dedication, I will always appreciate her sincere interest in my success. I would like also thank Vincent Rotello, for his helpful advice on my research. I want to acknowledge the Massachusetts Department of Transportation Highway Division and the NEAGEP Fellowship for funding my research. Special thanks to Erich, Camelia, and Erica for the opportunity to work on the Salt Project and the skills I developed during the project field trips. Thanks to the EWRE group, I always loved that we are like a family. To the best lab manager Sherrie Webb-Yagodzinski and my special friends Aarthi, Chinedum, Andrew, Camila and Salimar for the friendship we developed during these years that I know will last forever. I would like to thank my best friend Esteban, who always reminded me that was capable when I doubted of myself.

I am incredible grateful for the support and love from my parents and my brother Richard, my life goal is to make you always proud of me and to compensate you back for all the sacrifices you all have done to help me complete this degree. I would also like to give special thanks to my partner Jorge, he made this journey easier by being there for me in the moments I most needed. Getting to know him has been without any doubt one of the best things that have happened to me during this time, and to be with him, one of the greatest blessings God has given me in my life. To Toby for always being by my side.

ABSTRACT

THE ROLE OF EXTRACELLULAR POLYMERIC SUBSTANCES IN THE ACCUMULATION AND TRANSPORT OF POLYSTYRENE NANOPARTICLES IN BIOFILMS

FEBRUARY 2022

JOANN MARIE RODRIGUEZ SUAREZ, B.S, UNIVERSITY OF PUERTO RICO,
MAYAGÜEZ CAMPUS

M.S., UNIVERSITY OF PUERTO RICO, MAYAGÜEZ CAMPUS

Ph.D., UNIVERSITY OF MASSACHUSETTS AMHERST

Directed by: Dr. Caitlyn S. Butler

With the increasing number of nanotechnology applications, it is reasonable to expect nanoparticles to be ubiquitous in biofilms found in natural and engineered aquatic systems. We studied the impact of the degree of cross-linking on the deposition and diffusion of polystyrene nanoparticles (NPs) in alginate model biofilm matrices in the presence and absence of calcium cross-linkers using image correlation methods and single particle tracking. We found that cross-linking increases the viscoelasticity and hydration of the polymeric matrix and leads to structural changes that can restrict and alter the diffusive behavior of NPs, but the magnitude of the effects on diffusion depends on NP size. Nonetheless, all sizes of particles considered in the study experienced a degree of confinement and partial confinement demonstrating that diffusion in heterogeneous biofilm matrices should not be assumed to be isotropic. In bacterial biofilms, investigated using the same techniques, NP diffusion modes are dependent on biofilm age and NP functional groups and were affected by the intrinsic variability of

biological systems, even when the biofilms were formed in similar conditions and by the same microorganism. Living biofilms are dynamic and active with responsive interchange between the microbial inhabitants and the biofilm structure. The results from our studies suggest that when NPs accumulate in biofilms, NPs can stress the microbes and alter gene expression of key extracellular polymeric substances production and quorum sensing systems. These changes depend on NP surface charge, gene function and biofilm age and could end up affecting biofilm architecture and metabolic efficiency. These findings elucidating the conditions that affect biofilm structure add to our knowledge of the interactions between biofilms and nanoparticles, leading to a better understanding of the fate, transport, and effect of NPs in the environment and should be useful in the development of biofilm related applications to achieve specific objectives. For example, in medicine, to eradicate biofilm infections by improving the penetration of antibiotics delivered by nanomaterials, or in environmental engineering, to determine how environmental conditions can impact the accumulation of NPs in biofilms in the environment.

TABLE OF CONTENTS

	Page
ACKNOWLEDGMENTS	v
ABSTRACT	vi
LIST OF TABLES	xiii
LIST OF FIGURES	xiv
CHAPTER	
1. INTRODUCTION	1
1.1 Nanomaterials	1
1.2 Environmental fate and transport of nanoparticles	2
1.3 Biofilms.....	6
1.3.1 Extracellular polymeric substances (EPS) cross-linking	8
1.4 Diffusion of nanoparticles in biofilms	9
1.4.1 Techniques to characterize nanoparticle transport.....	11
1.5 Research motivation and general scope	19
2. IMPACT OF THE DEGREE OF CROSS-LINKING IN THE VISCOELASTIC PROPERTIES OF A POLYSACCARIDE MATRIX AND THE ACCUMULATION OF NANOPARTICLES.....	21
2.1 Introduction.....	21
2.1.1 Specific Objectives	22
2.2 Materials and Methods.....	23
2.2.1 Polysaccharides matrices with different degrees of cross-linking.....	23
2.2.2 Determination of the degree of cross-linking of a polysaccharide mixture.....	24

2.2.3 Deposition of nanoparticles over a cross-linked polysaccharide's matrix.....	25
2.3 Results and Discussion	29
2.3.1 Calcium cross-linking can increase alginate matrix hydration and viscoelasticity.....	29
2.3.2 Nanoparticle deposition over a cross-linked alginate matrix is size dependent	33
2.3.3 The degree of cross-linking limits the deposition of nanoparticles	35
2.4 Conclusion	39
3. HETEROGENEOUS DIFFUSION OF POLYSTYRENE NANOPARTICLES THROUGH AN ALGINATE MATIX: THE ROLE OF CALCIUM CROSS-LINKING AND NANOPARTICLE PARTICLE SIZE.....	42
3.1 Introduction.....	42
3.1.1 Specific Objectives	42
3.2 Materials and Methods.....	43
3.2.1 Model polysaccharide matrix.....	43
3.2.2 Sample preparation	44
3.2.3 Microscopic data acquisition	45
3.2.4 Methods used for the microscopy data analysis	48
3.2.5 Statistical Analysis.....	50
3.3 Results and Discussion	50
3.3.1 Nanoparticle accessibility to the alginate matrix cavities.....	50

3.3.2 Nanoparticle movement through the alginate matrices is anisotropic	52
3.3.3 Cross-linking decreases NP diffusion coefficients in a size dependent manner	54
3.3.4 Diffusion behaviors of nanoparticles in an alginate matrix	58
3.3.5 Reproducibility	65
3.4 Conclusion	69
4. THE EFFECTS OF POLYSTYRENE NANOPARTICLES ON THE GENETIC EXPRESSION OF KEY EPS PRODUCTION AND QUORUM SENSING SYSTEMS AS A FUNCTION OF PARTICLE CHARGE AND BIOFILM AGE	72
4.1 Introduction.....	72
4.1.2 Specific Objectives	73
4.2 Materials and Methods.....	74
4.2.1 Preparation of <i>Pseudomonas aeruginosa</i> inoculum	74
4.2.2 Biofilm growth in flow cells chambers with continuous media flow	75
4.2.3 Extracellular DNA and RNA extraction	79
4.2.4 Real-time quantitative PCR experiment	81
4.2.5 Protein quantification.....	83
4.2.6 Statistical analysis.....	84
4.3 Results and Discussion	84
4.3.1 Polystyrene nanoparticles are effective in downregulating <i>pelA</i>	84
4.3.2 Carboxylated polystyrene nanoparticles can decrease <i>lasR</i> gene expression..	87

4.3.3 Aminated polystyrene nanoparticles can increase the <i>rpsL</i> gene expression ..	90
4.4 Conclusion	95
5. DIFFUSION OF POLYSTYRENE NANOPARTICLES IN PSEUDOMONAS AERUGINOSA BIOFILMS AS A FUNCTION OF PARTICLE CHARGE AND BIOFILM MATURITY	97
5.1 Introduction.....	97
5.1.2 Specific Objectives	98
5.2 Materials and Methods.....	99
5.2.1 Biofilm cultivation and nanoparticle treatment	99
5.2.2 Microscopic data acquisition	100
5.2.3 Methods used for the microscopy data analysis	100
5.2.4 Statistical Analysis.....	102
5.3 Results and Discussion	102
5.3.1 Aminated and carboxylated nanoparticles can bind to EPS components in biofilms	102
5.3.2 Nanoparticle diffusion in biofilms depends on biofilm maturity and particle charge	107
5.3.3 Nanoparticles can display different diffusion modes in biofilm matrices	111
5.4 Conclusion	121
6. CONCLUSIONS.....	123

APPENDICES

A. RAW TIRF MICROSCOPY IMAGES FROM CHAPTER 3..... 127

B. FLOW CELLS DESIGN..... 130

C. STATISTICAL ANALYSIS OF DIFFUSION COEFFICIENT DISTRIBUTIONS 133

BIBLIOGRAPHY..... 134

LIST OF TABLES

Table 3.1: Average particle count before and after cross-linking (calculated based on one frame (2 msec) and an area of 128, 169 μm^2 for two independent samples).....	51
Table 3.2: The averaged anisotropy values obtained from the 2D-pCF analysis for each nanoparticle size considered in this study for sample 1.....	53
Table 3.3: The averaged anisotropy values obtained from the 2D-pCF analysis for each nanoparticle size considered in this study in sample 2.	66
Table 4.1: Primer sequences used in qPCR experiment.	82
Table 5.1: Average number of aminated and carboxylated polystyrene NPs identified in a microscopy video of 6,000 frames (3 minutes) for the 48 hrs and 96 hrs biofilm samples. The average values are considering 3 fields of view from each sample in an area of 793 μm^2 . Experiment 1 and 2 are independent experimental replicates.....	105

LIST OF FIGURES

Figure 1.1: Nanoparticle classification based on the particle material, properties, and applications (Khan, Saeed, & Khan, 2019; Yaqoob, Ahmad, Parveen, Ahmad, & Oves, 2020).	1
Figure 1.2: Chemical and physical transformations that could determine NP fate, transport and toxicity include dissolution, sulfidation, aggregation and coating. NP's environmental fate can depend not only on the particle transformations, but also on processes like particle deposition and accumulation in biological matrices (Bundschuh et al., 2018).	3
Figure 1.3: Example of possible NP-biofilm transformations. a) NPs in biofilms can form an organic corona and aggregate altering the particle size and surface properties, b) NPs can dissolve due to ligand mediated dissolution, c) an example of the passivation of silver NPs through sulfidation and, d) particle stabilization by NP corona formation (Desmau et al., 2020).	5
Figure 1.4: Stages of biofilm formation and propagation. (a) Bacteria attach to a surface, (b) cells secrete extracellular polymeric substances, forming a three-dimensional matrix, (c) when the biofilms reach a certain maturity the cells begin to proliferate, (d) cells detach from the surface and return to a planktonic form. (e) The biofilm cycle starts again (Fulaz, Vitale, Quinn, & Casey, 2019).	7
Figure 1.5: Cross-linking of the polysaccharide alginate by calcium ions. The divalent cation creates bridges between alginate chains and leads to the formation of egg-box junctions (Merakchi, Bettayeb, Drouiche, & Adour, 2019).	9
Figure 1.6: Diffusion modes considered in the iMSD analysis (Moens et al., 2015).	15
Figure 1.7: Description of the SPT analysis, a) the algorithm finds the location by fitting a Gaussian to the particle point spread function to find the particle's center, b) by looking at the closer neighbor and with the localized center of the particle spread function the algorithm starts connecting segments from consecutive frames and by closing the gaps links the segments, c) to form trajectories, d) with the mean square displacement curves of individual particles the movement of the particle over time can be characterized and individual diffusion coefficients can be calculated (Shen et al., 2017).	16

Figure 1.8: Anisotropy of diffusion definition diagram (Malacrida, Rao, et al., 2018). .. 18

Figure 2.1: Changes in mass and dissipation energy for alginate matrices. QCM-D data for alginate-calcium matrices including (step V) the deposition of 20, 100 or 200 nm diameter NPs. Each step (I-VI) indicates the introduction of a solution with the component to be deposited over the silica sensor. The run started with the introduction of a PLL solution in 1 mM CaCl₂ (I), followed by a rinse with 1 mM CaCl₂ to remove the PLL loosely bounded to the silica sensor (II). Then a 0.5% alginate solution was introduced (III) and the alginate deposited over the sensor was cross-linked with a 10 mM calcium chloride solution (IV). Step (V) shows the deposition of a 10 mg/L COOH⁻ polystyrene NPs of a) 20 nm, b) 100 nm and c) 200 nm diameter suspended in a 1.3 mM CaCl₂ and 17.6 mM NaCl solution followed by a rinse with a solution with the same ionic strength (VI). 30

Figure 2.2: Changes in the dissipation energy (ΔD) as a function of the changes of the frequency (Δf) for 0.5% (w/v) alginate deposition over a PLL layer. The results presented are the average of the 5th overtone for steps III and IV (Figure 2.1) for all 6 independent runs prior to the addition of nanoparticles. 31

Figure 2.3: Average mass of NPs deposited over the 0.5% alginate matrix cross-linked with a 10 mM CaCl₂ solution. Deposition of 20 nm and 100 nm particles over the matrix increased the mass over the silica sensor. The introduction of the 200 nm particle solution decreased the mass deposited over the sensor, which suggests that these large particles may be able to remove loosely bound alginate chains. 35

Figure 2.4: Titration curves for the determination of free amine groups before and after cross-linking. The titration curve from Chitosan samples 1 and 2 was used to determine the $[-NH_2]_T$. This concentration corresponds to the amine groups that are available for cross-linking for 700 ng/ μ L of chitosan in 100 mM NaCl. The titration curves for 1:1 Chitosan/Dextran (High DCL) and 1:0.3 Chitosan/Dextran (Low DCL) samples were used to calculate the concentration of $[-NH_2]$, which corresponds to the free chitosan amine groups after the cross-linking. 36

Figure 2.5: Relation between DCL and 20 nm NP accumulation in chitosan/dextran sulfate cross-linked matrices. The number in parentheses indicates the percent of cross-linking. 38

Figure 3.1: Schematic of the clear silicone template. The gasket was a custom design obtained from Grace BioLabs. The design was used and described previously by Kisley, et al. (2015). 44

Figure 3.2: Diagram that shows the flow of the sample preparation, data acquisition and data analysis. For the data analysis we used image Mean Square Displacement (iMSD), two-dimensional pair correlation function (2DpCF) and single particle tracking (SPT). 45

Figure 3.3: A 9 frame section of the 12,000 frame microscopy data collected for 20 nm, 100 nm and 200 nm particles. The 12,000 frames were collected at a frame rate of 490 frames/s, but the frames presented here are every 20th frame in order to capture the particles' movement. The images were color inverted for visualization purposes, but the analysis was done with the images in their original colors (white particles and black background) The scale bar (black) in each frame is 5 μm 46

Figure 3.4: Hydrodynamic diameter of NPs used in the study in a solution of 11.4 mM total ionic strength and pH= 5.6. The dots show the mean of 3 independent measurements and the error bars are the standard deviation. 48

Figure 3.5: Connectivity maps for all three fields of view (15.4 x 15.4 μm) obtained by 2D-pCF analysis for the 20, 100 and 200 nm NPs detected in the TIRF evanescent field. Each row shows each field of view analyzed for an alginate and a cross-linked alginate matrix. The scale bar (red) in each map is 5 μm 52

Figure 3.6: Polar graphs of individual tracks (from SPT) of all three fields of view of 20, 100 and 200 nm NPs through an alginate and a cross-linked alginate matrix. Each track has an assigned color that represents a single particle with the origin representing the particle initial position. All the particle tracks for the three fields of view are presented in the polar graph for each alginate matrix condition and particle size. 54

Figure 3.7: Visual maps and diffusion coefficient histograms for each NP size obtained from the iMSD analysis. The bars are histograms with bins sizes of 1 $\mu\text{m}^2/\text{s}$ for the 20 and 100 nm NPs and 0.01 $\mu\text{m}^2/\text{s}$ for the 200 nm NPs. The lines are kernel (Scott) probability density estimates of the diffusion coefficient (D) distributions. Each row shows each field of view analyzed for each condition. The D maps color scale goes from black to red. The red areas are the areas with higher D values and the darker areas the ones with the lower D values. The color-coded values in the distribution graphs are mean, mode and skewness (s) values of the D distributions taking in consideration all 3 fields of view analyzed. The scale bar (white) in each map is 5 μm 55

Figure 3.8: Visual maps and diffusion coefficient histograms obtained from the iMSD analysis. The bars are histograms with a bin sizes of $1 \mu\text{m}^2/\text{s}$. The lines are kernel (Scott) probability density estimates of the diffusion coefficient (D) distributions. The color-coded values in the distribution graphs are mean, mode and skewness (s) values of the D distributions taking into consideration all 3 fields of view analyzed. The maps show the distribution of the diffusion coefficients and the modes of diffusion, freely diffusive (blue), confined (yellow) and partially confined (red). The pie charts represent the average percentage (of the three field of views analyzed) of free diffusion (blue), confined (yellow) or partially confined (red) areas. The scale bar (white and black) in each map is $5 \mu\text{m}$ 57

Figure 3.9: Maps of the distribution of diffusion modes, freely diffusive (blue), confined (yellow) and partially confined (red). Each row shows each field of view analyzed for each condition. The pie charts represent the average percentage (of the three fields of view analyzed) of free diffusion (blue), confined (yellow) or partially confined (red) areas. The line graphs show the mean square displacement (MSD) as a function of time obtained by SPT analysis. The inset for the 200 nm NPs shows an expanded view of the MSDs. All three fields of view were plotted in the same graph for each alginate condition and each particle size studied. The scale bar (black) in each map is $5 \mu\text{m}$ 59

Figure 3.10: Visual maps and diffusion coefficient histograms obtained from the iMSD analysis for the 20 nm particles. The bars are histograms with a bin sizes of $1 \mu\text{m}^2/\text{s}$. The lines are kernel (Scott) probability density estimates of the diffusion coefficient (D) distributions. The connectivity maps were obtained from the 2D-pCF analysis. The D values were up to $30 \mu\text{m}^2/\text{s}$ (scale smaller than alginate samples). Each row shows each field of view analyzed for the glycerol sample. The D visual maps color scale goes from black to red, where the red areas are the areas with higher D values and the darker areas the ones with the lower the D values. The orange area in the D distribution curves represents the theoretical value calculated for a circular rigid particle of 33.6 nm following the Stokes-Einstein diffusion model in a 15% glycerol (v/v) mixture using the viscosity for a temperature range of 15-25 °C. The color-coded values in the distribution graphs are mean, mode and skewness (s) values of the D distribution. The scale bar (white and red) in each map is $5 \mu\text{m}$ 63

Figure 3.11: Visual maps and diffusion coefficient histograms obtained from the iMSD analysis for the 200 nm particles. The bars are histograms with a bin sizes of $0.5 \mu\text{m}^2/\text{s}$. The lines are kernel (Scott) probability density estimates of the diffusion coefficient (D) distributions. The connectivity maps were obtained from the 2D-pCF analysis. The D values were up to $5 \mu\text{m}^2/\text{s}$ (scale smaller than alginate samples). Each row shows each field of view analyzed for the glycerol sample. The D visual maps color scale goes from

black to red, where the red areas are the areas with higher D values and the darker areas the ones with the lower the D values. The orange area in the D distribution curves represents the theoretical values calculated for a circular rigid particle of 232.4 nm following the Stokes-Einstein diffusion model in a 15% glycerol (v/v) mixture using the viscosity for a temperature range of 15-25 °C. The color-coded values in the distribution graphs are mean, mode and skewness (s) values of the D distribution. The scale bar (white and red) in each map is 5 μm 65

Figure 3.12: Connectivity maps for all three fields of view (15.4 x 15.4 μm) obtained from the 2D-pCF for the 20, 100 and 200 nm NPs detected in the TIRF evanescent field. Each row shows each field of view analyzed for an alginate and a cross-linked alginate matrix. The scale bar (red) in each map is of 5 μm 66

Figure 3.13: Average anisotropy values (from 2D-pCF analysis) and polar graphs of individual tracks from the SPT of all 3 fields of views analyzed of 20, 100 and 200 nm NPs through an alginate and a cross-linked alginate matrix. Each track has an assigned color that represents a single particle with the origin representing the initial position. All the particle tracks for the three field of views are presented in the polar graph for each alginate matrix condition and particle size. The cross-linking did not have a statistically significant effect in the anisotropy values (p-value_{20nm} = 0.41, p-value_{100nm} = 0.06 and p-value_{200nm} = 0.54)..... 67

Figure 3.14: Visual maps and diffusion coefficient histograms for each NP size studied obtained from the iMSD analysis. The bars are histograms with bins sizes of 1 $\mu\text{m}^2/\text{s}$ for the 20 and 100 nm NPs and 0.01 $\mu\text{m}^2/\text{s}$ for the 200 nm NPs. The lines are kernel (Scott) probability density estimates of the diffusion coefficient (D) distributions. The D values were up to 50 $\mu\text{m}^2/\text{s}$ for the 20 nm particles. Each row shows each field of view analyzed for each condition. The D maps color scale goes from black to red. The red areas are the areas with higher D values and the darker areas the ones with the lower D values. The color-coded values in the distribution graphs are mean, mode and skewness (s) values of the D distributions taking into consideration all 3 fields of views analyzed. The scale bar (white) in each map is 5 μm 68

Figure 3.15: Maps of the distribution of diffusion modes, freely diffusive (blue), confined (yellow) and partially confined (red). Each row shows each field of view analyzed for each condition. The pie charts represent the average percentage (of the three field of views analyzed) of free diffusion (blue), confined (yellow) or partially confined (red) areas for each NP size. The graphs show the Mean Square Displacement (MSD) in time obtained from the SPT analysis. All three fields of view were plotted in the same graph for each alginate condition and each particle size studied. The scale bar (black) in each map is 5 μm 69

Figure 4.1: Custom designed flow cells. Each flow cell has 3 chambers for sample replicates and are sealed with glass coverslips to allow the in-situ visualization of the sample under the microscope. 75

Figure 4.2: Experimental setup to cultivate biofilms with continuous flow in custom designed flow cells. 76

Figure 4.3: Diagram showing the flow cells exposed to NPs. The flow cell “Control” was treated with HEPES buffer, the “Cationic NP” with aminated polystyrene nanoparticles and the “Anionic NP” with carboxylated polystyrene nanoparticles. Each flow cell has 3 chambers allowing biological triplicates for each condition. 78

Figure 4.4: Normalized fold expression of *pelA* transcription by PAO1 $\Delta wspF \Delta psI$ P_{BADpel} bacterial strain for unexposed biofilms (Control) and NP treated biofilm samples (aminated polystyrene (NH₃⁺) and carboxylated polystyrene (COOH⁻)). The values correspond to two independent experiments and triplicate biological samples for each experiment for each condition (green and yellow symbols indicate the two independent experiments). The qPCR results were normalized to the results for the reference gene *ampR*. The error bars represent the standard error of the mean of 6 biological samples (3 from each experimental replicate). Asterisks indicate statistical significance, * for $p \leq 0.05$ and ** for $p \leq 0.01$ 86

Figure 4.5: Normalized fold expression of *lasR* transcription by PAO1 $\Delta wspF \Delta psI$ P_{BADpel} bacterial strain of unexposed biofilms (Control) and NP treated biofilm samples (aminated- modified polystyrene (NH₃⁺) and carboxylated-modified polystyrene (COOH⁻)). The values correspond to triplicates of biological samples for each condition for two independent experiments normalized to the reference gene *ampR*. The error bars represent the standard error of the mean of 6 biological samples (3 from each experimental replicate). Asterisks indicate statistical significance, * for $p < 0.05$ and ** for $p < 0.01$ 88

Figure 4.6: Normalized fold expression of *rhIR* transcription in the PAO1 $\Delta wspF \Delta psI$ P_{BADpel} bacterial strain for unexposed biofilms (Control) and NP treated biofilm samples (aminated- modified polystyrene (NH₃⁺) and carboxylated-modified polystyrene (COOH⁻)). The values correspond to triplicates of biological samples under each condition for two independent experiments normalized to the reference gene *ampR*. The error bars represent the standard error of the mean of 6 biological samples (3 from each experimental replicate). Asterisks indicate statistical significance, * for $p < 0.05$ and ** for $p < 0.01$ 89

Figure 4.7: Concentration of extracellular DNA extracted from PAO1 $\Delta wspF \Delta psI$ P_{BADpel} unexposed (Control) and NP treated (aminated- modified polystyrene (NH₃⁺) and carboxylated-modified polystyrene (COOH⁻) biofilms. The values correspond to triplicates of biological samples under each condition for two independent experiments. The error bars represent the standard deviation of 6 biological samples (3 from each experimental replicate)..... 90

Figure 4.8: Absolute copy number of *rpsL* transcripts in the PAO1 $\Delta wspF \Delta psI$ P_{BADpel} bacterial strain for unexposed 48 hrs biofilms (Control) and NP treated 48 hrs biofilm samples (aminated- modified polystyrene (NH₃⁺) and carboxylated-modified polystyrene (COOH⁻)). The bar corresponds to the average of three biological samples under each condition. Experiment 1 and 2 are independent experimental replicates. The error bars represent the standard deviation. Asterisks indicate statistical significance, * for p < 0.05 and ** for p < 0.01..... 91

Figure 4.9: Normalized fold expression of *rpsL* transcription by the PAO1 $\Delta wspF \Delta psI$ P_{BADpel} bacterial strain for unexposed biofilms (Control) and NP treated biofilm samples (aminated- modified polystyrene (NH₃⁺) and carboxylated-modified polystyrene (COOH⁻)). The values correspond to triplicates of biological samples under each condition for two independent experiments normalized to the reference gene *ampR*. The error bars represent the standard error of the mean of 6 biological samples (3 from each experimental replicate). Asterisks indicate statistical significance, * for p < 0.05 and ** for p < 0.01..... 92

Figure 4. 10: Total protein concentration measured in the biofilm samples. The concentration of intracellular proteins and protein bound to the bacteria were measured in the cell pellet collected from the biofilm samples while the unbound proteins were measured in the sample supernatant using the Qubit protein assay kit. The values correspond to triplicates of biological samples under each condition for two independent experiments. The error bars represent the standard deviation of 6 biological samples (3 from each experimental replicate). Asterisks indicate statistical significance, * for p < 0.05 and ** for p < 0.01..... 93

Figure 5.1: Microscopy images from one field of view of each condition considered in this study. The fluorescent areas (white areas) are the aminated and carboxylated nanoparticles excited with a 561 nm laser. A control sample of a biofilm without nanoparticles was observed to identify possible background fluorescence emitted from the biofilm components. The scale bar (red) in each image is 5 μ m and the images were recorded at a depth of $z = 4500 \pm 703 \mu$ m. 104

Figure 5.2: Connectivity maps for all three fields of view ($28.2 \mu\text{m} \times 28.2 \mu\text{m}$) obtained by 2D-pCF analysis for the aminated and carboxylated NPs at a depth of $z = 4500 \pm 703 \mu\text{m}$. The two top rows correspond to biofilms from Experiment 1 and the two bottom rows to biofilms from Experiment 2. Experiment 1 and 2 are experimental replicates. Each row shows each field of view analyzed for the 48 hr biofilm samples (blue) and the 96 hr biofilms samples (red). The scale bar (red) in each map is $10 \mu\text{m}$ 107

Figure 5.3: Visual maps and diffusion coefficient histograms for the aminated and carboxylated polystyrene nanoparticles at diffusing at a depth of $z = 4500 \pm 703 \mu\text{m}$. The diffusion coefficients were obtained from the iMSD analysis from Experiment 1. The bars are histograms with bins sizes of $0.1 \mu\text{m}^2/\text{s}$. The lines are kernel (Scott) probability density estimates of the diffusion coefficient (D) distributions. Each row shows the maps from the 48 hr and 96 hr biofilm samples. The D map color scale goes from black to red. The red areas are the areas with higher D values (faster diffusion) and the darker areas the ones with the lower D values (slower diffusion). The color-coded values in the distribution graphs are average values of the D distributions taking into consideration all 3 fields of view analyzed. The scale bar (white) in each map is $10 \mu\text{m}$ 110

Figure 5.4: Visual maps and diffusion coefficient histograms for the aminated and carboxylated polystyrene nanoparticles nanoparticles at diffusing at a depth of $z = 4500 \pm 703 \mu\text{m}$. The diffusion coefficients were obtained from the iMSD analysis from Experiment 2. The bars are histograms with bins sizes of $0.1 \mu\text{m}^2/\text{s}$. The lines are kernel (Scott) probability density estimates of the diffusion coefficient (D) distributions. Each row shows the maps from the 48 hrs and 96 hrs biofilm samples. The D maps color scale goes from black to red. The red areas are the areas with higher D values and the darker areas the ones with the lower D values. The color-coded values in the distribution graphs are average value of the D distributions taking in consideration all 3 fields of view analyzed. The scale bar (white) in each map is $10 \mu\text{m}$ 111

Figure 5.5: Maps of diffusion modes, freely diffusive (blue), confined (yellow) and partially confined (red). Each row shows each field of view analyzed for the 48 hr biofilms and the 96 hr biofilm samples in Experiment 1. The pie charts represent the average percentage (of the three fields of view analyzed) showing free diffusion (blue), confined (yellow) or partially confined (red) areas for each type of NP. The scale bar (black) in each map is $10 \mu\text{m}$ and the z depth was $4500 \pm 703 \mu\text{m}$ 114

Figure 5.6: Maps of the distribution of diffusion modes, freely diffusive (blue), confined (yellow) and partially confined (red). Each row shows each field of view analyzed for the 48 hrs biofilms and the 96 hrs biofilms samples in Experiment 2. The pie charts represent the average percentage (of the three field of views analyzed) of free diffusion (blue),

confined (yellow) or partially confined (red) areas for each type of NP considered. The scale bar (black) in each map is 10 μm and the z depth was $4500 \pm 703 \mu\text{m}$ 115

Figure 5.7: The graphs show the Mean Square Displacement (MSD) in time obtained from the SPT analysis from Experiment 1 biofilm samples. All three fields of view were plotted in the same graph for each nanoparticle considered in this study and the z depth was $4500 \pm 703 \mu\text{m}$ 117

Figure 5.8: The graphs show the Mean Square Displacement (MSD) in time obtained from the SPT analysis from Experiment 2 biofilm samples. All three fields of view were plotted in the same graph for each nanoparticle considered in this study and the z depth was $4500 \pm 703 \mu\text{m}$ 118

Figure 5.9: Polar graphs of individual tracks (from SPT) for all three fields of view from Experiment 1 biofilms at a z depth of $4500 \pm 703 \mu\text{m}$. Each track has an assigned color that represents a single nanoparticle with the origin representing the nanoparticle initial position. All the nanoparticle tracks for the three fields of view are presented in the polar graph for each nanoparticle considered. 120

Figure 5.10: Polar graphs of individual tracks (from SPT) of all three fields of view from Experiment 2 biofilms at a z depth of $4500 \pm 703 \mu\text{m}$. Each track has an assigned color that represents a single nanoparticle with the origin representing the nanoparticle initial position. All the nanoparticle tracks for the three fields of view are presented in the polar graph for each nanoparticle considered. 121

Figure A.1: Images of the 20 nm particles from two independent samples. 80% of the total area of each sample was used for the particle count. The images were color inverted for visualization purposes, but the analysis was done with the images in their original colors (white particles and black background). The scale bar is 50 μm 127

Figure A.2: Images of the 100 nm particles from two independent samples. 80% of the total area of each sample was used for the particle count. The images were color inverted for visualization purposes, but the analysis was done with the images in their original colors (white particles and black background). The scale bar is 50 μm 128

Figure A.3: Images of the 200 nm particles from two independent samples. 80% of the total area of each sample was used for the particle count. The images were color inverted for visualization purposes, but the analysis was done with the images in their original colors (white particles and black background). The scale bar is 50 μm 129

Figure B.1: 2D Schematic with the specific dimensions of the flow cells lid. In the Phillips style #4 of 3/8 inches screws were 1.5 mm holes the Phillips style #4 of 3/8 inches screws were screwed to close the flow cell. 131

Figure B.2: 3D Schematic with the specific dimensions of the flow cells lid. The 22 X 22 cover glass slide were glued over the 16.0 mm squares to seal the flow cell chamber but at the same time allow microscopic visualization..... 131

Figure B.3: 2D Schematic with the specific dimensions of the flow cells bottom. The 22 X 22 cover glass slide were glued over the 16.0 mm squares to seal the flow cell chamber but at the same time allow microscopic visualization. 132

Figure B.4: 3D Schematic with the specific dimensions of the flow cells bottom. In the Phillips style #4 of 3/8 inches screws were 1.5 mm holes the Phillips style #4 of 3/8 inches screws were screwed to close the flow cell. The silicone tubing was connected to the external side stainless-steel tube (OD= 3.2 mm, ID= 3.0 mm) that was glued to the 3.2 mm side holes 132

CHAPTER 1

INTRODUCTION

1.1 Nanomaterials

Nanomaterials are particles with at least one dimension of 100 nm or less, with unique size dependent physico-chemical properties that the material may not possess at the micro or macro scale. Nanoparticles (NPs) usually have a surface layer, a shell layer and a core and are classified based on their physical (size or morphology) and chemical (material reactivity) properties. Figure 1.1 summarizes NP classifications based on particle composition and includes examples of their properties and applications.

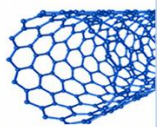
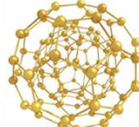
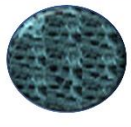



Carbon based	Metal	Ceramics	Semiconductor	Polymeric	Lipid based
					
-Organics	-metals (e.g., gold, silver, copper, titanium)	-calcium phosphates, silica, alumina	-semiconductor material (i.e., quantum dots)	-gelatins, chitosan, PLA, PLGA, PCL, PGA	-solid core lipid and external core of surfactants or emulsifiers
Properties					
-electrical conductivity -strength -electron affinity	-optical polarizability -antibacterial -electrical conductivity	-heat resistant -chemical inertness -high mechanical strength	-optoelectronic -magnetic	-ease of functionalization -biocompatible -biodegradable	-stable -no biotoxicity -biodegradable
Applications					
-fillers -gas absorbents -support media for catalysts	-batteries -catalyst -sunscreen -inks	-biosensors -tissue engineering -drug delivery	-photocatalysis -photo optics -electronic devices -cancer diagnosis	-drug delivery -gene therapy	-drug carriers and delivery -cancer therapy

Figure 1.1: Nanoparticle classification based on the particle material, properties, and applications (Khan, Saeed, & Khan, 2019; Yaqoob, Ahmad, Parveen, Ahmad, & Oves, 2020).

Nanomaterials are ubiquitous in nature due to natural processes at the nanoscale such as mineral growth, transformation, and weathering and as an indirect result of microbial activity. Since the 1980s, engineered NPs have been synthesized in the laboratory with levels of purity, order and scale that cannot be found in nature (Hochella, Spencer, & Jones, 2015). Due to the unique characteristics that materials can exhibit at the nanoscale, NPs have been used in medicine for drug delivery and cancer treatment, in environmental remediation as gas adsorbers, in electronics, in personal care products like sunscreen and in water treatment technologies among other fields and applications (Banerjee & Sengupta, 2011; Billingsley, Riley, & Day, 2017; Brown et al., 2012; Ikuma & Lau, 2013).

1.2 Environmental fate and transport of nanoparticles

With the increasing number of nanotechnology applications and with the ubiquity of nanoparticles, it can be expected that nanoparticles interact with the environment. Most studies about NP fate and transport have focused on estimating the quantities that could be released into environmental and engineered systems by developing models that rely on NP production and use data. For example, a mathematical model estimated that in 2017, 36,000 tons/year of three of the most frequently used engineered NPs were released into engineered systems including landfills, recycling systems, waste incineration and sewage treatment (Giese et al., 2018).

To evaluate NP behavior and the effects of their emission into environmental and engineered systems it is important to not only quantify the amount of NPs released, but also, to evaluate their movement and their presence. Studies of NP fate, transport and

environmental implications are not simple due to the complexity of the systems, the transformations and processes that the particles can go through, and the limitations of analytic techniques for NP detection and quantification (von der Kammer et al., 2012). When NPs enter complex matrices like environmental systems, they remain pristine for a very short time (Westmeier et al., 2018) before they undergo physico-chemical transformations and processes that could determine their fate, transport, and toxicity (Figure 1.2). These transformations and processes depend on the particle's properties of and the environmental conditions (Dale et al., 2015; Peijnenburg et al., 2015).

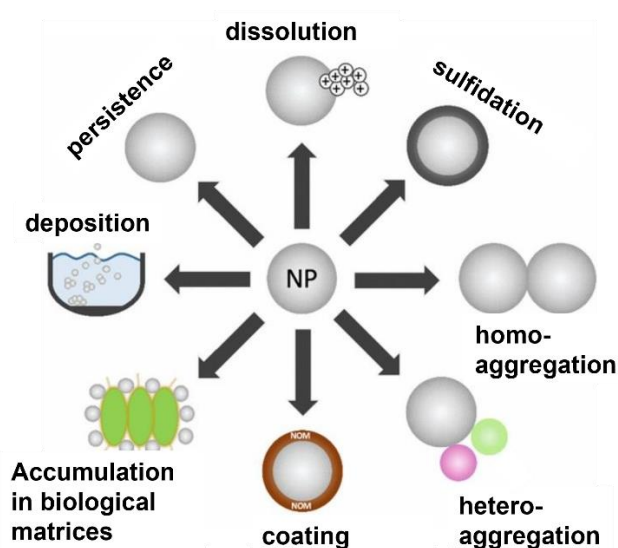


Figure 1.2: Chemical and physical transformations that could determine NP fate, transport and toxicity include dissolution, sulfidation, aggregation and coating. NP's environmental fate can depend not only on the particle transformations, but also on processes like particle deposition and accumulation in biological matrices (Bundschuh et al., 2018).

The transformations include dissolution, sulfidation, aggregation, coating, deposition and the accumulation in biological matrices. In the case of NP accumulation in biological

matrices, biofilms have the potential to impose strong controls on the NP life cycle in natural and engineered systems (J. I. . Kim, Park, Chang, Nam, & Yeo, 2016; Park et al., 2018; Perrier et al., 2018; Schierz et al., 2014; Tang, Zhu, Zhu, Zamir, & Wu, 2018). For example, researchers have identified NPs in the sewage system (B. Kim, Park, Murayama, & Hochella, 2010), probably released during the process of manufacturing, use or disposal of nanomaterials. To minimize pollution and protect public health, sewage is treated in a wastewater treatment plant (WWTP) through a combination of physicochemical and biological processes before it is released into waterways such as rivers, lakes and oceans. Considering the presence of biofilms within the treatment processes and in the receiving environment downstream of municipal and industrial WWTPs, NP interactions with biofilms are a critical component in understanding the fate of NPs within the engineered water cycle and the downstream environment.

Biofilms can act as competing sorbents due to surface chemistry interactions (e.g., electrostatic forces and hydrophobic interactions) and size exclusion by the heterogeneous structural properties of the biofilm (e.g., permeability and density) (Flemming & Wingender, 2010). In a study of gold nanorods in an estuarine mesocosm with different compartments including water, sediment, microbes, biofilms, clams and fish, the nanorods partitioned from the water column and accumulated mostly in the clams and biofilms after 12 days (Ferry et al., 2009). In addition to acting as possible reservoirs of NPs, biofilms in natural and engineered systems can transform NPs and vice versa.

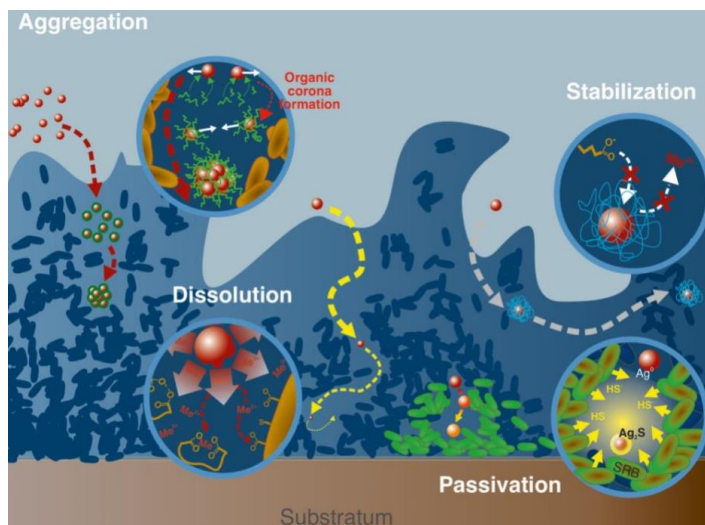


Figure 1.3: Example of possible NP-biofilm transformations. a) NPs in biofilms can form an organic corona and aggregate altering the particle size and surface properties, b) NPs can dissolve due to ligand mediated dissolution, c) an example of the passivation of silver NPs through sulfidation and, d) particle stabilization by NP corona formation (Desmau et al., 2020).

Some NPs can cause damage to cells and affect the ecosystem. For example, titanium dioxide NPs can cause cell membrane damage, the generation of intracellular reactive oxygen species and reduce the activity of extracellular enzymes (Battin, Kammer, Weilhartner, Ottofuelling, & Hofmann, 2009; Schug, Isaacson, Sigg, Ammann, & Schirmer, 2014). NP transformations due to microbial activity can occur even in particles that are considered stable (Figure 1.3). For example, biofilms of *Egeria densa* can dissolve gold NPs within days (Avellan et al., 2018) and extracellular polymeric substances from periphytic organisms can stabilize and dissolve cerium dioxide NPs and increase the size of silver NPs (Kroll, Behra, Kaegi, & Sigg, 2014).

1.3 Biofilms

Biofilms are complex structures of microorganisms embedded in a highly hydrated heterogeneous matrix of macromolecules known as extracellular polymeric substances (EPS). Single-species or multi-species biofilms can be found in environmental and engineered systems. Biofilms are the most common microorganism lifestyle because the matrix surrounding the cells can serve as a protector barrier for non-ideal environments (e.g., predation, desiccation and starvation) and increase cell adherence to surfaces (Toole, 2003).

There are different stages of biofilm formation and propagation (Figure 1.4). The first step for biofilm development is the attachment of planktonic cells to a surface. They can attach to different types of surfaces, from materials like metal and plastic, to tissues. After the attachment, the cells secrete EPS and form a three-dimensional matrix. The dispersal stage of the biofilm is a survival response to environmental changes (e.g., nutrients or oxygen levels, temperature, and pH) that could be favorable or unfavorable for the cell's propagation. This stage of biofilm formation is regulated via quorum sensing signals (Kaplan, 2010) and when the population gets to a certain density enzymes degrade EPS components and the cells regain mobility.

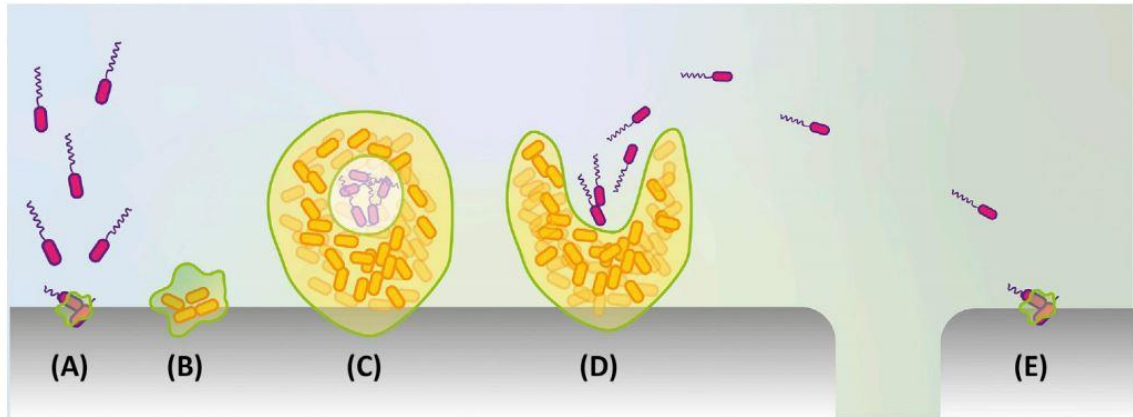


Figure 1.4: Stages of biofilm formation and propagation. (a) Bacteria attach to a surface, (b) cells secrete extracellular polymeric substances, forming a three-dimensional matrix, (c) when the biofilms reach a certain maturity the cells begin to proliferate, (d) cells detach from the surface and return to a planktonic form. (e) The biofilm cycle starts again (Fulaz, Vitale, Quinn, & Casey, 2019).

The structure of biofilms is dictated by the EPS, which is composed of a range of biomolecules, including polysaccharides (up to 95 wt%), proteins (up to 60 wt%), lipids (up to 40 wt%), and even nucleic acids (up to 10 wt%) (Flemming & Wingender, 2010). EPS has been identified as essential for biofilm establishment. It contains the structural elements responsible for mechanical stability and controls and limits the diffusion of molecules and particles by selective barriers (Lieleg, Oliver; Ribbeck, 2011; Wingender, Neu, & Flemming, 1999). Because EPS forms a three-dimensional gel-like matrix, the size of pore-spaces of the biofilm can vary, in part, depending on the EPS density (Beech, 2004). The EPS structure and composition can be spatially heterogeneous and highly variable depending on the species that forms the biofilm and the environmental conditions at which the biofilm is exposed (Flemming & Wingender, 2010).

1.3.1 Extracellular polymeric substances (EPS) cross-linking

Polysaccharides are a major component of the EPS. After the cells secrete the polysaccharides, they can undergo modifications due to enzymatic alterations, cross-linking or variable polymerization. These polysaccharides modifications can occur at different locations, (e.g., in the periplasm of Gram-negative bacteria, on the cell surface or in the extracellular space), adding more spatial and temporal heterogeneity to the EPS matrix (Rička & Tanaka, 1984; Wloka, Rehage, Flemming, & Wingender, 2004). In this study we focused on the polysaccharide modifications resulting from cross-linking.

When polysaccharides cross-link to various degrees in a biofilm, the entangled polymer chains forms a three-dimensional network that will regulate the matrix stiffness (a higher degree of cross-linking will cause less swelling of the polymer matrix) (Theocharis, Skandalis, Gialeli, & Karamanos, 2016) and lead to the formation of physical “channels” and changes in the ionization of the functional groups of the polymer (Rička & Tanaka, 1984; Wloka et al., 2004).

Cross-linking can be covalent or ionic, and can depend on the polysaccharide structure, configuration, and concentration, and on the pH and ionic strength of the surrounding bulk solution. For example, for polymers such as alginate, the introduction of or increases in divalent cation concentrations will lead to bridges between carboxyl groups on adjacent polymer chains, decreasing the pore size and increasing rigidity (Wloka et al., 2004) (Figure 1.5).

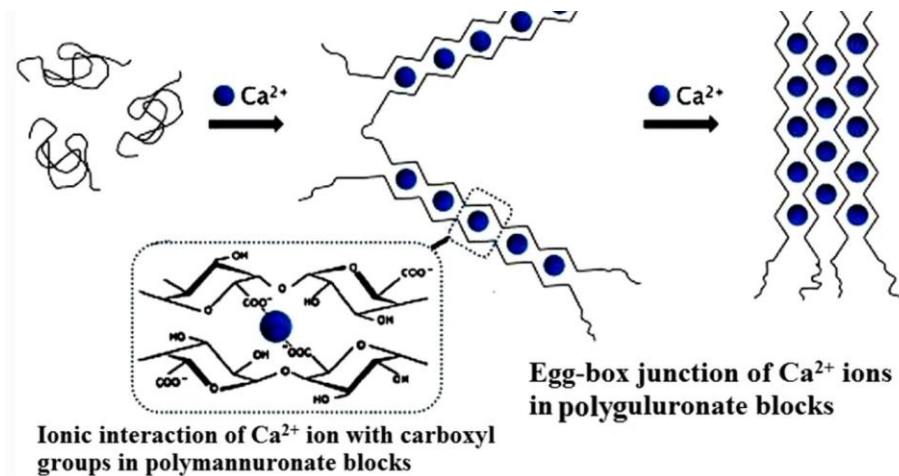


Figure 1.5: Cross-linking of the polysaccharide alginate by calcium ions. The divalent cation creates bridges between alginate chains and leads to the formation of egg-box junctions (Merakchi, Bettayeb, Drouiche, & Adour, 2019).

Polysaccharides can also cross-link to other EPS components like extracellular DNA (Jennings et al., 2015). These links between adjacent EPS polymers can be transient providing the biofilm matrix with a capability to expand or contract, in response to environmental changes. Previous studies have shown that eDNA cross-linking mechanisms can provide mechanical strength and resilience to the biofilm matrix (Devaraj et al., 2019).

1.4 Diffusion of nanoparticles in biofilms

The main transport mechanism in biofilms is diffusion (Stewart, 2003) and previous studies have characterized the movement of NPs through a biofilm matrix in terms of NP diffusion coefficients. When diffusion coefficients were determined experimentally, it was found that rates of diffusion decreased exponentially with the square of the NP size (Peulen & Wilkinson, 2011). However, there was variability in diffusion coefficients due

to local heterogeneity in EPS density at the microscale (Flemming et al. 2016; Flemming & Wingender, 2010; Peulen & Wilkinson, 2011).

As mentioned above, polysaccharides are the major structural component of the EPS (up to 95%), which suggests that polysaccharides play a significant role in the deposition and transport of NPs in biofilms. Polysaccharides meshes can act as selective barriers in which the matrix and particle affinity can control particle diffusion. Size filtering by the polysaccharide mesh can result in NP trapping even when the particles do not chemically interact with the matrix. The polymer mesh size, and thus size filtering, is dictated by the polymer concentration and degree of cross-linking (Amsden, 1999). If the distance between the adjacent links of the polymer mesh is much larger than the particle, the viscosity of the interstitial space will dictate the diffusion. In this size regime transport occurs within EPS's 3D-meshwork of polymers with water-filled pore-spaces (Decho, 1990). When the particle is larger than or close to the mesh size, the particle can get trapped limiting diffusion. However, even these larger particles can escape confinement due to the constant rearrangement and deformations the polysaccharides can experience due to the polymer thermal motion and structural dynamics (Witten & Ribbeck, 2017). In conditions where the electrostatic interactions between the matrix and the NPs are favorable, NP transport rates are lower, but particle size can still play a role (McGill, Cuylear, Adolphi, Osiński, & Smyth, 2009). In general, NP movement is limited by the biofilm matrix density and structural arrangements, but also is influenced by the particle surface chemistry (including charge and hydrophobicity) and size (Golmohamadi, Clark, Veinot, & Wilkinson, 2013; McGill et al., 2009; Peulen & Wilkinson, 2011).

1.4.1 Techniques to characterize nanoparticles transport

Computational models have been used previously in studies that involve the characterization of particle transport (Hansing et al., 2016). These are mainly Brownian dynamics simulations that consider free diffusion as the mode of diffusion, which is reasonable for theoretical predictions of particle behavior in a rigid periodic lattice and for small molecules that do not significantly interact with the matrix. However, most of these simulation models are not appropriate for particles moving in heterogenous matrixes like the EPS because free-diffusion models do not consider anomalous particle diffusion and polymer network flexibility.

In experimental studies, the movement of particles in a matrix could be studied using particles labeled with a fluorescent dye. These particles are added to the matrix of interest and particle movement is visualized, recorded, and analyzed. Analysis methods such as fluorescent correlation spectroscopy (FCS) can characterize the bulk behavior while methods such as single particle tracking (SPT) work at the individual particle level.

FCS was first described in 1972 for the description of chemical reactions and then its interpretation for particles was introduced in 1974 by Rigler and Eigen (Ehrenberg & Rigler, 1974; Magde, Elson, & Webb, 1972). In FCS, diffusing fluorescently labeled particle traverse an open-volume element created by a focused beam and the fluorescence intensity fluctuates as the particle move in and out of the open-volume element (Visser & Hink, 1999). Correlating the fluorescence intensity over time provides information about the diffusion of the fluorescent particle or molecule. The normalized time-correlated autocorrelation function is calculated as:

$$G(\tau) = \frac{\langle I(t) \cdot I(t+\tau) \rangle}{\langle I^2 \rangle} = \frac{\langle I^2 \rangle + \langle \delta I(t) \cdot \delta I(t+\tau) \rangle}{\langle I^2 \rangle} \quad (1)$$

Equation (1) relates the fluorescence intensity I , at time t to that τ seconds later where the brackets indicates averaging over the entire time course and $\delta I(t)$ is the intensity fluctuation at time t (Visser & Hink, 1999). Assuming a Gaussian shaped three dimensions detection volume:

$$G(\tau) = 1 + \left[(1 - F + F \cdot e^{-\lambda\tau}) / N_m \left(1 + \frac{4D}{\omega_1^2 \cdot \tau} \right) \times \left(1 + \frac{4D}{\omega_2^2 \cdot \tau} \right)^{1/2} \right] \quad (2)$$

where D is the diffusion coefficient for translational diffusion, N_m is the time-averaged number of particles in the detection volume, the ω_1 and ω_2 are related with the radial and axial radii, λ is the characteristic triplet decay and F describes the fraction of molecules in the triplet state. The diffusion coefficient, which is determined by Brownian motion, is the self-diffusion coefficient of the fluorescent particle in two dimensions and is related with the diffusion time by:

$$D = \frac{\omega_1^2}{4 \cdot \tau_{diff}} \quad (3)$$

where τ_{diff} is the time needed for the particle to diffuse over a distance ω_1 .

For a sphere, the diffusion coefficient D is related to the particle hydrodynamic radius by the Stokes- Einstein equation where k is the Boltzmann constant, T is the temperature and η is the viscosity.

$$r_h = \frac{k \cdot T}{6 \cdot \pi \cdot D \cdot \eta} \quad (4)$$

Peulen and Wilkinson have used FCS to study biofilms and to characterize the diffusion of several model NPs in real biofilms (Peulen & Wilkinson, 2011). Some of the disadvantages of this method is that it only provides average diffusion characterization, is based on intensity fluctuations, so particles that are immobile in the matrix do not contribute to the diffusion coefficient calculation, and the spatial resolution is limited by diffraction. An interesting extension of FCS that overcomes the diffraction limit and has been used for the characterization of porous materials similar to the biofilm matrix is the “fluorescent correlation spectroscopy super-resolution optical fluctuation imaging” (fcsSOFI). This method can characterize the nanostructure of porous matrices and the Brownian diffusion dynamics of particles (Kisley et al., 2015).

A method similar to FCS is image correlation spectroscopy (ICS) which is based on the correlation analysis of fluorescence fluctuations in an image. With this method it is possible to characterize diffusion in terms of diffusion coefficients but it is not sensitive to the direction at which the fluorescent particle or molecule exits the volume defined for the correlation (Petersen, Hddelius, Wiseman, & Seger, 1993). Herbert et al., were able to develop an extension of ICS that can do both, a temporal and a spatial correlation of the fluorescence intensity fluctuations called space-time image correlation spectroscopy (STICS) (Hebert, Costantino, & Wiseman, 2005).

The STICS method allows one to measure slow diffusion in magnitudes of $\mu\text{m}/\text{min}$ but not faster diffusion rates. Rienzo et al. developed a modification of STICS that overcomes this limitation called the image mean square displacement (iMSD). The iMSD method, available in the SimFCS software, determines how the probability of finding a molecule at a given distance evolves as a function of time (Digiacoimo, Digman, Gratton,

& Caracciolo, 2016). iMSD is an extension of the spatiotemporal image correlation spectroscopy function and can be related to diffusion modes (Figure 1.6). These diffusion modes describe particles that are linearly diffusing, confined or partially confined (Moens, Digman, & Gratton, 2015). The modes of diffusion are described by the following equation (Malacrida, Hedde, Ranjit, Cardarelli, & Gratton, 2018):

$$\sigma^2(\tau) = \sigma_0^2 + 4D\tau + \frac{L^2}{3}(1 - e^{-k_{micro}\tau}) \quad (5)$$

where σ_0^2 is the y-intercept of the MSD versus time curve and is related to the size of the particle, L is the confinement size, k_{micro} is the rate constant for confinement and D is the diffusion coefficient of the particle in the material under study. By considering three diffusion modes it is possible to describe more specifically the particle motion and to distinguish areas in which the particles are freely diffusing from areas where the particles are confined or partially confined.

As Figure 1.6 shows, the iMSD curve shows a linear increase versus time for linear or isotropic diffusion (red curve). The higher the D value the higher the slope which means that the particle moved faster and was able to travel a greater distance in a specific time. For the confined mode of diffusion, the iMSD curve reaches a plateau in a short time indicating that the MSD of the particle does not change with time (blue curve). When particles are confined but find a way to get out of confinement and start moving freely the iMSD curve starts with a lower slope, but when the particle escapes confinement, the slope suddenly increases (green curve).

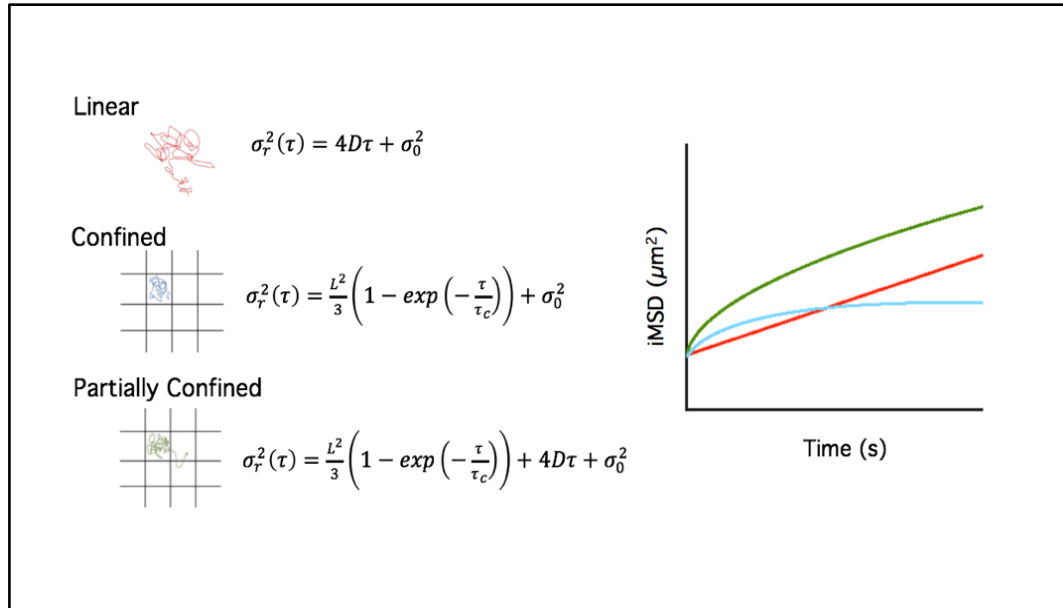


Figure 1.6: Diffusion modes considered in the iMSD analysis (Moens et al., 2015).

The previously mentioned single particle tracking (SPT) method tracks the position of individual particles in real time (Figure 1.7). SPT is appropriate for samples with low particle density but can get complicated if the particles merge, split or temporarily disappear due to out of focus motion or blinking. There are available custom-made SPT tracking programs, open access software and commercial software that can identify the particles trajectories by an iterative process to recognize and track particles based on spatial proximity (Crocker & Grier, 1996; Liao, Yang, Koh, Matzger, & Biteen, 2012). One user friendly commercially available software that includes the SPT analysis and allows one to track particles motion in real time is the NIS-Elements Image Analysis Software by Nikon. The SPT analysis method in this package, based on work by Jaqaman et al., uses an algorithm that links particles between consecutive frames and then forms trajectories by linking these continuous segments and closing gaps allowing the accurate tracking of particle movement (Jaqaman et al., 2009). Using the mean square

displacement (MSD) curve of individual particles, this algorithm can calculate the average diffusion coefficient but also, the diffusion coefficient for each individual particle in the sample. The diffusion coefficient can be calculated with the following equation considering a track of k number of frames and assuming N successive fitted positions:

$$MSD_i = 2nDt_i + E \quad i = 1, \dots, N \quad (6)$$

where D is the diffusion coefficient determined by fitting a line to the first third of the MSD vs time curve, t is time and n is the number of dimensions (Jaqaman et al., 2009).

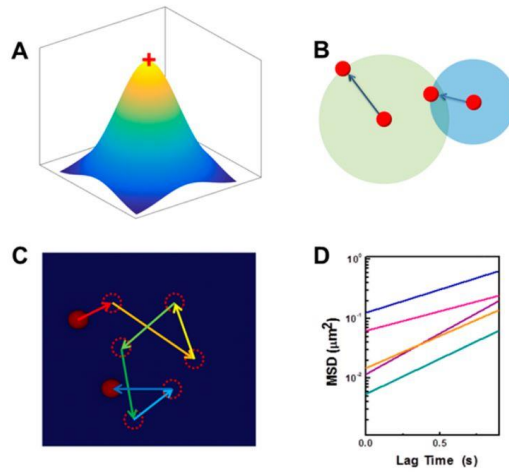


Figure 1.7: Description of the SPT analysis, a) the algorithm finds the location by fitting a Gaussian to the particle point spread function to find the particle's center, b) by looking at the closer neighbor and with the localized center of the particle point spread function the algorithm start connecting segments from consecutive frames and by closing the gaps links the segments, c) to form trajectories, d) with the mean square displacement curves of individual particles the movement of the particle over time can be characterized and individual diffusion coefficients can be calculated (Shen et al., 2017).

All the methods described above are focused on the characterization of the diffusion behavior of the particle which will be influenced by the matrix structure in which the

particle is diffusing. For that reason, when studying the diffusion of particles, in this case NPs in a heterogeneous matrix, it is useful to have an analysis that could help characterize the matrix structural features at the nanoscale (e.g., pores and channels). The two-dimensional pair correlation function (2D-pCF) could be a good alternative for this type of analysis. The 2D-pCF method, which is also available in the SimFCS software, provides high spatial resolution because it is a correlation between the intensity fluctuations of a pair of pixels (Malacrida, Hedde, et al., 2018). The 2D-pCF analysis detects particles at two different arbitrary but adjacent locations and measures the average time it takes for the particles to move from one location to the other. It is able to detect barriers of diffusion based on the time that it takes for the particle to be detected at the second location. If the time is longer than the expected average time, the 2D-pCF analysis implies that there is at least one barrier between those two locations (Malacrida, Rao, & Gratton, 2018). With the 2D-pCF you can generate connectivity maps and visualize the matrix structure features that may interfere with the particle's diffusion. This method also provides information about the anisotropy of diffusion. The anisotropy of diffusion, reports on the directional dependence of particle diffusion, is obtained from the long and short axes of the two-dimensional pair correlation function (Figure 1.8). If there are no barriers for diffusion the axes have equal lengths, and the anisotropy of diffusion is zero. The pair correlation function is defined by the following equation (Digman & Gratton, 2009):

$$pCF = G(\tau, r_0, r_1) = \frac{\langle I(t, r_0) \cdot I(t + \tau, r_1) \rangle}{\langle I(t, r_0) \cdot I(t, r_1) \rangle} - 1 \quad (7)$$

where, τ is the time delay between acquisitions of I , the fluorescence intensity at points r_0

and r_l . The brackets indicate the temporal average. For a given point, r_0 , the pair correlation is measured for all points surrounding r_0 that are a given distance δr away. If motion is isotropic, the pCF does not depend on the angle between points r_0 and r_l and all the pCF curves have the same shape. If motion is anisotropic, for example, if there is a barrier to diffusion in one direction, it will take longer to diffuse the same distance in one direction than in another and the pCF curves will be angle dependent. The angular dependence of the pCF results can be used to calculate anisotropy by (Malacrida, Rao, et al., 2018):

$$\text{Anisotropy} = \frac{\lambda_1 - \lambda_2}{\lambda_1 + \lambda_2} \quad (8)$$

where, λ_1 is the long axis where the motion is relatively unhindered and λ_2 is the short axis where motion is hindered. Figure 1.8 shows a diagram of the anisotropy definition.

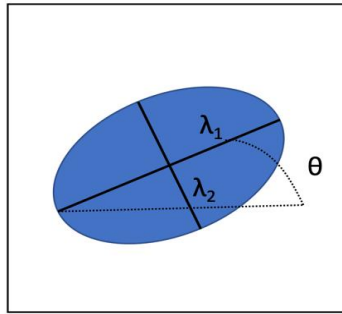


Figure 1.8: Anisotropy of diffusion definition diagram (Malacrida, Rao, et al., 2018).

The combination of iMSD, 2D-pCF, and SPT, which are microscopy advances previously used in cell systems (Di Rienzo, Gratton, Beltram, & Cardarelli, 2013; Digiacomo et al., 2016; Digman & Gratton, 2009; Malacrida, Hedde, et al., 2018; Malacrida, Rao, et al., 2018) to quantitate heterogeneous diffusion, could formulate a better understanding of

heterogeneous diffusion-controlled systems. In the case of biofilm systems, these methods could lead to a better understanding of the natural spatial heterogeneity of the EPS, how local structural micro-domains affect the mobility of NPs in biofilms and can provide experimental data to develop mathematical biofilms models that consider the variable diffusivity modes of solutes within biofilms.

1.5 Research motivation and general scope

Researchers have identified NPs in the sewage system (Kim et al. 2010) probably released during the process of manufacturing, use or disposal of nanomaterials that will end up in a wastewater treatment plant to be treated in bioreactors. In a bioreactor, where biofilms are attached to a fixed or moving carrier, local environmental conditions and bulk phase conditions (i.e., organic load, dissolved oxygen, temperature, ions concentration, pH and alkalinity) are important to promote specific metabolic activities and achieve treatment objectives (Morgenroth 2008). As mentioned before, cross-linking could affect the structure of biofilms, and the degree of cross-linking depends on polysaccharide concentration, and on the pH and ionic strength of the surrounding bulk solution. The overall aim of this study is to investigate how the EPS architecture dictates the accumulation and movement of NPs in biofilms to better understand the fate, transport, and effect of NPs on biofilms in the environment and in engineered systems like bioreactors used in a WWTP. Researchers have studied NP-biofilm interactions mostly from the NP's perspective (size and surface) to identify the particle's characteristics that lead to an effective accumulation and penetration in biofilms (Miller et al. 2015). However, the main focus of this study is to evaluate how biofilm structural

properties can change due to different DCL of the EPS components and how these changes reduce or enhance NP accumulation and transport into the biofilm matrix.

Specific Objective 1

Chapter 2: Identify the impact of the degree of cross-linking on nanoparticle deposition in a simple biofilm model using a polysaccharide as a model matrix.

Specific Objective 2

Chapter 3: Characterize the diffusion of polystyrene nanoparticles as a function of nanoparticle size and polysaccharide degree of cross-linking.

Specific Objective 3

Chapter 4: Investigate if nanoparticles in a *Pseudomonas aeruginosa* biofilm could be a stressor to the cells that could affect the expression of genes related with the EPS production and quorum sensing systems.

Specific Objective 4

Chapter 5: Characterize the diffusion of polystyrene nanoparticles in a *Pseudomonas aeruginosa* biofilm as a function of nanoparticle charge and biofilm age.

CHAPTER 2

IMPACT OF THE DEGREE OF CROSS-LINKING IN THE VISCOELASTIC PROPERTIES OF A POLYSACCHARIDE MATRIX AND THE ACCUMULATION OF NANOPARTICLES

2.1 Introduction

As mentioned before in Chapter 1, polysaccharides are the major component of the extracellular polymeric substances (EPS) throughout the biofilm matrix. According to Ikuma et al. (2015), when nanoparticles (NPs) reach a biofilm matrix, first NPs attach and accumulate in the biofilm top surface layer and then they diffuse through the biofilm matrix. The accumulation of the NPs in the surface layer of the biofilm depends on the properties of the EPS components at that location, the NP properties, and the composition of the surrounding bulk solution.

Polysaccharides are long chain polymers with the ability to cross-link. The degree of cross-linking (DCL) depends on the polysaccharide structure, configuration, and concentration, and on the pH and ionic strength of the surrounding bulk solution. When a polymer is cross-linked, the number of free functional groups of the polymer (in this case, polysaccharides) and the distance between the polymer chains can increase or decrease depending on the DCL. A high DCL can reduce the number of free functional groups on the polymer, decrease the space between the polymer chains (matrix channels) and reduce the flexibility of the polymer. This chapter presents the results from experiments

where we explored the effects of the DCL on the viscoelasticity of a polysaccharide matrix and on the deposition of carboxylated polystyrene NPs into the matrix.

2.1.1 Specific Objectives

The specific objective of this study was to evaluate the impact of the polysaccharide's degree of cross-linking (DCL) on:

- a) the viscoelasticity of an alginate matrix cross-linked with calcium ions
- b) the carboxylated polystyrene nanoparticle (NP) deposition on a single and multi-polysaccharide cross-linked matrices as a function of NP concentration and size.

Our hypothesis was that a low DCL will result in polysaccharides with a higher concentration of free functional groups and larger void space between the polymer chains. Depending on the NP surface charge, a low DCL will reduce, in the case of same charged pairs, or increase, in the case of opposite charged pairs, the attractive forces between the NPs and polysaccharide matrix. As a result, there will be an increase in NP deposition if electrostatic forces are favorable. However, the deposition of the particles will not only depend on electrostatic forces between the NPs and the polymeric matrix, but also, on the space available in the matrix for the particles to deposit. A higher DCL will reduce the interstitial space between the polymer chains limiting the concentration of NPs that can get into the matrix. The deposition of particles smaller than the matrix pore size will be higher in comparison with particles that are close to or bigger than the matrix pores.

2.2 Materials and Methods

2.2.1 Polysaccharides matrices with different degrees of cross-linking

In this study we established different DCL in a polymeric matrix by adding a cross-linking agent and by controlling the concentration ratio of a polysaccharide's mixture. To evaluate the effect of the DCL on the polysaccharide's viscoelastic properties, we used alginate as a model polysaccharide and calcium ions as the cross-linking agent. Alginate is a polyelectrolyte that consists of uronic acid residues, β -D-mannuronate and α -L-guluronate that can form permanent junctions points with calcium ions (Wloka et al., 2004). A solution of 0.5% (w/v) alginate (alginic acid sodium salt, CAS:9005-38-3 Sigma-Aldrich) was prepared by adding 0.250 grams of alginate to 50 milliliters of ultrapure water generated by reverse osmosis (MilliQ Ultrapure Water system, Millipore). The solution was under continuous mixing overnight to completely dissolve the alginate powder in the water. To cross-link the alginate, a 10 mM solution of CaCl_2 was used. We used alginate-calcium (pH = 5.6) matrices to study the effect of cross-linking on the viscoelastic properties of the polymer and the deposition of carboxylated polystyrene particles as a function of the particle size.

To explore the effect of the DCL on the deposition of carboxylated polystyrene NPs as a function of NP concentration, we prepared a mixture of chitosan, a cationic polysaccharide, and dextran sulfite, an anionic polysaccharide, in an ionic strength of 100 mM (NaCl) (pH= 7.01). Chitosan is a polycationic amino polysaccharide that is the deacylated derivative of chitin (Guibal, 2004). Dextran sulfate is a highly soluble polyanionic derivative of dextran. Mixtures with two different DCL were established by adjusting the chitosan to dextran sulfate concentration ratio. Solutions of chitosan and

chitosan-dextran sulfate were prepared with high (1:1) and low concentration (1:0.3) ratios. The concentration of chitosan was fixed at 700 ng/μL, while the concentrations of dextran sulfate were 200 ng/μL (Low concentration) and 700 ng/μL (High concentration). All solutions were prepared by adding chitosan (medium molecular weight, Sigma Aldrich, CAS: 901276-4) and dextran sulfate (sodium salt, Alfa Aesar, CAS: 9011-18-1) at the respective concentrations to a 100 mM NaCl water solution.

2.2.2 Determination of the degree of cross-linking of a polysaccharide mixture

The DCL of the chitosan and dextran sulfate mixtures were determined by performing a potentiometric titration to quantify the free protonatable functional groups of the chitosan before and after cross-linking with dextran sulfate following the method described by Skoog et al. (1996). After the cross-linking procedure any remaining free protonatable functional groups were protonated by adding 20 mL of 0.1 M HCl. After 15 minutes of mixing after the acid addition, the sample was titrated with 0.1 M NaOH. Both the sample with the chitosan, dextran sulfate and HCl and the 0.1 M NaOH solution in the burette were at the same ionic strength (100 mM using NaCl). The DCL was calculated based on the chitosan amine concentration using the following expression (Osifo et al., 2008) :

$$DCL = 1 - \frac{[-NH_2]}{[-NH_2]_T} \quad (9)$$

where $[-NH_2]$ is the amine concentration of chitosan after cross-linking and $[-NH_2]_T$ is the amine concentration of chitosan before cross-linking. The $[-NH_2]$ is calculated using the titration curve of the chitosan-dextran sulfate solution (High DCL 700 ng/μL / 700

ng/ μ L and Low DCL 700 ng/ μ L / 200 ng/ μ L) and the $[-NH_2]_T$ is calculated from the titration of the chitosan only solution (700 ng/ μ L) using the follow expression:

$$[NH_2] = ((C_2 \cdot V_2 - C_1 \cdot V_1) \cdot MW_{NH_2}) \quad (10)$$

where C_1 is the HCl acid concentration (0.1 M), C_2 is the NaOH base concentration (0.1 M), V_1 is the volume of HCl acid added obtained from the first inflection point of the titration curve and V_2 is the volume of NaOH base obtained from the second inflection point of the titration curve. The molecular weight of the amine group, MW_{NH_2} , is 16 g/mol. Each titration curve was repeated in duplicate and the mean DCL value is reported below.

2.2.3 Deposition of nanoparticles over a cross-linked polysaccharide's matrix

To evaluate the deposition of nanoparticles (NP) into a matrix of chitosan cross-linked with dextran sulfate at a high and low DCL and alginate cross-linked with calcium ions, a quartz crystal microbalance with dissipation monitoring (QCM-D) (QSense from Biolin Scientific) was used. QCM-D measures the mass over a sensor (including the mass of water in the layer) by using the acoustic waves generated by an oscillating crystal quartz plate with piezoelectric properties (Dixon, 2008). The resonance frequency (f) will depend on the total oscillating mass including the mass of the sensor and the layers over it and by monitoring Δf is possible to detect changes in the mass with nanogram resolution. For a thin, rigid, and uniform films the mass deposited over the sensor can be calculated by the Sauerbrey equation:

$$\Delta m = -C \cdot \frac{\Delta f}{n} \quad (11)$$

where Δm is the change in mass of the added layer, C is a proportionality constant (mass sensitivity constant) that depends only on the intrinsic properties with a value of 17.7 ng/cm²s for quartz and Δf is the change in the resonance frequency (Hz) at the overtone n (number of the harmonic modes: 1,3,5,7..).

The changes in the dissipation energy ΔD of the oscillating crystal quartz are based on the time it takes to stop the oscillating after the current is off. This measurement is related to the viscoelastic properties of the layer over the sensor and is defined by:

$$D = \frac{E_{dissipated}}{2\pi E_{stored}} \quad (12)$$

where $E_{dissipated}$ is the energy dissipated during one oscillatory cycle and E_{stored} the energy stored in the oscillating system. A non-zero ΔD means that the layer over the sensor is not a rigid layer and has viscoelastic properties, i.e., keeps oscillating even after the current is off (Dixon, 2008). For both sets of experiments (alginate-calcium matrix and chitosan-dextran sulfate matrix), 14 mm diameter silica sensors were used as the surface for deposition of the model matrix. All experiments were run at a flowrate of 100 μ L/min and a stabilized temperature of 20 °C.

2.2.3.1 Alginate-calcium matrix QCM-D experiment

For each run, a baseline was established while washing the sensor with 1 mM CaCl₂. After achieving the baseline, the silica sensor was pre-coated with the poly-L-lysine

(PLL) solution (0.1% w/v) in 1 mM CaCl₂ followed by the 0.5% (w/v) alginate solution. The silica-alginate interaction is electrostatically unfavorable because both are negatively charged under the pH and ionic strength conditions used for this study. Adding a layer of positively charged PLL before introducing the alginate resulted in favorable electrostatic interactions between the alginate and the surface facilitating the formation of an alginate layer (Choi et al., 2015). Alginate cross-linking with calcium ions was performed in-situ by running a solution of 10 mM CaCl₂ (pH = 5.6) over the sensor after the deposition of the alginate layer. At this point, changes in the frequency (Δf) and in the dissipation energy (ΔD) were monitored over time to identify possible changes in the viscoelastic properties of the alginate matrix due to cross-linking by the calcium ions assuming that the alginate layer covered the entire surface of the PLL layer. For future similar experiments, it is recommended to verify if the compound of interest (in this case alginate) has formed a layer that covers the entire surface of the PLL layer to make sure the changes in the frequency and dissipation energy reported by the QCM-D are related with the alginate - CaCl₂ interactions. This verification can be done by using a reporter (e.g., nanoparticles) that based on favorable electrostatic interactions adsorbs to PLL but not to alginate analogous to the method previously used by Richter et al. (2003) to verify the surface coverage of a lipid solution over a silica surface by using B5 protein as a reporter of accessible silica.

To quantify the deposition of carboxylate-modified polystyrene NPs into the calcium cross-linked alginate matrix as a function of particle size, FluoSpheres obtained from Thermo-Fisher of 20 nm, 100 nm and 200 nm diluted in 1.3 mM CaCl₂ and 17.6 mM NaCl to a concentration of 10 mg/L were introduced into the QCM-D modules. The

particles were suspended in a solution of 1.3 mM CaCl₂ and 17.6 mM NaCl based on a previous determination of the ionic strength in an alginate and 10 mM CaCl₂ solution using inductively coupled plasma-optical emission spectrometry (ICP-OES). The change in mass deposited over the sensor due to NP deposition was calculated using equation (10). Data were collected beginning with the introduction of the PLL solution in 1 mM CaCl₂ and ending with a final rinse of a 1.3 mM CaCl₂ and 17.6 mM NaCl solution. All solutions were at similar pH around 5.6. Duplicate runs were performed for all conditions.

2.2.3.2 Chitosan-dextran sulfate matrix QCM-D experiment

For each run, a baseline was established for 100 mM NaCl. After achieving the baseline, a solution of 700 ng/μL of chitosan in 100 mM NaCl was introduced to form the first layer over the silica sensor followed by a rinse step with 100 mM NaCl. Then, a dextran sulfate solution of 700 ng/μL or 200 ng/μL was introduced for high or low DCL formation, followed by a rinse step with 100 mM NaCl. Carboxylated-modified polystyrene nanoparticles of 20 nm (FluoSpheres obtained from Thermofisher) were used as a model nanoparticle in a concentration range from 700 ng/uL to 50 ng/uL suspended in 100 mM NaCl. Each run was repeated in duplicate. All solutions were at similar pH around 7.01. The DCL was calculated from the potentiometric titration (Equation 9) and the change in mass due to NP deposition was obtained from the QCM-D data (Equation 11). These data provided a window into how DCL can alter nanoparticle deposition.

2.3 Results and Discussion

2.3.1 Calcium cross-linking can increase alginate matrix hydration and viscoelasticity

The QCM-D shifts in frequency and energy dissipation were recorded as a function of time and are presented in Figure 2.1 as average values for the 5th overtone. In step I of the experiment, we successfully deposited a layer of poly-L-lysine (PLL) onto the silica sensor. The mass of the PLL layer was consistent for all the runs with a shift in the frequency around -5 Hz. The corresponding shifts in the dissipation energy were below 3×10^{-6} , which indicates that the PLL layer was relatively rigid. The rinsing step after the PLL deposition (Step II in Figure 2.1) led to a small increase in the Δf and a decrease in ΔD to almost 0, indicating that the rinsing step removed all the weakly adsorbed PLL leaving a rigid layer of PLL over the silica sensor surface. Similar results were obtained previously by Choi et al. (2015). This PLL layer provided attractive electrostatic interactions for the deposition of alginate onto the PLL layer (De Kerchove & Elimelech, 2006) as seen by the decrease in Δf in step III. According to the changes in the dissipation energy observed in step III in all alginate deposition runs (a, b, and c from Figure 2.1), the alginate layer initially had rigid properties and then it became more viscoelastic as indicated by the increase in ΔD up to 12-14 until Δf stabilized.

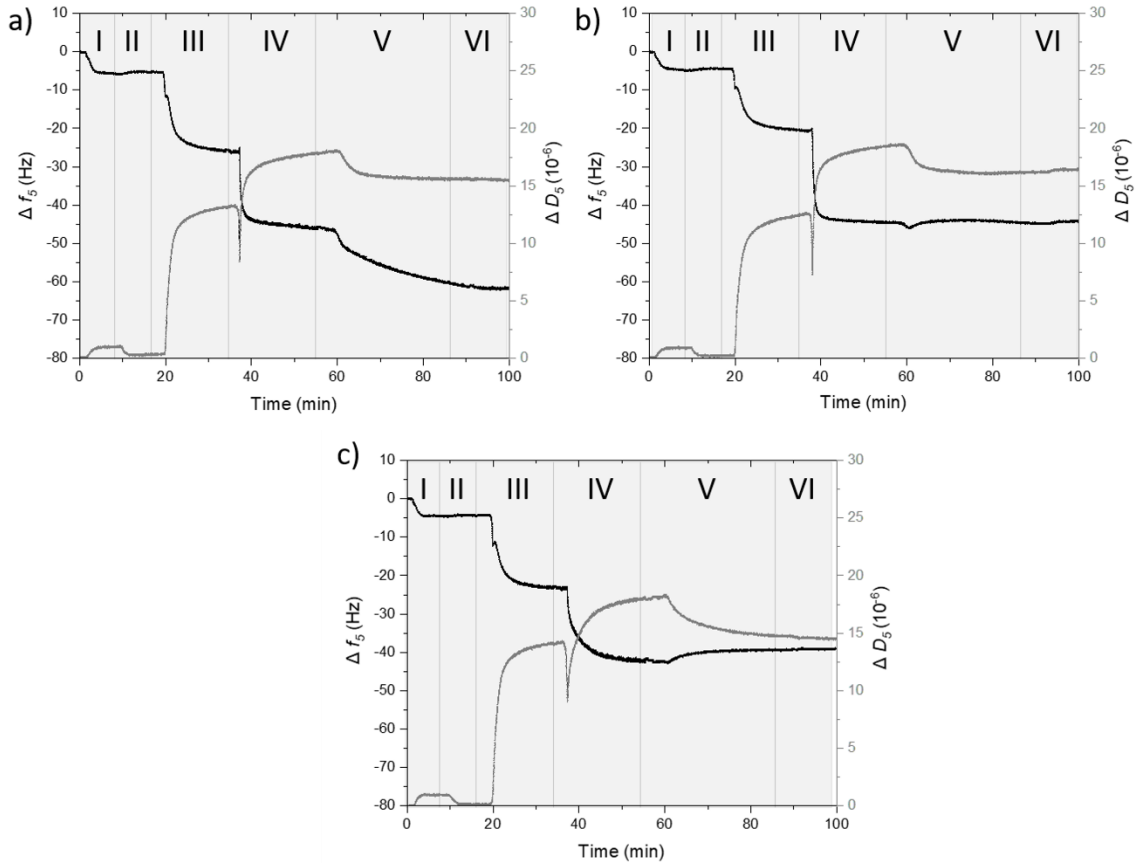


Figure 2.1: Changes in mass and dissipation energy for alginate matrices. QCM-D data for alginate-calcium matrices including (step V) the deposition of 20, 100 or 200 nm diameter NPs. Each step (I-VI) indicates the introduction of a solution with the component to be deposited over the silica sensor. The run started with the introduction of a PLL solution in 1 mM CaCl₂ (I), followed by a rinse with 1 mM CaCl₂ to remove the PLL loosely bounded to the silica sensor (II). Then a 0.5% alginate solution was introduced (III) and the alginate deposited over the sensor was cross-linked with a 10 mM calcium chloride solution (IV). Step (V) shows the deposition of a 10 mg/L COOH⁻ polystyrene NPs of a) 20 nm, b) 100 nm and c) 200 nm diameter suspended in a 1.3 mM CaCl₂ and 17.6 mM NaCl solution followed by a rinse with a solution with the same ionic strength (VI).

Figure 2.2 shows the graph of ΔD vs Δf for alginate deposition and cross-linking (steps III and IV in Figure 2.1). This graph provides insights on how the viscoelastic properties of the alginate layer change due to the cross-linking with calcium ions. The slope of the ΔD vs Δf is related to the energy dissipated per unit of mass absorbed (Vandeventer et

al., 2012). Initially, the PLL layer is rigid. Alginate adsorption onto the PLL layer increased the viscoelasticity as indicated by the slope changes in Figure 2.2. The alginate adsorption process initially had a lower slope ((1) in Figure 2.2), followed by a sudden increase in the slope ((2) in Figure 2.2), suggesting an increase in the viscoelastic properties, and ending with a linear slope indicating that the energy dissipated per unit of mass adsorbed was constant and that the viscoelastic properties of the alginate film reached a steady state.

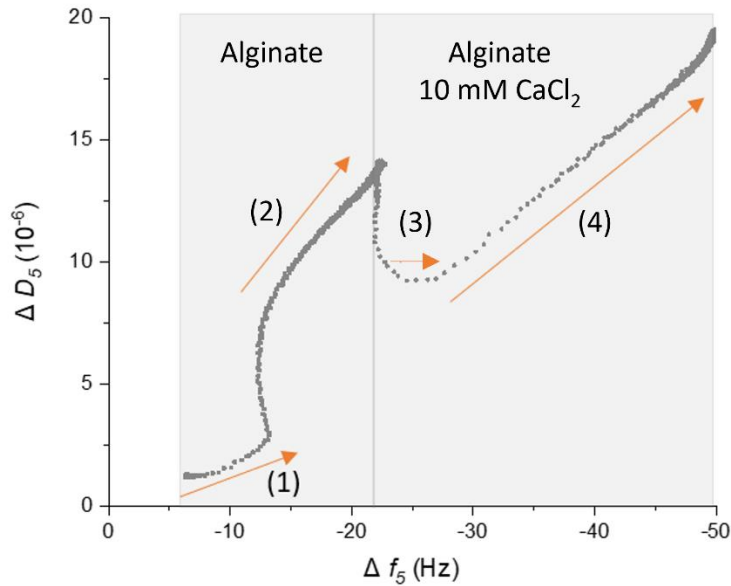


Figure 2.2: Changes in the dissipation energy (ΔD) as a function of the changes of the frequency (Δf) for 0.5% (w/v) alginate deposition over a PLL layer. The results presented are the average of the 5th overtone for steps III and IV (Figure 2.1) for all 6 independent runs prior to the addition of nanoparticles.

These results suggest that the first layer of alginate is strongly coupled with the PLL layer due to favorable electrostatic interactions ($pK_{a \text{ alginate}} = 3.3$ to 3.6 (K. Y. Lee, 2012), $pK_{a \text{ PLL}} = 10$ (Yaroslavov, Kuchenkova, Okuneva, Melik-nubarov, & Kozlova, 2003)) but as

the alginate layer built up, the alginate- alginate interactions could dominate. The decrease in the change of frequency as more alginate layers were deposited could be caused by both the addition of alginate chains and hydration of the layer which would lead to swelling. A similar analysis has been previously hypothesized by Vandeventer et al. (2012) in an analogous study of DNA adsorption to silica surfaces using QCM-D. Cross-linking of the alginate layer with calcium ions caused a decrease in Δf of about -25 Hz (Figure 2.1, Step IV). In QCM-D experiments changes in frequency are related to the effective mass deposited over the sensor, including the hydration water (bound water) to the film. When alginate is cross-linked with calcium ions, each calcium ion is coordinated by four oxygens from the alginate carboxyl groups as well as by oxygens from four molecules of water (Braccini & Pérez, 2001). This decrease in Δf may be related to an increase in the bound water due to the Ca^{2+} cross-linking. Similar behavior has been observed previously (De Kerchove & Elimelech, 2006; Kilan & Warszyński, 2014). The change in the dissipation energy shows a sudden decrease followed by an immediate increase after the introduction of the 10 mM CaCl_2 solution (Figure 2.1). Calcium cross-linking is expected to result in more stable junctions points, due to Coulombic interactions, compared to dilute solutions of alginate that form temporary networks due to chain entanglement. This change in junction stability is likely responsible for the decrease in viscoelasticity of the alginate immediately after exposure to the calcium ion solution (Wloka et al., 2004). The later increase in ΔD is characteristic of films with large amounts of co-adsorbed water which could be explained by an increase in hydration of the film due to water molecule binding by calcium ions and the

trapping of water molecules by hydrogen bonding inside the matrix (De Kerchove & Elimelech, 2006; Höök et al., 2001).

2.3.2 Nanoparticle deposition over a cross-linked alginate matrix is size dependent

In addition to the effects of calcium cross-linking on the viscoelastic properties of the alginate film, the deposition of carboxylated polystyrene nanoparticles (NPs) over the alginate cross-linked matrix as a function of the particle size was quantified. If we consider the carboxylated polystyrene NPs as rigid spheres and as discrete elements where the losses of the observed in dissipation energy are originated from the hydration coat dragged by the particle when deposited (Olsson, Quevedo, He, Basnet, & Tufenkji, 2013), we can calculate the net mass of particles deposited over the cross-linked alginate using the Sauerbrey equation (Equation 11) and the changes in frequency observed in stage V (Figure 2.1). In the specific conditions selected (pH, ionic strength, cross-linker agent concentration, and flowrate) for this QCM-D experiment, the deposition of the NPs will be driven mainly by the available void space in the alginate cross-linked matrix relative to the particle size and the possible electrostatic interactions between the carboxylated polystyrene NPs and the alginate - Ca^{+2} matrix. Experiments in where the pH of the buffer solution varies below and above the carboxylated groups pK_a could help to elucidate the effects of the favorable and unfavorable electrostatic forces on the NPs deposition over an alginate – 10 mM Ca^{+2} matrix.

Figure 2.3 shows the results from the mass calculation for each particle size under study. The 20 nm and 100 nm particles were able to deposit over the matrix resulting in an increase in the mass over the sensor ($52 \pm 8 \text{ ng/cm}^2$ and $3 \pm 1 \text{ ng/cm}^2$ respectively). The

deposition of the 20 and 100 nm particles decreased ΔD suggesting that the deposition of these particles caused a decrease in the viscoelasticity of the film due to dehydration of the film or due to the particle's deposition adding their intrinsic rigidity. The increase in mass by the 20 nm particles was significantly higher compared to the minimal increase in mass by the 100 nm but still both caused almost the same decrease in the ΔD . A possible explanation for this behavior is that the void space of the matrix is close to 100 nm, restricting the number of 100 nm particles that were able to penetrate the cross-linked alginate matrix making the ratio of the mass of particles getting into the matrix to the water mass released due to dehydration close to 1. The 200 nm particles, which were the largest particles used in this study, increased the change in frequency, indicating a decrease in the mass over the sensor of $11 \pm 3 \text{ ng/cm}^2$ (Figure 2.3) In terms of the ΔD , the 200 nm particles caused a decrease in the change of the dissipation energy higher than the one caused by the 20 and 100 nm particles. It is possible that 200 nm particles are big enough to remove loosely bound alginate chains due to the binding of the NP carboxylated groups with Ca^{2+} ions. To determine the relative effects of the matrix void space, the electrostatic interactions of the NPs and the matrix

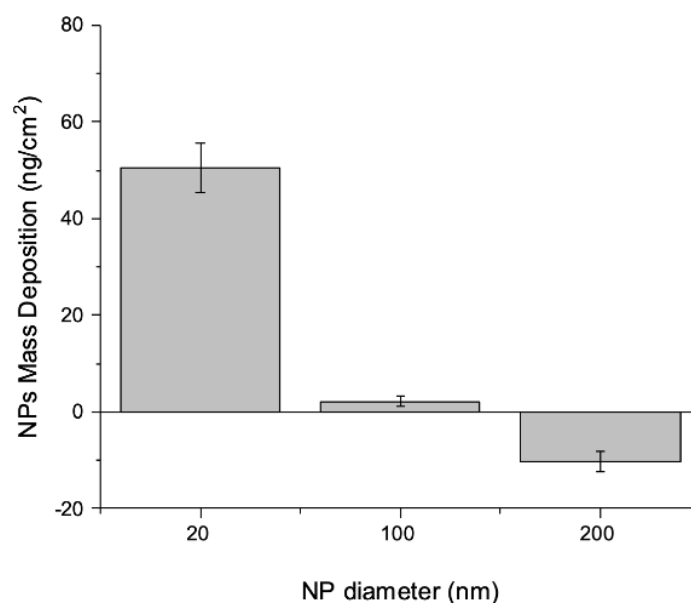


Figure 2.3: Average mass of NPs deposited over the 0.5% alginate matrix cross-linked with a 10 mM CaCl₂ solution. Deposition of 20 nm and 100 nm particles over the matrix increased the mass over the silica sensor. The introduction of the 200 nm particle solution decreased the mass deposited over the sensor, which suggests that these large particles may be able to remove loosely bound alginate chains.

2.3.3 The degree of cross-linking limits the deposition of nanoparticles

To evaluate how the degree of cross-linking (DCL) could limit the deposition of 20 nm carboxylated polystyrene nanoparticles (NPs) we prepared solutions of chitosan and dextran sulfate at a high and low degree of cross-linking (DCL) as described in Section 2.2.1. In order to measure the DCL we performed a potentiometric titration and used Equation 9 to calculate the DCL based on the method of Skoog et al. (1996). Duplicate titrations curves for each sample are presented in Figure 2.4. Samples containing only chitosan (orange curves in Figure 2.4) were used to calculate the free amine groups available for cross-linking in a solution of 700 ng/μL and 100 mM NaCl using Equation

10. The average $[-\text{NH}_2]_{\text{T}}$ was 2.6 ± 0.52 mg. The concentration of free amine groups after cross-linking ($[-\text{NH}_2]$) decreased for both high DCL and low DCL conditions. For the high DCL, the data from the yellow curves from Figure 2.4 were used and the average $[-\text{NH}_2]$ was 0.96 ± 0.21 mg. In the low DCL conditions the $[-\text{NH}_2]$ was higher with an average value of 2.4 ± 0.09 mg, a concentration close to $[-\text{NH}_2]_{\text{T}}$.

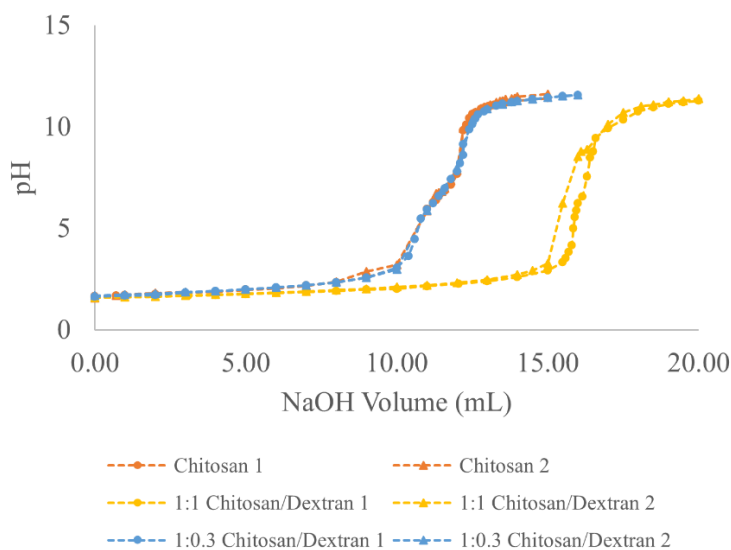


Figure 2.4: Titration curves for the determination of free amine groups before and after cross-linking. The titration curve from Chitosan samples 1 and 2 was used to determine the $[-\text{NH}_2]_{\text{T}}$. This concentration corresponds to the amine groups that are available for cross-linking for $700 \text{ ng}/\mu\text{L}$ of chitosan in 100 mM NaCl . The titration curves for 1:1 Chitosan/Dextran (High DCL) and 1:0.3 Chitosan/Dextran (Low DCL) samples were used to calculate the concentration of $[-\text{NH}_2]$, which corresponds to the free chitosan amine groups after the cross-linking.

The potentiometric titration is based on the addition of HCl to protonate the free amine groups available in the chitosan complex followed by the neutralization of the remaining acid (HCl) volume with the NaOH base. The shift to the right of the 1:1 chitosan/dextran titration curve indicated that fewer free amine groups were available after the cross-

linking, resulting in a higher volume of NaOH needed to neutralize the remaining acid (1:1 neutralization reaction) (Skoog et al., 1996). Calculating the DCL based on equation 9, in the low DCL condition (200 ng/ μ L of dextran sulfate) 92.3% of the amine groups were free after cross-linking resulting in a DCL of 7.69%. In the high DCL condition (700 ng/ μ L of dextran sulfate), the free amine groups concentration after cross-linking was 36.9% for a DCL of 63.1%. Based on these results the degree of cross-linking (DCL) of a polyelectrolyte complex like the cationic chitosan and anionic dextran sulfate can be controlled by adjusting the concentration of the polymers. The method used to determine the DCL percentage seems to be more sensitive at a high DCL. The anionic sulfate groups in the dextran sulfate could affect the inflection points of the titration curves due to non-selective protonation of the sulfate groups in the dextran sulfate instead of the amine groups of the chitosan. For a more selective quantification of free functional groups other analytical methods should be considered like Fourier-transform infrared spectroscopy (FTIR) or chromatography (El Mansouri & Salvadó, 2007).

To determine how the DCL of the chitosan/dextran sulfate matrix could affect the accumulation of nanoparticles we used the QCM-D technique and calculated the mass of 20 nm carboxylated polystyrene NPs (hydrodynamic diameter in 100 mM NaCl measured by Dynamic Light Scattering, $d = 39.70 \pm 9.29$ nm) that could get into the high and low DCL chitosan/dextran sulfate matrices. The mass of nanoparticles accumulated in both matrixes were calculated using Equation 11 for a variety of nanoparticle concentrations (Figure 2.5).

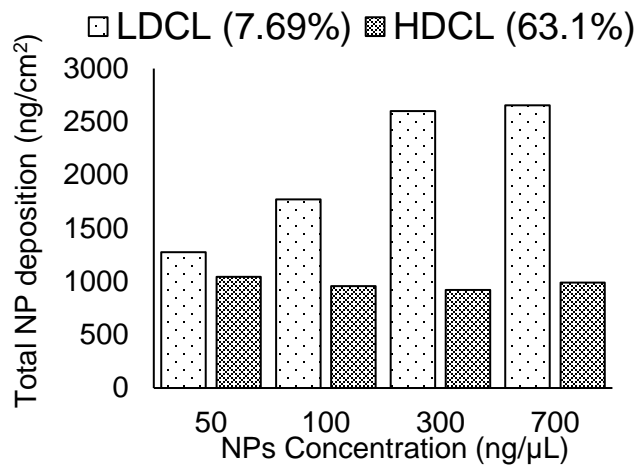


Figure 2.5: Relation between DCL and 20 nm NP accumulation in chitosan/dextran sulfate cross-linked matrices. The number in parentheses indicates the percent of cross-linking.

The deposition of the NPs over the chitosan/dextran sulfate matrix was influenced by the DCL. In the chitosan/dextran sulfate matrix with a low DCL (7.69%), the deposition of the NPs was almost 40% higher than in the matrix with a high DCL (63.1%) (Figure 2.5). In the high DCL matrices the maximum total NP deposition was 1044 ng/cm² while in the low DCL samples the maximum total NP deposition was 2655 ng/cm². NP deposition was independent of NP concentration in the high DCL matrices but increased linearly for low DCL matrices. In a matrix with a high DCL, the interstitial voids of the matrix are likely to be smaller than in a low DCL matrix, which could reduce the penetration of the nanoparticles to deeper layers of the matrix thereby reducing the overall accumulation of NPs. However, it seems that there is a limited void space in the matrix for the particles to accumulate. In the case of the low DCL matrix, the chitosan/dextran sulfate matrix reaches the maximum accumulation at 2600 ng/cm² compared to the high DCL where is reached at around 1000 ng/cm². In addition to the interstitial space due to the structural

features of the chitosan/dextran sulfate matrix, the electrostatic forces between the particles and the polymers could play a role in the NP accumulation. Carboxylated polystyrene nanoparticles have an anionic surface due the COOH- groups on their functionalized surface. As mentioned before, the low DCL chitosan/dextran sulfate have a higher concentration of free amine groups compared to the high DCL matrices ($[-\text{NH}_2]_{\text{low DCL}} = 2.4 \pm 0.09 \text{ mg}$, $[-\text{NH}_2]_{\text{high DCL}} = 0.96 \pm 0.21 \text{ mg}$) making the electrostatic interactions between the NPs and the polymeric matrix more favorable in the low DCL samples resulting in an increase in particle deposition.

2.4 Conclusion

The experiments presented in this chapter provided initial insights on how cross-linking can increase the viscoelasticity and hydration of the polymeric matrix and affect the deposition of nanoparticles. Cross-linking can affect the rigidity and stability of the alginate and the magnitude of these effects should depend on the cross-linking agent concentration leading to the formation of different DCL. For this study we used a calcium concentration of 10 mM, further studies may be needed to evaluate how cross-linking agent concentrations can affect the DCL and restrict or promote NP accumulation in biofilms.

NP size is a property that can limit accumulation in polymeric matrices, depending on the size of the particle relative to the void space of the matrix. The smaller the particle to void size ratio, the higher the mass of particles that could be deposited. However, polymeric matrixes have a maximum level of NP deposition at which depending on the

DCL the interstitial spaces can get full and restrict the deposition of more particles.

Another factor that can influence NP deposition is the electrostatic interactions which are influenced by the free functional groups of the polymeric matrix. A low DCL will result in polysaccharides with a higher concentration of free functional groups, resulting in an increase in NP deposition if electrostatic forces are favorable. The deposition of NPs in the calcium cross-linked matrix decreased the viscoelasticity and hydration of the alginate matrix indicating that the deposition of particles in polymeric films can induce changes in the matrix.

The strategy presented in this Chapter is a simplified approach to reduce the complexity of an EPS matrix in a biofilm. The results from this study aid in our understanding and provided initial insights on how the viscoelastic properties and concentration of the individual EPS components, the NP concentration and size, and the composition of the surrounding bulk solution can affect the time course of interaction of NPs with biological matrices. Biofilms are ubiquitous in nature. In environmental systems and even in some engineered systems (e.g. bioreactors in WWTP) the concentration of biofilm cross-linking agents such as calcium or other EPS component with cross-linking capability (Jennings et al., 2015), as well as the bulk solution chemistry (e.g., pH, which will have implications on the electrostatic interactions of biofilms – NPs) will vary depending on the conditions of the system. The result from this study suggests that by controlling the properties and concentration of the cross-linking agent (that could be present in the surrounding bulk solution in environmental systems) the viscoelasticity and void size of the EPS biofilm matrix could be manipulated to increase or decrease the deposition of

NPs into the biofilm taking in consideration also the NP physicochemical properties (e.g., surface chemistry and size). Further studies are needed to support and verify the results presented in this chapter.

CHAPTER 3

HETEROGENEOUS DIFFUSION OF POLYSTYRENE NANOPARTICLES THROUGH AN ALGINATE MATIX: THE ROLE OF CALCIUM CROSS- LINKING AND NANOPARTICLE PARTICLE SIZE

3.1 Introduction

While biofilms are known to interact with NPs, the fundamental mechanisms that govern NP diffusion in biofilms are unknown. Previous studies of the diffusion of particles and molecules through biofilms have focused on the measurement of average, effective diffusion coefficients (Stewart, 1998, 2003). However, due to local heterogeneities of the EPS in terms of structure and composition, diffusion coefficients are not expected to be uniform across the biofilm matrix (Liao et al., 2012; Renslow et al., 2010; Stewart, 1998).

In this chapter we present the results from a study in where we used alginate gels as a model for biofilm EPS and comparatively investigated NP movement in alginate gels and in calcium cross-linked alginate gels. We evaluated the effects of calcium cross-linking on NP movement and its relationship with the NP diameter.

3.1.1 Specific Objectives

The focus of this study is on the fine porous structure of biofilm and its effect on NP movement and accessibility. In this study, we used image correlation methods and single particle tracking to characterize the heterogeneous behavior of NPs in biofilms and map a

detailed representation of the structure and connectivity of pores within the alginate matrix.

The specific objectives of this study were to:

- 1) to characterize the movement of carboxylated polystyrene NPs in a structurally heterogeneous alginate matrix, and
- 2) to investigate the effects of cross-linking on the diffusion coefficients and diffusive mode of NPs as a function of NP size.

3.2 Materials and Methods

3.2.1 Model polysaccharide matrix

To study how polysaccharide cross-linking affects the structure of a biofilm matrix and the transport of NPs, alginate was used as an anionic model polysaccharide. A solution of 0.5% (w/v) alginate (alginic acid sodium salt, CAS:9005-38-3 Sigma-Aldrich) was prepared by adding 0.250 grams of alginate to 50 milliliters of Milli-Q water. The solution was under continuous mixing overnight to completely dissolve the alginate powder in the water. To cross-link the alginate, a stock solution of CaCl_2 was prepared and added to the alginate solution for a final concentration of 10 mM CaCl_2 . The divalent calcium ion can serve as a cross-linking agent to affect the structure and thickness of biofilms by ionic bridging of EPS components. Alginate (cross-linked with calcium) has the same type of cross-linking mechanism and rheological behavior as the EPS, making it an appropriate model for this study (Wloka et al., 2004).

3.2.2 Sample preparation

To study the transport of NPs through a cross-linked and non-cross-linked alginate matrix, a custom clear silicon template (Kisley et al., 2015) with dimensions summarized in Figure 3.1 (43018M by Grace BioLabs) was placed over a coverslip and an aliquot of 25 μL of 0.5 % (w/v) alginate in water with or without CaCl_2 (10 mM) was added to the silicon well. Following alginate polymerization and immediately before imaging, 5 μL of NP suspension (5.3×10^9 particles/mL) was pipetted on top of the alginate matrix previously added to the well.

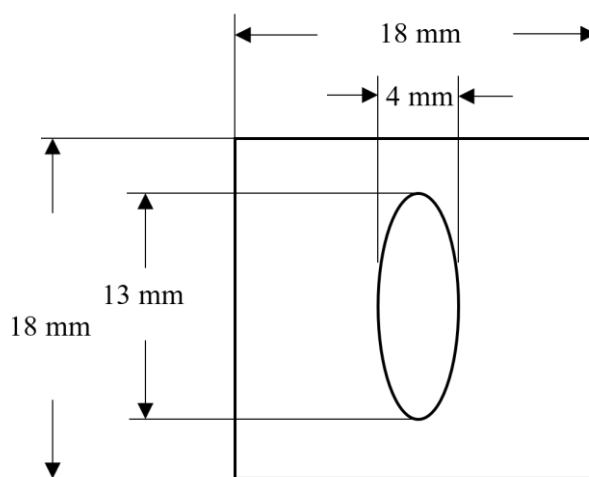


Figure 3.1: Schematic of the clear silicone template. The gasket was a custom design obtained from Grace BioLabs. The design was used and described previously by Kisley, et al. (2015).

The NPs used in this study were fluorescent anionic carboxylate-modified polystyrene beads with diameters of 20 nm, 100 nm and 200 nm, (Invitrogen FluoSpheres, max abs/em: 580/605). Anionic carboxylate-modified polystyrene beads were used as an NP model to minimize attractive interactions between the NPs and the anionic alginate (Kisley et al., 2015). The samples were covered with an additional coverslip to prevent

dehydration. The sample preparation, microscopic data acquisition and methods used for image analysis are summarized in Figure 3.2.

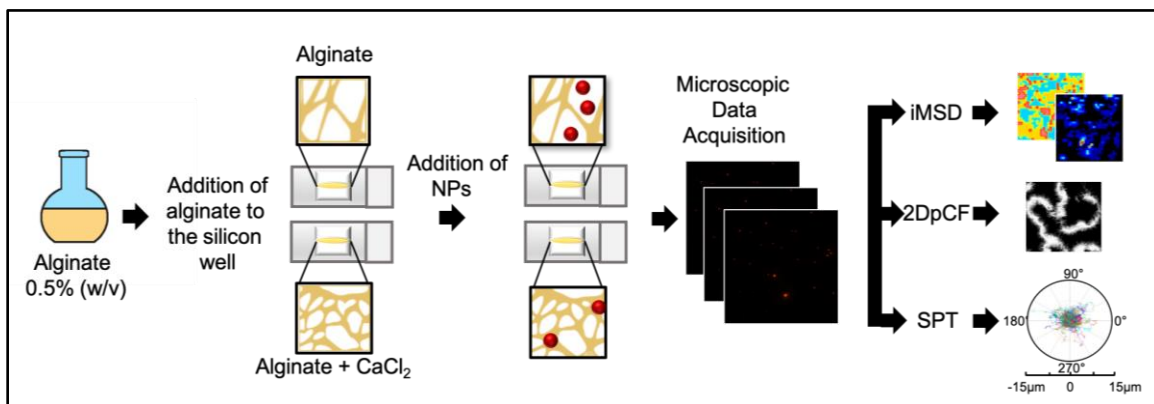


Figure 3.2: Diagram that shows the flow of the sample preparation, data acquisition and data analysis. For the data analysis we used image Mean Square Displacement (iMSD), two-dimensional pair correlation function (2DpCF) and single particle tracking (SPT).

3.2.3 Microscopic data acquisition

The samples were observed using total internal reflection fluorescence (TIRF) imaging on a Nikon N-Storm Super-Resolution Microscope System with a Hamamatsu ORCA-Flash 4.0 detector. In TIRF microscopy, the excitation beam is reflected off the coverslip and only fluorophores in the exponentially decaying evanescent field with a depth of 200 nm are excited and can be observed (Mattheyses, Simon, & Z Rappoport, 2010). TIRF imaging allowed analysis of NP diffusion only in two dimensions, x and y, parallel to the coverslip. For each sample, 12,000 frames of data were collected at a rate of 490 frames/s using a 100X NA 1.4 TIRF objective. The red fluorescent NPs were excited with a 561 nm laser and a laser power of 23 mW (30% of the maximum, 75 mW, fiber output for 561 nm) for 20 and 100 nm diameter NPs and 11 mW (15% of the maximum) for the 200

nm diameter NPs. The laser power selected was the minimum laser power needed to clearly observe the FluoSpheres, avoiding pixel saturation and reducing fluorophore photobleaching. For each sample (sample 1 and sample 2) three fields of view of 256 x 256 pixels (0.06 $\mu\text{m}/\text{pixel}$) were recorded to collect images from different locations of the sample (Figure 3.3).

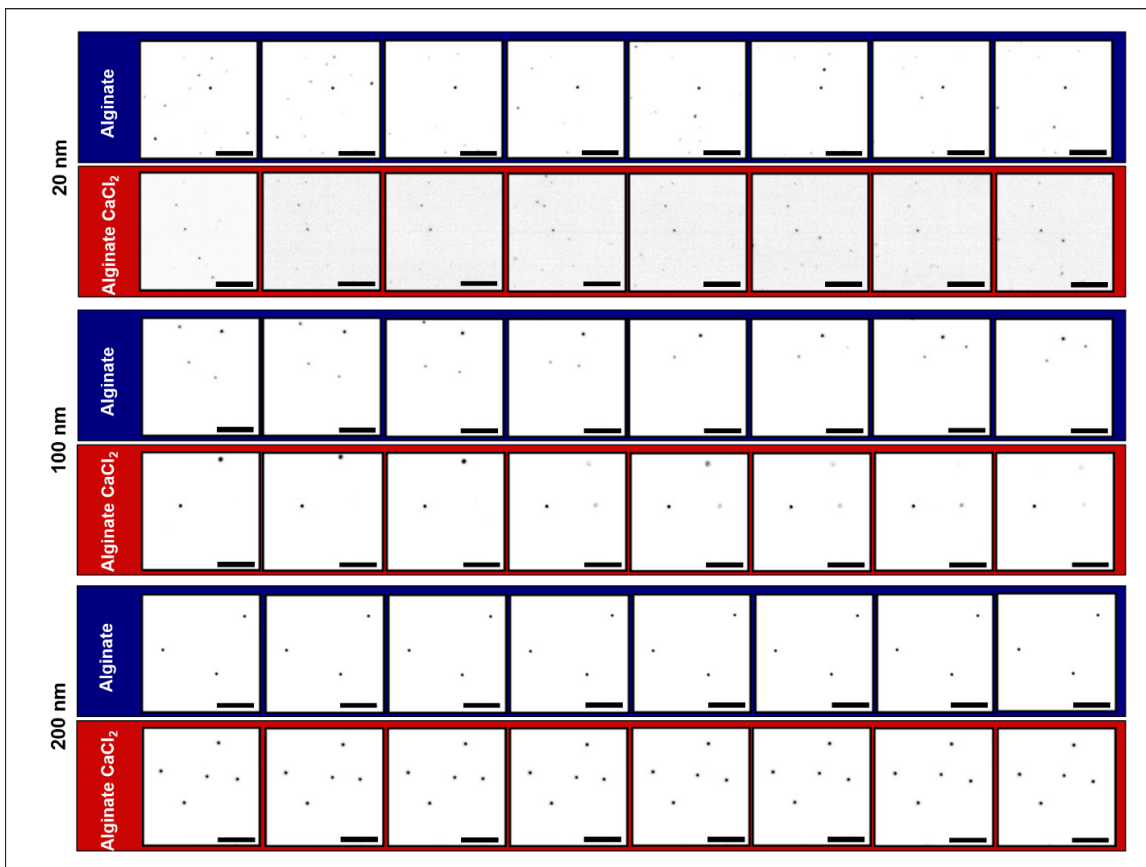


Figure 3.3: A 9 frame section of the 12,000 frame microscopy data collected for 20 nm, 100 nm and 200 nm particles. The 12,000 frames were collected at a frame rate of 490 frames/s, but the frames presented here are every 20th frame in order to capture the particles' movement. The images were color inverted for visualization purposes, but the analysis was done with the images in their original colors (white particles and black background) The scale bar (black) in each frame is 5 μm .

Dynamic light scattering (DLS) Malvern Zetasizer NS (Worcestershire, U.K.) was used to measure the hydrodynamic diameter of the nanoparticles in the ionic strength and pH of the sample after cross-linking the alginate matrix with CaCl_2 . The ionic strength of the alginate sample after the cross-linking process was determined to be 11.4 mM by inductively coupled plasma-optical emission spectrometry (ICP-OES) and the pH= 5.6 was measured using the Thermo Scientific Orion Star A211 benchtop meter. DLS was used to evaluate possible aggregation of the particles during the time it takes to collect TIRF microscopy images (around 60 minutes per sample). The hydrodynamic diameter of all the NPs under study (20, 100 and 200 nm) did not change with time indicating that there was no observable aggregation on the time scale of the experiments (Figure 3.4).

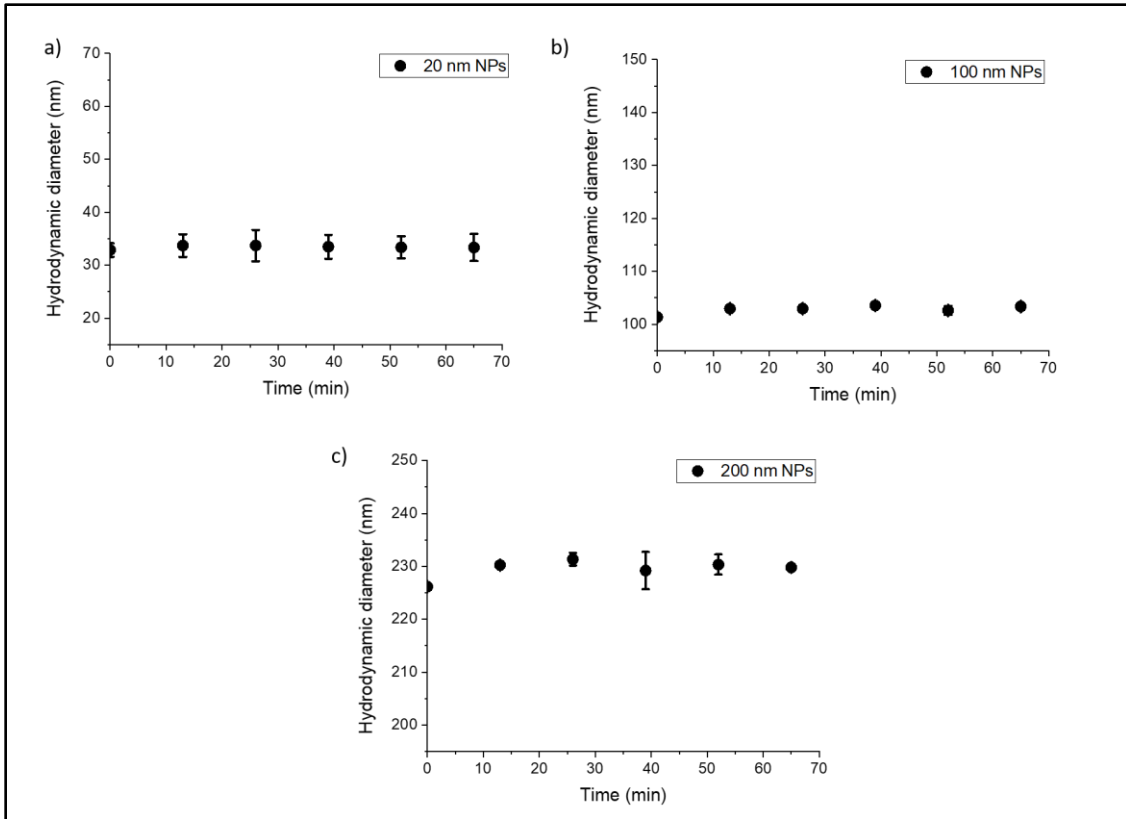


Figure 3.4: Hydrodynamic diameter of NPs used in the study in a solution of 11.4 mM total ionic strength and pH= 5.6. The dots show the mean of 3 independent measurements and the error bars are the standard deviation.

3.2.4 Methods used for the microscopy data analysis

To characterize NP diffusion and the structural features of the alginate matrix, the microscopic images were analyzed using correlation analysis and single particle tracking. To determine whether NP diffusion is isotropic or directional (anisotropic), two-dimensional pair correlation function (2D-pCF) was used to calculate anisotropies (Figure 1.8) and to generate connectivity maps. A detailed description of this method can be found in Chapter 1. 2D-pCF was an appropriate method to visualize features of the polymeric hydrogel matrix that require high spatial resolution (e.g., barriers for NP

diffusion) because it does not rely on a spatial average. The analysis was performed using a pCF pixel distance of 4, detecting temporally and spatially correlating fluorescence at a random adjacent location at a maximum distance of 0.24 μm (4 pixels) away. For the connectivity maps, the arrow length (line length) selected was 5 pixels (0.3 μm). Single particle tracking (SPT) was used to analyze individual tracks of the NPs moving through the alginate matrices, obtain mean square displacement (MSD) curves and to perform a particle count (from an image of the 80% of the total area of the sample, Appendix A). The SPT analysis was done using the algorithm in the NIS-Elements software (Nikon's universal software platform) (Jaqaman et al., 2009). Please refer to Chapter 1, section 1.4.1, for more details of this algorithm. In the case of this study, a random motion model was selected, and it allowed gaps in tracks of a maximum size of 5 frames based on the average time a particle stayed visible in the microscopic images. All trajectories longer than 20 frames were selected; shorter tracks were not considered in the analysis. For the identification and visualization of the spatial distribution of diffusion modes and NP diffusion coefficients (D), an image Mean Square Displacement (iMSD) analysis was performed. One of the advantages of using iMSD, as discussed in Chapter 1, is that based on the calculation of mean square displacements (MSD), the diffusion coefficient will be visually presented in the same spatial location where it was measured in the form of maps (Malacrida, Rao, et al., 2018). The iMSD method was used to identify and visualize the spatial distribution of diffusion modes and the diffusion coefficients (D) of NPs moving in the non-cross-linked and cross-linked alginate network. For the iMSD analysis, a region of interest (ROI) of 32 x 32 pixel and a moving window with an ROI overlap of $\frac{1}{4}$ (8 X 8 pixels) was selected for the scanning analysis. The data was analyzed using the

“all models” option for diffusion (free diffusion, confined, and partially confined) because a wide variety of diffusion behaviors was observed in the microscopic images.

3.2.5 Statistical Analysis

Statistical analysis comparing the difference between the histograms of diffusion coefficients obtained by the iMSD analysis was performed in R using the permutation test of symmetry where the levels of the various conditions were treated as having paired or repeated data. The R coding for this analysis can be found in Appendix C. If the p-value was lower than 0.05 then the null hypothesis that there was no difference between the distributions was rejected. For the statistical comparison of the particle count and anisotropy values, a Two- Sample T-test was run in Minitab 19 using the average value and standard deviation of all three fields of view observed.

3.3 Results and Discussion

3.3.1 Nanoparticle accessibility to the alginate matrix cavities

As mentioned before, in TIRF microscopy only fluorophores in the exponentially decaying evanescent field with a depth of 200 nm are excited and can be observed. To reach the 200 nm of the alginate network closest to the coverslip, imaged NPs must move from the top of the 1 mm thick alginate gel (where the NPs were added) through the alginate matrix. The mobility of the 20 nm, 100 nm and 200 nm particles through an alginate matrix with and without cross-linking was then evaluated from TIRF microscopy images (see Figure 3.3 for a representative image). The average particle count obtained from SPT for each condition under study is presented in Table 3.1. For 20 nm particles,

26% fewer particles were observed after cross-linking. This percentage was calculated 1) using an unprocessed image of 80% of the total area of each well from two independent samples (Appendix A) and 2) assuming that the maximum number of NPs that were able to move through the 1 mm alginate layer and be imaged near the opposite surface are the number of NPs identified in the alginate only sample.

Table 3.1: Average particle count before and after cross-linking (calculated based on one frame (2 msec) and an area of 128, 169 μm^2 for two independent samples).

20 nm NPs		100 nm NPs		200 nm NPs	
Alginate	Alginate CaCl ₂	Alginate	Alginate CaCl ₂	Alginate	Alginate CaCl ₂
938 ± 255	702 ± 107	519 ± 16	124 ± 17	210 ± 41	90 ± 10

In the case of the 100 nm and 200 nm particles, cross-linking also decreased the number of particles identified. As expected, the results showed an inverse relation between particle size and the number of imaged particles, with the number of particles identified decreasing with increasing particle size. The connectivity maps, which illustrate the space within matrix that the NPs are able to access, also showed size dependent differences (Figure 3.5).

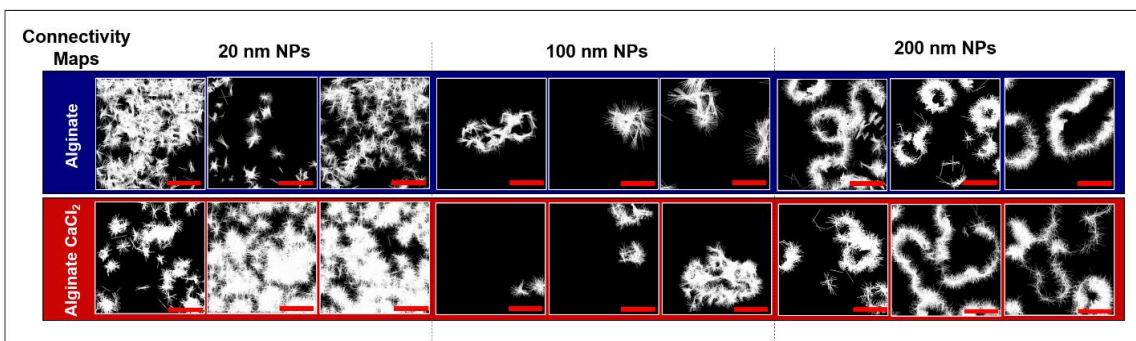


Figure 3.5: Connectivity maps for all three fields of view ($15.4 \times 15.4 \mu\text{m}$) obtained by 2D-pCF analysis for the 20, 100 and 200 nm NPs detected in the TIRF evanescent field. Each row shows each field of view analyzed for an alginate and a cross-linked alginate matrix. The scale bar (red) in each map is $5 \mu\text{m}$.

The 20 nm NPs move in areas that are less defined, smaller and morphologically more heterogeneous than the 100 and 200 nm particle paths. The 200 nm particles move within areas that are defined and connected. The 100 nm particles seem to face a mix of diffusion barriers encountered by the 20 nm and 200 nm NPs. These results suggest that the alginate matrix is a heterogeneous network composed of voids of different sizes and shapes. Depending on the size of NPs, these voids restrict the movement and accessibility of NPs from one point to another (e.g., top to bottom).

3.3.2 Nanoparticle movement through the alginate matrices is anisotropic

The polymer cross-linked network forms randomly in these gels with, presumably, no preferred orientation of pores and channels which would, when considering all the particles, result in isotropic motion. However, the anisotropy values obtained from the 2D-pCF analysis suggest that NP motion is anisotropic (Table 3.2). TIRF imaging occurs close to the coverslip, and it is possible that the surface partially constrains pore and

channel orientation resulting in anisotropic motion. Cross-linking did not have a statistically significant effect on the anisotropy values (p-value_{20nm} = 0.08, p-value_{100nm} = 0.07 and p-value_{200nm} = 1.0), indicating that the organization of the cavities that NPs can access (depending on their size) is not affected by the cross-linking.

Table 3.2: The averaged anisotropy values obtained from the 2D-pCF analysis for each nanoparticle size considered in this study for sample 1.

20 nm NPs		100 nm NPs		200 nm NPs	
Alginate	Alginate CaCl ₂	Alginate	Alginate CaCl ₂	Alginate	Alginate CaCl ₂
0.47 ± 0.06	0.60 ± 0.03	0.38 ± 0.03	0.62 ± 0.11	0.32 ± 0.06	0.32 ± 0.05

However, cross-linking did influence the directional path lengths (i.e., the length of a track along a specific angle) as it can be seen in the tracks presented in Figure 3.6. In a cross-linked alginate network, the directional path length of NPs increased as NP size decreased. The total distance traveled by a single particle, considering backwards and forward movements, was longer for the 200 nm NPs. When the results for the different size NPs were compared, the 200 nm NPs were more likely to travel the same path more than once than were the 20 or 100 nm NPs as indicated by the track line thickness in Figure 3.6. This pattern of movement suggests that the cavities of alginate networks (at an alginate concentration of 0.5 % w/v) could have a length scale around 200 nm in size. In such a case, for the 200 nm particles, the accessible area would be close to their size, restricting the motion of the particle and causing collisions between the NPs and the alginate making the particle move in a back and forth manner until they are able to escape the area of confinement and proceeding to a neighboring cavity. This behavior was also

visualized in the connectivity maps of the 200 nm particles (Figure 3.5) with more clearly defined channels available to the NPs. In addition, in both the non-cross-linked and cross-linked alginate matrix, the 20 nm particles traveled a greater net distance than the 100 nm or the 200 nm particles (Figure 3.6). One possible reason is that the alginate matrix has narrow passages that are easier to access by the 20 nm particles.

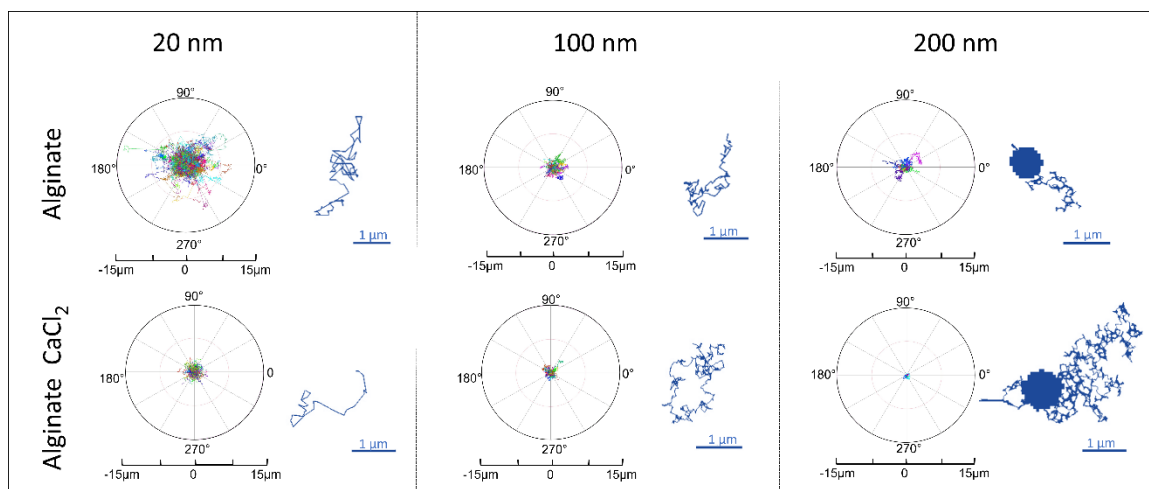


Figure 3.6: Polar graphs of individual tracks (from SPT) of all three fields of view of 20, 100 and 200 nm NPs through an alginate and a cross-linked alginate matrix. Each track has an assigned color that represents a single particle with the origin representing the particle initial position. All the particle tracks for the three fields of view are presented in the polar graph for each alginate matrix condition and particle size.

3.3.3 Cross-linking decreases NP diffusion coefficients in a size dependent manner

The movement of NPs in the alginate matrix can be described quantitatively by the diffusion coefficient (D) and D can be calculated from the images using iMSD. While the SPT analysis can also be used to determine D , the correlation methods used in iMSD (Malacrida, Rao, et al., 2018) can also generate maps revealing variations in D as a function of x-y position in a matrix (Figure 3.7).

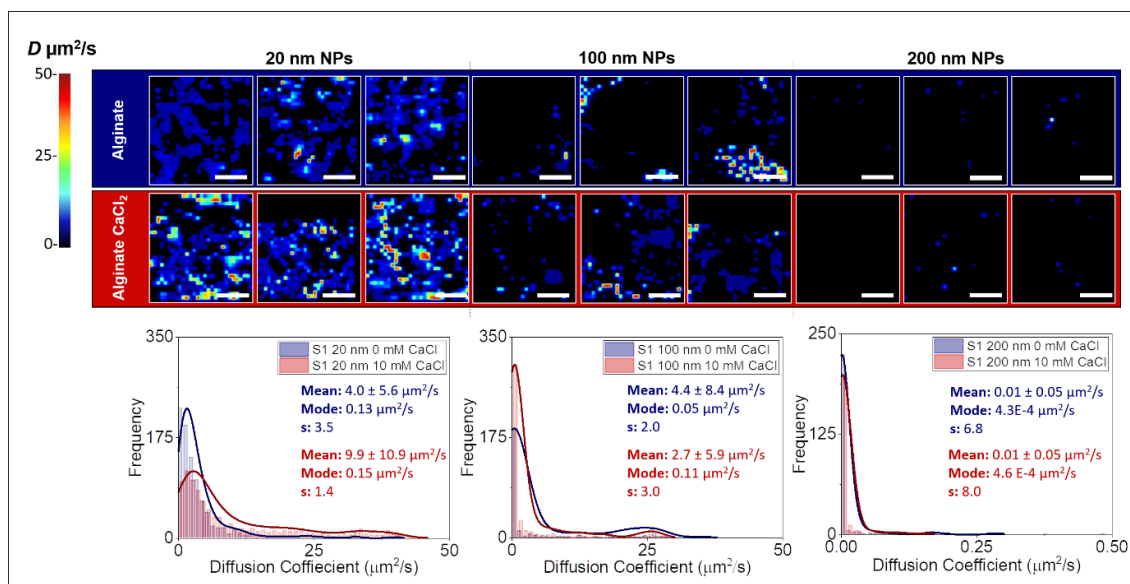


Figure 3.7: Visual maps and diffusion coefficient histograms for each NP size obtained from the iMSD analysis. The bars are histograms with bins sizes of $1 \mu\text{m}^2/\text{s}$ for the 20 and 100 nm NPs and $0.01 \mu\text{m}^2/\text{s}$ for the 200 nm NPs. The lines are kernel (Scott) probability density estimates of the diffusion coefficient (D) distributions. Each row shows each field of view analyzed for each condition. The D maps color scale goes from black to red. The red areas are the areas with higher D values and the darker areas the ones with the lower D values. The color-coded values in the distribution graphs are mean, mode and skewness (s) values of the D distributions taking in consideration all 3 fields of view analyzed. The scale bar (white) in each map is $5 \mu\text{m}$.

These maps showed high spatial variability of D for 20 nm particles, ranging between 0 and $50 \mu\text{m}^2/\text{s}$, and the variability decreased for both the 100 and 200 nm particles. With an increase in NP size, particle diffusion appears to be limited as indicated by the decrease in the average D . Calcium cross-linking has a statistically significant effect only in the D distribution of the 20 nm and 100 nm particles (p-value_{200nm} = 0.01 and p-value_{100nm} = 0.02). There was no statistical difference between the D distributions for the 200 nm particles (p-value_{200nm} = 0.6) in both matrices.

The 20 nm particles have a smaller D and a narrower distribution in a non-cross-linked alginate ($D = 4.0 \pm 5.6 \mu\text{m}^2/\text{s}$) than in the cross-linked ($D = 9.9 \pm 10.9 \mu\text{m}^2/\text{s}$), as

indicated by the positive and higher skewness values ($s = 3.4$ and $s = 1.4$). The smaller D for the 20 nm particles in the alginate only matrix could be related to the greater number of NPs in the observed area (Table 3.1), making the matrix more crowded and therefore, minimizing the diffusion of the 20 nm NPs (lower D).

To determine if the high concentration of the 20 nm particles could be the reason for the decreased diffusion coefficient in the alginate sample, an alginate sample (without calcium) was exposed to half of the original 20 nm particle concentration. The diffusion coefficient increased from $4.0 \pm 5.6 \mu\text{m}^2/\text{s}$ to $14.4 \pm 12.7 \mu\text{m}^2/\text{s}$ and the percentage of areas showing free diffusion increased from 27% to 65%, which confirms that it is likely that the lower D in the alginate matrix compared to the calcium cross-linked for the 20 nm NPs is related to the high concentration of particles in the volume making the matrix more crowded (Figure 3.8). With an increase in particle number within the alginate matrix, particle movement changes as a result of inter-particle interactions (Poling-Skutvik et al., 2016) and crowding. One likely inter-particle interaction is the repulsive electrostatic forces due to the anionic carboxylated polystyrene NPs (zeta potential = $-30.9 \pm 1.61 \text{ mV}$).

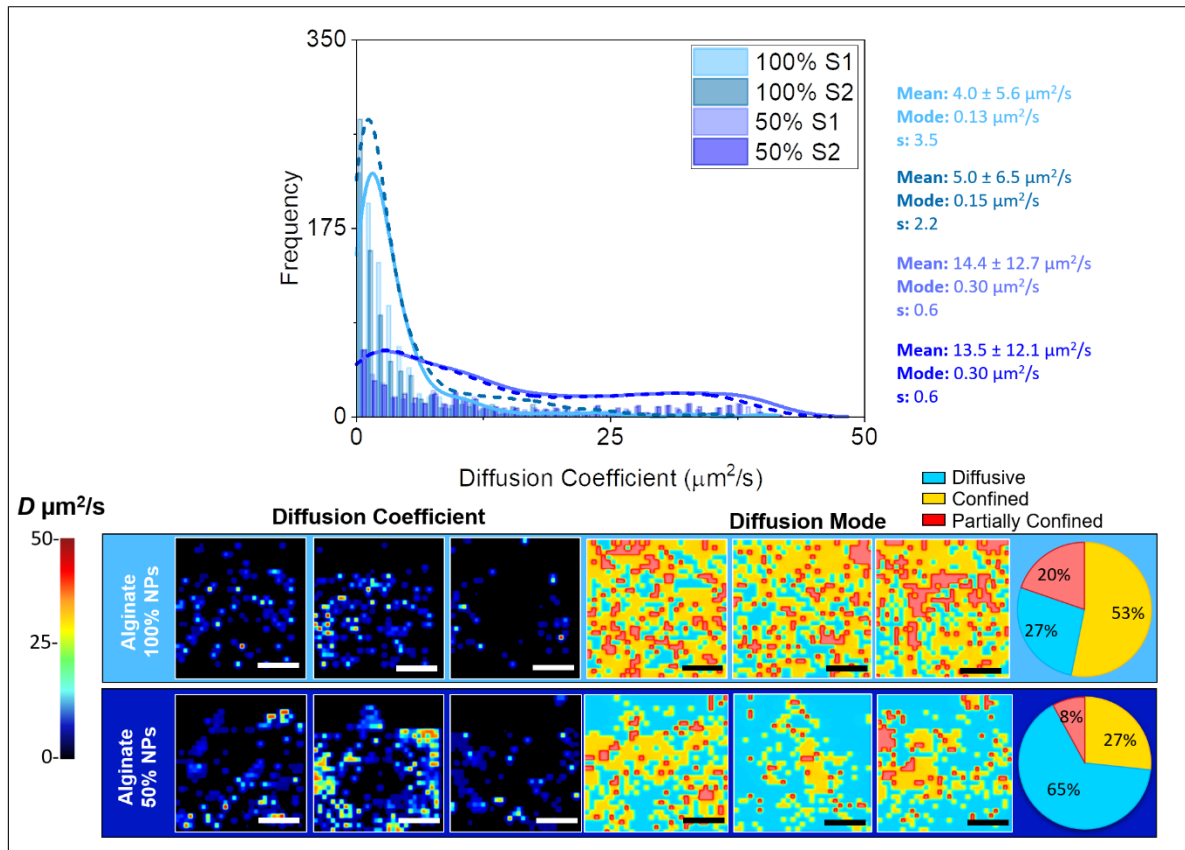


Figure 3.8: Visual maps and diffusion coefficient histograms obtained from the iMSD analysis for two NP concentration samples. The bars are histograms with a bin sizes of $1 \mu\text{m}^2/\text{s}$. The lines are kernel (Scott) probability density estimates of the diffusion coefficient (D) distributions. The color-coded values in the distribution graphs are mean, mode and skewness (s) values of the D distributions taking into consideration all 3 fields of view analyzed. The maps show the distribution of the diffusion coefficients and the modes of diffusion, freely diffusive (blue), confined (yellow) and partially confined (red). The pie charts represent the average percentage (of the three field of views analyzed) of free diffusion (blue), confined (yellow) or partially confined (red) areas. The scale bar (white and black) in each map is $5 \mu\text{m}$.

For the 100 nm particles, the average D decreased in the cross-linked alginate (from $D = 4.4 \pm 8.4 \mu\text{m}^2/\text{s}$ to $D = 2.7 \pm 5.9 \mu\text{m}^2/\text{s}$) and the distribution is more skewed towards higher values possibly due to the decrease in the pore size due to cross-linking as shown in Figure 3.7. The D of the 200 nm particle was the same for both alginate conditions,

indicating that the cross-linking did not have a significant effect on the motion, although the distribution in the cross-linked alginate is skewed towards higher values of D than the distribution for non-cross-linked alginate.

Peulen and Wilkinson previously used fluorescence correlation spectroscopy (FCS) to monitor diffusion in bacterial biofilms (Peulen & Wilkinson, 2011). Both this study and the FCS-based study observed the same trend: a marked decrease in diffusion coefficient as a function of NP size. However, with the exception of the larger particles (92 and 135 nm microspheres), the FCS-derived D distributions were relatively narrow and the average D values appeared to be insensitive to sample heterogeneities. Our results, even for the 20 nm NPs, more closely resemble the FCS results for the larger particles. This difference in D distributions and heterogeneity could arise from differences between 1) the model alginate matrix used here, and bacterial biofilm used by Peulen and Wilkinson and 2) FCS and image correlation spectroscopy (ICS, used in this study). ICS tracks fluorescence fluctuations both spatially and temporally, while FCS solely monitors fluorescence fluctuations in a small volume over time and is known to be sensitive only to mobile particles. Future studies could consider using both ICS and FCS as complementary techniques to overcome their inherent challenges.

3.3.4 Diffusion behaviors of nanoparticles in an alginate matrix

NP diffusivity in the alginate matrices has high spatial variability, as observed in the broad distributions of the diffusion coefficient and the connectivity maps (Figures 3.5 and 3.7). However, there are still size-specific trends. It is generally assumed that NPs freely diffuse within biofilms but NPs can also be confined by the biofilm matrix or confined

for a period of time before resuming free-diffusion (partially confined) (Davey, Digman, Gratton, & Moens, 2018). For the detailed description of the different modes of diffusion refer to Figure 1.6, Chapter 1. Across all NP sizes and alginate conditions, all types of diffusion were observed (Figure 3.9).

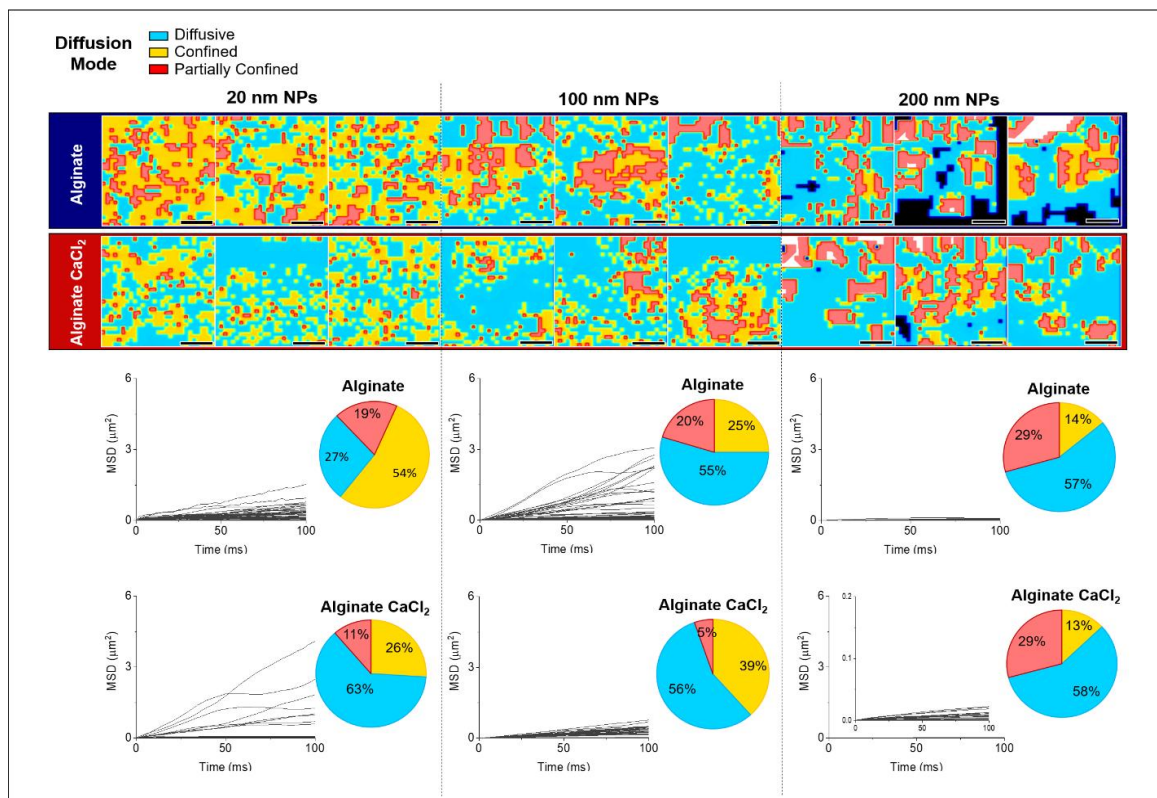


Figure 3.9: Maps of the distribution of diffusion modes, freely diffusive (blue), confined (yellow) and partially confined (red). Each row shows each field of view analyzed for each condition. The pie charts represent the average percentage (of the three fields of view analyzed) of free diffusion (blue), confined (yellow) or partially confined (red) areas. The line graphs show the mean square displacement (MSD) as a function of time obtained by SPT analysis. The inset for the 200 nm NPs shows an expanded view of the MSDs. All three fields of view were plotted in the same graph for each alginate condition and each particle size studied. The scale bar (black) in each map is 5 μm.

Zones within the alginate matrices where NPs experienced different modes seem to be smaller and more spatially distributed for the 20 nm NPs, suggesting that the diffusion

behaviors are not restricted to specific regions. The percentage of areas in which the 20 nm NPs may freely diffuse increased from an average of 27% to 63% in cross-linked alginate. As mentioned above, the increased confinement of 20 nm NPs in the alginate only matrix is likely related to the higher number of NPs per volume in the alginate network, making the free spaces of the matrix more crowded in the alginate only matrix. The percentage of areas showing free diffusion increased from 27% to 65% when the number of 20 nm particles initially added to the alginate matrix was 50% less (Figure 3.8). For the 100 nm NPs, cross-linking decreased the partially confined areas and increased the areas of confinement suggesting that for alginate networks that are around 100 nm in size, cross-linking may modify and rigidify the network making it harder for the particles to escape from confinement. Cross-linking seems to have no effect on the diffusion of 200 nm NPs. The modes of diffusion seemed to be spatially localized and, the percentage of areas with partial confinement was higher in the 200 nm samples compared to the 20 nm and 100 nm particles. The capability of a particle to escape from the confinement and start to diffuse freely will increase as the ratio of the particle diameter and the size of the area of confinement increases (Babayekhorasani, Dunstan, Krishnamoorti, & Conrad, 2016). The 200 nm NP movement could also be coupled to alginate chain relaxation. In a polymeric hydrogel like alginate both the polymer chains and the NPs are mobile (Poling-Skutvik et al., 2016). Entangled, mobile polymer chains can fluctuate and these fluctuations can facilitate the hopping of confined particles between cavities (Cai, Panyukov, & Rubinstein, 2011; Georgiades, Pudney, Thornton, & Waigh, 2013; Hansing, Duke, Fryman, Derouchey, & Netz, 2018; Sprakel, Gucht, Stuart, & Besseling, 2007). In addition, because there is no difference between the diffusion

modes of these 200 nm NPs in the alginate non-cross-linked and cross-linked matrix, it is possible that cross-linking only affected length-scales smaller than 200 nm.

Mean Square Displacement (MSD) curves for each NP size (20, 100 and 200 nm) were obtained from SPT analysis and presented in Figure 3.9 to describe the pattern of diffusion over the time observed. For the 20 nm and 100 nm particles in the alginate sample, the particles initially (< 50 ms) diffuse freely as demonstrated by the linear MSD increase with time, but the diffusion becomes anomalous for some particles after 50 ms. In a calcium cross-linked alginate matrix, the majority of the MSD curves showed a linear diffusion regime. Anomalous diffusion could be caused by a combination of inter-particle interactions due to the high number of particles (in the case of the 20 nm NPs) and heterogeneities of the alginate network. The heterogeneity of the alginate matrix (both non-cross-linked and cross-linked) showed in the broader D distributions curves and maps and in the spatial distribution of diffusion modes suggests that cavities of different sizes may be interconnected, exposing the particle to various types of void spaces that depending on their size and shape could generate deviations from the Stokes-Einstein mode of diffusion (Conrad & Poling-Skutvik, 2018; Kirstein et al., 2007). The MSD curves for the 200 nm particles have a shallower slope compared to the 20 nm and 100 nm NPs indicating that the particles are confined which is supported by the dominance of confinement in the diffusion mode maps. For all NP sizes studied, the calcium cross-linking decreased the slope of the MSD curves and the MSD versus time curves plateaued for some particles, which means that the particle was stationary for at least 0.5 s, which reinforces the connectivity maps and small D values in Figures 3.5 and 3.7, respectively.

To compare the anomalous diffusion of NPs in a heterogeneous matrix like alginate and a matrix in which the NPs should isotropically diffuse, 5 μL of NP solution (one size per sample) was added to 25 μL of an aqueous solution of 15% (v/v) of glycerol. TIRF microscopy images were collected using conditions identical to those used when imaging the 0.5% (w/v) alginate and alginate + 10 mM CaCl_2 samples. The theoretical diffusion coefficient of the 20 and 200 nm particles were calculated using the Stokes-Einstein diffusion model at a range of 15 to 25 $^\circ\text{C}$ and the viscosity of the 15% (v/v) glycerol-water mixture was calculated using the equation developed in a previous study (Cheng, 2008). The viscosity values calculated for 15 $^\circ\text{C}$ and 25 $^\circ\text{C}$ are $1.70 \times 10^{-3} \text{ Ns/m}^2$ and $1.32 \times 10^{-3} \text{ Ns/m}^2$ respectively. Using the calculated viscosity values from 15 $^\circ\text{C}$ to 25 $^\circ\text{C}$ and the measured hydrodynamic diameter of 20 nm and 200 nm particles, diffusion coefficient ranges are $D_{20\text{nm}} = 7.38 - 9.89 \mu\text{m}^2/\text{s}$ and $D_{200\text{nm}} = 1.07 - 1.42 \mu\text{m}^2/\text{s}$. The average D values obtained using iMSD were $D_{20\text{nm}} = 7.08 \pm 1.80 \mu\text{m}^2/\text{s}$ and $D_{200\text{nm}} = 0.55 \pm 0.37 \mu\text{m}^2/\text{s}$, which are close to the theoretical values calculated for both 20 nm and 200 nm particles.

The average D value for the 20 nm particles in glycerol was higher than the value obtained for the alginate for the same particle concentration but lower than that observed when the number of particles was halved (Figure 3.7 and 3.8). For the cross-linked alginate matrix the average $D_{20\text{nm}}$ was similar to that observed in glycerol. The movement of the 20 nm particles in the glycerol samples is determined by the viscosity of the solution and by interparticle interactions as indicated by the lack of physical diffusion barriers observed in the connectivity maps and is, as expected, more isotropic according to the lower anisotropy value (anisotropy = 0.20 ± 0.02) (Figure 3.10). The D

distribution of the glycerol sample shows a skewness value similar to the alginate samples. The similarity of the glycerol and matrix results suggest that for these small 20 nm diameter particles, even in the matrices with their physical barriers, solution viscosity and inter-particle interactions play dominant roles in determining the average diffusion coefficient. The role of matrix barriers in restricting the diffusion of these small particles is, however, revealed by the connectivity maps and anisotropic motion in the alginate matrices compared to glycerol.

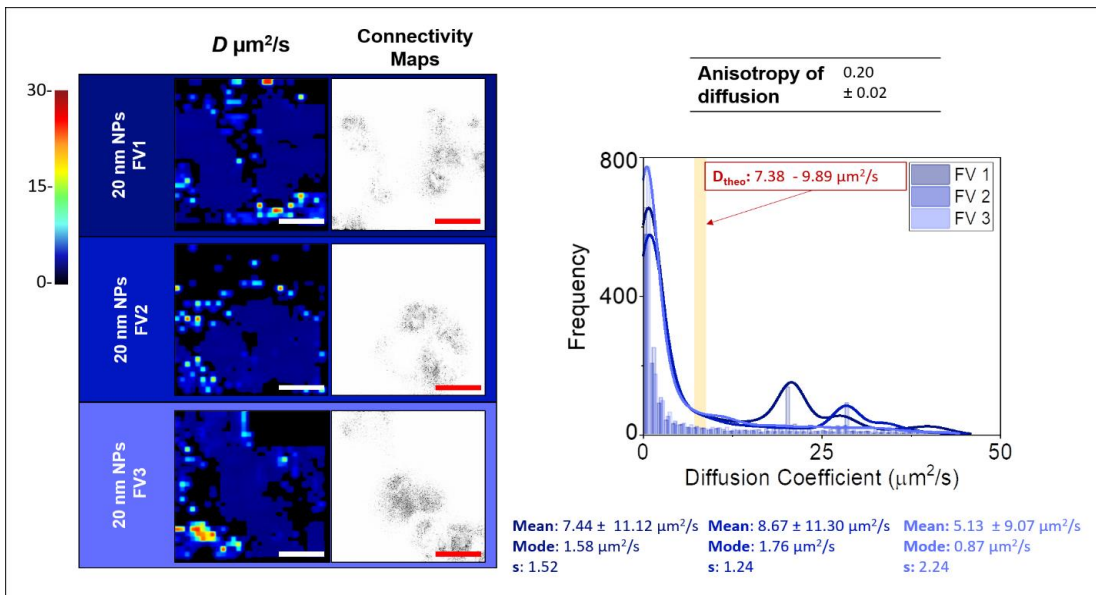


Figure 3.10: Visual maps and diffusion coefficient histograms obtained from the iMSD analysis for the 20 nm particles. The bars are histograms with a bin sizes of $1 \mu\text{m}^2/\text{s}$. The lines are kernel (Scott) probability density estimates of the diffusion coefficient (D) distributions. The connectivity maps were obtained from the 2D-pCF analysis. The D values were up to $30 \mu\text{m}^2/\text{s}$ (scale smaller than alginate samples). Each row shows each field of view analyzed for the glycerol sample. The D visual maps color scale goes from black to red, where the red areas are the areas with higher D values and the darker areas the ones with the lower the D values. The orange area in the D distribution curves represents the theoretical value calculated for a circular rigid particle of 33.6 nm following the Stokes-Einstein diffusion model in a 15% glycerol (v/v) mixture using the viscosity for a temperature range of 15-25 °C. The color-coded values in the distribution graphs are mean, mode and skewness (s) values of the D distribution. The scale bar (white and red) in each map is 5 μm .

In contrast, the much larger 200 nm particles moved faster ($D = 0.55 \pm 0.37 \mu\text{m}^2/\text{s}$) and with isotropic diffusion (anisotropy value close to 0) in the glycerol compared to both alginate samples (cross-linked and non-cross-linked) (Table 3.2, Figure 3.7 and Figure 3.11). As explained before, the 200 nm NP movement in alginate is likely limited by the size of the alginate matrix cavities (NP size and cavity size high value ratio), but also, could be coupled to alginate chain relaxation. All 200 nm NP samples (glycerol and alginate) have a positive skewness, but the glycerol distribution is significantly broader and reached higher D values compared to the alginate distributions likely due to a lack of physical barriers.

When the particles diffuse in a homogenous matrix, the D values obtained from the iMSD analysis are closer to theoretical values calculated by Stokes-Einstein equation and, unlike the results for the alginate matrices (Figure 3.5), the connectivity maps do not show barriers to diffusion.

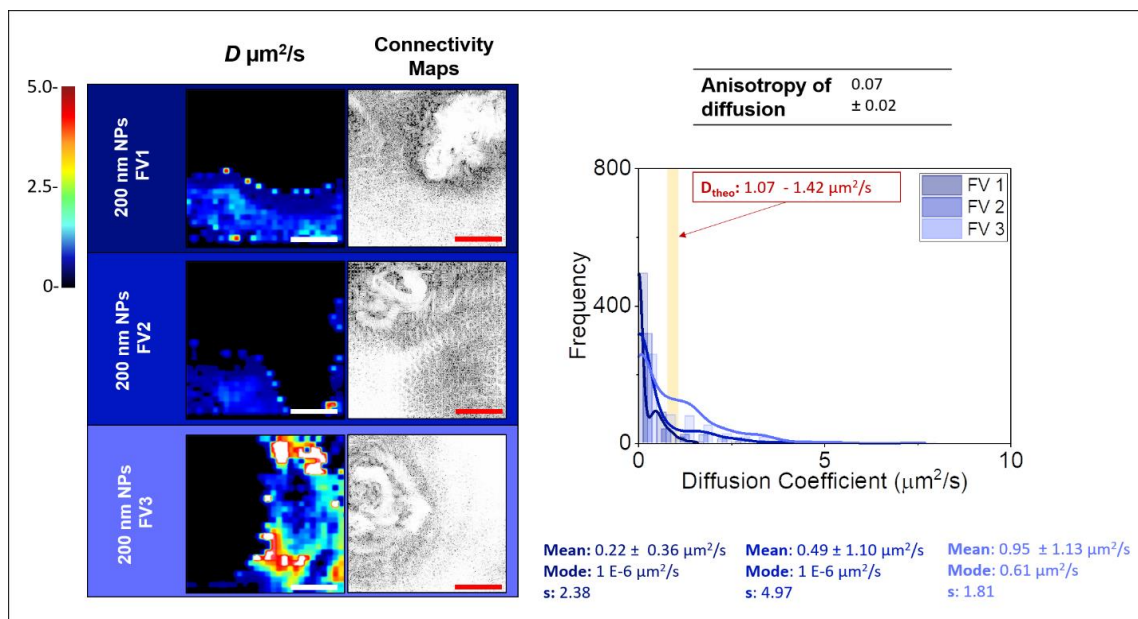


Figure 3.11: Visual maps and diffusion coefficient histograms obtained from the iMSD analysis for the 200 nm particles. The bars are histograms with a bin sizes of $0.5 \mu\text{m}^2/\text{s}$. The lines are kernel (Scott) probability density estimates of the diffusion coefficient (D) distributions. The connectivity maps were obtained from the 2D-pCF analysis. The D values were up to $5 \mu\text{m}^2/\text{s}$ (scale smaller than alginate samples). Each row shows each field of view analyzed for the glycerol sample. The D visual maps color scale goes from black to red, where the red areas are the areas with higher D values and the darker areas the ones with the lower the D values. The orange area in the D distribution curves represents the theoretical values calculated for a circular rigid particle of 232.4 nm following the Stokes-Einstein diffusion model in a 15% glycerol (v/v) mixture using the viscosity for a temperature range of 15-25 °C. The color-coded values in the distribution graphs are mean, mode and skewness (s) values of the D distribution. The scale bar (white and red) in each map is $5 \mu\text{m}$.

3.3.5 Reproducibility

TIRF microscopy images were collected for two independent alginate samples and analyzed to evaluate the reproducibility of the obtained results. Although the general trends discussed above from sample 1 are similar to the ones observed in sample 2, the average diffusion coefficient was higher in sample 2. This result suggests that even when alginate samples are prepared following the same procedure and the microscopy images

are taken in the same conditions, there is a variability between two different alginate samples characteristic of the heterogeneous nature of the matrix. The results presented in Figures 3.12, 3.13, 3.14 and 3.15 and Table 3.3, are the 2D-pCF, SPT and iMSD, analyses of sample 2 which correspond to Figures 3.5, 3.6, 3.7 and 3.9 and Table 3.2 respectively, for sample 1 presented before.

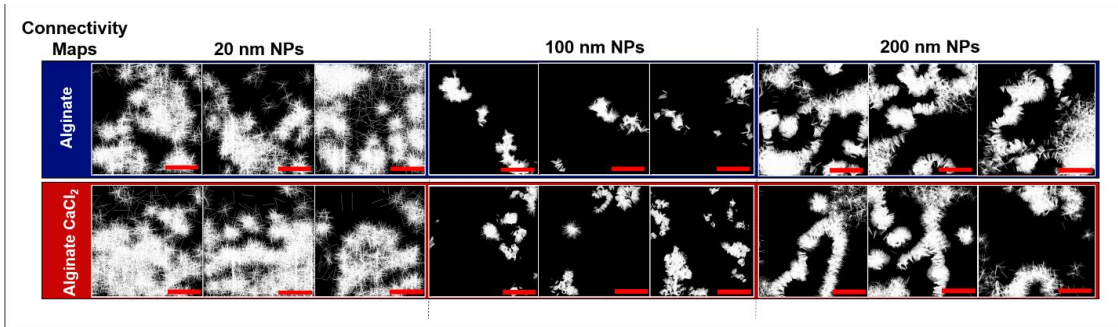


Figure 3.12: Connectivity maps for all three fields of view ($15.4 \times 15.4 \mu\text{m}$) obtained from the 2D-pCF for the 20, 100 and 200 nm NPs detected in the TIRF evanescent field. Each row shows each field of view analyzed for an alginate and a cross-linked alginate matrix. The scale bar (red) in each map is of $5 \mu\text{m}$.

Table 3.3: The averaged anisotropy values obtained from the 2D-pCF analysis for each nanoparticle size considered in this study in sample 2.

20 nm NPs		100 nm NPs		200 nm NPs	
Alginate	Alginate CaCl ₂	Alginate	Alginate CaCl ₂	Alginate	Alginate CaCl ₂
0.54 ± 0.06	0.58 ± 0.04	0.43 ± 0.17	0.49 ± 0.08	0.38 ± 0.11	0.43 ± 0.04

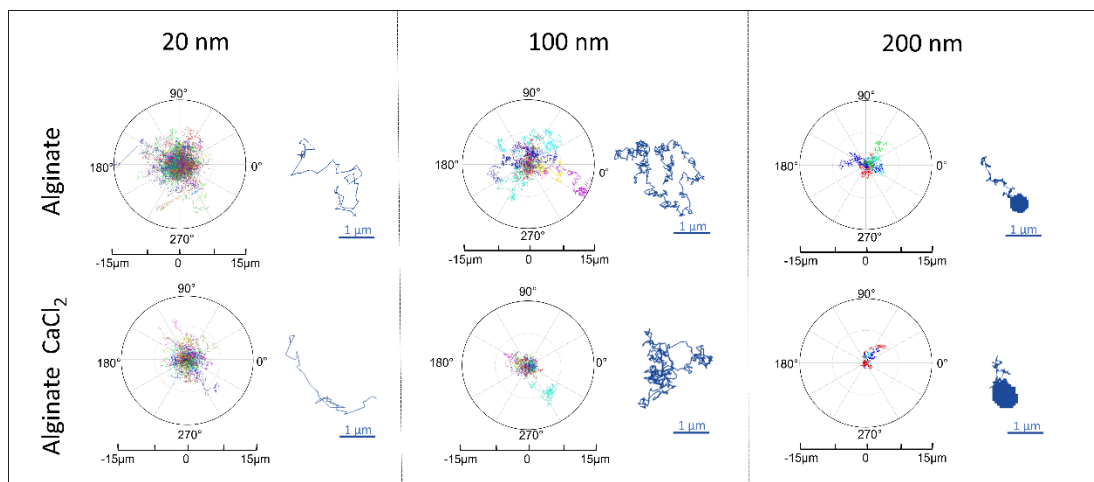


Figure 3.13: Average anisotropy values (from 2D-pCF analysis) and polar graphs of individual tracks from the SPT of all 3 fields of views analyzed of 20, 100 and 200 nm NPs through an alginate and a cross-linked alginate matrix. Each track has an assigned color that represents a single particle with the origin representing the initial position. All the particle tracks for the three field of views are presented in the polar graph for each alginate matrix condition and particle size. The cross-linking did not have a statistically significant effect in the anisotropy values (p-value $_{20\text{nm}} = 0.41$, p-value $_{100\text{nm}} = 0.06$ and p-value $_{200\text{nm}} = 0.54$).

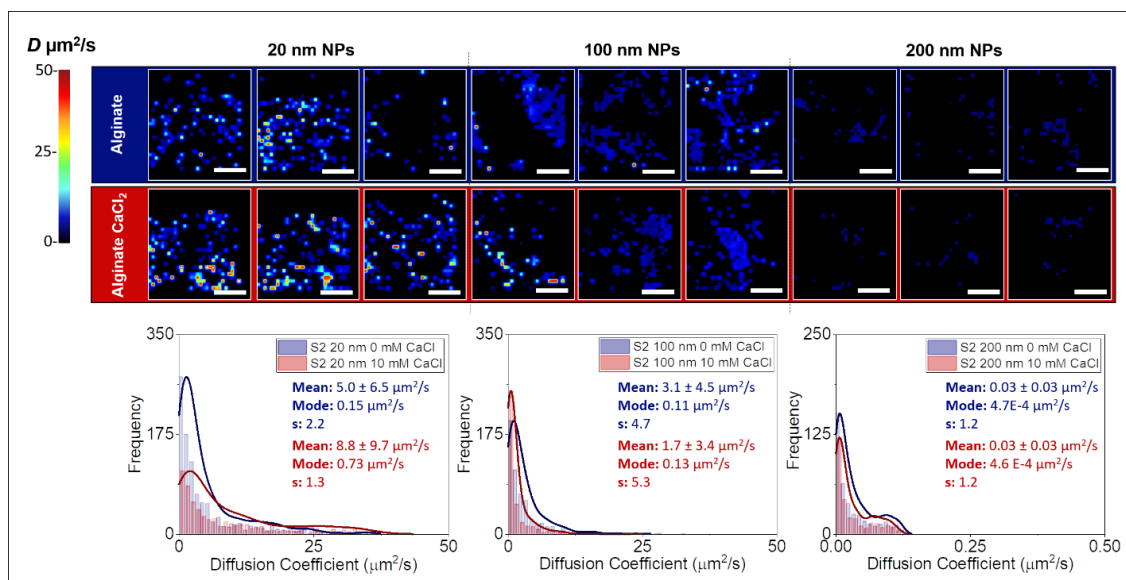


Figure 3.14: Visual maps and diffusion coefficient histograms for each NP size studied obtained from the iMSD analysis. The bars are histograms with bins sizes of $1 \mu\text{m}^2/\text{s}$ for the 20 and 100 nm NPs and $0.01 \mu\text{m}^2/\text{s}$ for the 200 nm NPs. The lines are kernel (Scott) probability density estimates of the diffusion coefficient (D) distributions. The D values were up to $50 \mu\text{m}^2/\text{s}$ for the 20 nm particles. Each row shows each field of view analyzed for each condition. The D maps color scale goes from black to red. The red areas are the areas with higher D values and the darker areas the ones with the lower D values. The color-coded values in the distribution graphs are mean, mode and skewness (s) values of the D distributions taking into consideration all 3 fields of views analyzed. The scale bar (white) in each map is $5 \mu\text{m}$.

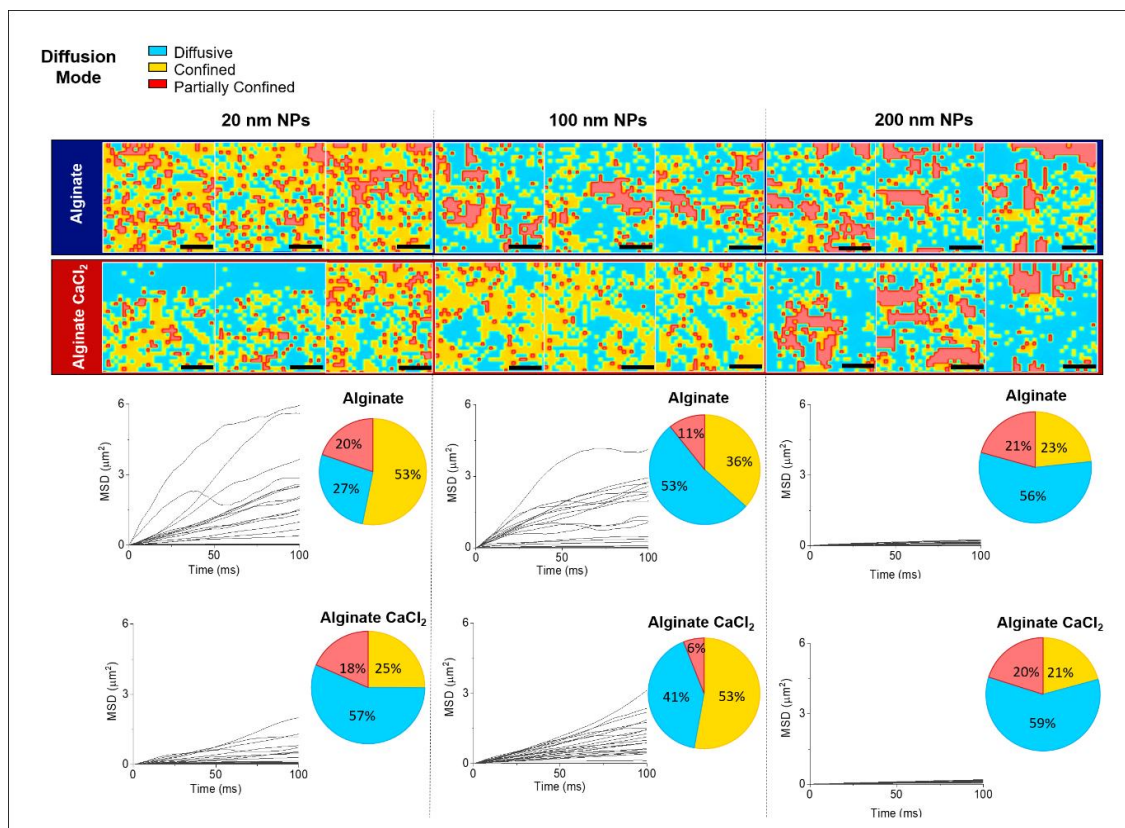


Figure 3.15: Maps of the distribution of diffusion modes, freely diffusive (blue), confined (yellow) and partially confined (red). Each row shows each field of view analyzed for each condition. The pie charts represent the average percentage (of the three field of views analyzed) of free diffusion (blue), confined (yellow) or partially confined (red) areas for each NP size. The graphs show the Mean Square Displacement (MSD) in time obtained from the SPT analysis. All three fields of view were plotted in the same graph for each alginate condition and each particle size studied. The scale bar (black) in each map is 5 μm .

3.4 Conclusion

The fate and transport of NPs in the environment is hard to predict due to the highly variable environmental conditions and the long list of unique properties and composition that NPs can exhibit. To predict NP environmental fate and toxicity risk, and to optimize NP design for specific applications, the conditions that could potentially affect NPs transport have to be identified. The key criteria for designing NPs that effectively

accumulate and penetrate biofilms have been NP size and surface characteristics (Miller et al., 2015). However, this study highlights the importance of the matrix properties to which the NPs are targeted in evaluating and predicting NP transport.

The findings from this study indicate that cross-linking can lead to structural changes that can restrict and alter the diffusive behavior of NPs in heterogeneous matrices like alginate, but the significance of the cross-linking effect on NP diffusion will depend on NP size. In this study we found that, as expected the average diffusion coefficient increased as the NP size decreased. However, a simple inverse trend between NP size and diffusion coefficient cannot be inferred. For NPs below a matrix dependent size limit, NP concentration influences the diffusion, likely due to higher particle penetration of the matrix leading to particle crowding and inter-particle repulsive interactions. The differences in D values and areas of diffusion observed in the connectivity maps between the homogenous matrix and the alginate ones confirm that physical barriers that are formed in polysaccharides matrices will restrict the diffusion of NPs in biofilms. The scale of the accessible area for diffusion relative to the NP size is important and could influence modes of diffusion. All sizes of particles under study experienced a degree of confinement and partial confinement. Therefore, diffusion in heterogeneous matrices (like alginate) cannot be assumed to be isotropic. Different modes of diffusion should be taken into consideration in biofilm modeling.

The spatial variability of NP diffusive behaviors and diffusion coefficients was clearly observed in this study. The combination of iMSD, 2D-pCF, and SPT, which are microscopy advances previously used in cell systems (Di Rienzo et al., 2013; Digiacomio

et al., 2016; Digman & Gratton, 2009; Malacrida, Hedde, et al., 2018; Malacrida, Rao, et al., 2018) to quantitate heterogeneous diffusion, could formulate a better understanding of heterogeneous diffusion-controlled systems. In the case of biofilm systems, these methods could lead to a better understanding of the natural spatial heterogeneity of the EPS, how local structural micro-domains affect the mobility of NPs in biofilms and can provide experimental data to develop mathematical biofilms models that consider the variable diffusivity modes of solutes within biofilms.

CHAPTER 4

THE EFFECTS OF POLYSTYRENE NANOPARTICLES ON THE GENETIC EXPRESSION OF KEY EPS PRODUCTION AND QUORUM SENSING SYSTEMS AS A FUNCTION OF PARTICLE CHARGE AND BIOFILM AGE

4.1 Introduction

The exposure of biofilms to nanoparticles (NPs) can have important consequences for microbial behavior and viability. The cellular responses and effects depend on the metabolic capabilities and cell membrane properties of the microbe but also on the physical and chemical properties of the NPs (Chompoosor et al., 2010; Li, Zhang, Niu, & Chen, 2013). For example, inorganic nanoparticles (e.g. titanium dioxide, silver, cadmium oxide and zero valent iron) can generate reactive oxygen species (ROS) that can activate death signaling pathways, survival signaling mechanisms, and affect gene expression (Erdim, Badireddy, & Wiesner, 2015; Hessler, Wu, Xue, Choi, & Seo, 2012; Patil & Parikh, 2014; Sevcu, El Temsah, Joner, & Cernik, 2011; Shivashankarappa, 2015; von Moos & Slaveykova, 2014).

Nanoparticles can also affect cell-cell communication by altering the expression of quorum-sensing systems that are vital for biofilm formation and maturation. The quorum-sensing (QS) systems works through a receptor in the membrane that binds the extracellular signal and then interacts with a response regulator to modify transcriptional levels and regulate cooperative behaviors (Mellbye & Schuster, 2014). QS signaling networks can regulate the extracellular polymeric substances (EPS) secreted by the

bacterial cells as a response to environmental stimuli (Kassinger & Hoek, 2020). As mentioned before in Chapter 1, the biofilm structure is highly dictated by the EPS, so changes in EPS composition could affect the matrix mechanical properties due to changes in the degree of cross-linking (DCL) between EPS components (Chapter 2). Changes in the DCL of the EPS matrix can affect biofilm architecture and the biofilm's metabolic efficiency (Kassinger & Hoek, 2020; Matsukawa & Greenberg, 2004; Wang et al., 2016).

4.1.2 Specific Objectives

Biofilms are dynamic and active with responsive interchange between the microbial inhabitants and the biofilm structure. Our hypothesis is that when NPs accumulate in biofilms, NPs could be a stressor for the cells and cause changes (increases or decreases) in the genetic expression of key EPS production and quorum-sensing systems. If NPs are stressors for the bacteria and lead to changes in the production of EPS components and quorum sensing signals, the EPS matrix composition can change resulting in a change in biofilm properties.

The specific objective of this study was to evaluate how *Pseudomonas aeruginosa* biofilms respond to the presence of cationic and anionic polystyrene NPs. Specifically, (1) identify changes in the expression of genes related to polysaccharides biosynthesis (*pelA*) and quorum sensing systems (*lasR* and *rhlR*), (2) quantify changes in the extracellular DNA concentration and, (3) assess the role of biofilm age in the magnitude of the cellular response to cationic and anionic polystyrene NP exposure.

4.2 Materials and Methods

4.2.1 Preparation of *Pseudomonas aeruginosa* inoculum

For this experiment, we used the bacteria *Pseudomonas aeruginosa*, strain PAO1 $\Delta wspF \Delta psl P_{BADpel}$. *Pseudomonas aeruginosa* is a well-known biofilm former and this strain has been previously described by Jennings et al., (2015) as having an arabinose-inducible *pel* operon, *wspF* non-polar mutation, *pslBCD* and polar mutant of the *psl* operon. The PAO1 $\Delta wspF \Delta psl P_{BADpel}$ strain have only the polysaccharide *Pel* as the primary matrix structural polysaccharide, making it suitable to study the effect of the NPs presence on polysaccharides production. The bacteria were first cultivated on agar plates containing Jensen's chemically - defined medium. The agar media plates were prepared by mixing NaCl (85.6 mM), K₂HPO₄ (14.4 mM), sodium glutamate (92 mM), valine (24 mM), phenylalanine (8 mM), Bacto agar (15 g/L) and adjusting the pH to 7.3 using HCl before autoclaving the solution. After the autoclave cycle, the media was, then, supplemented with filtered (0.20 μ m syringe filter) glucose (final concentration of 70 mM), 0.5% (vol/vol) arabinose and trace minerals. The trace minerals added were CaCl₂ (0.14 mM), MgSO₄ (1.33 mM), FeSO₄ (0.0039 mM), and ZnSO₄ (0.0085 mM). After growing the bacteria in the agar plate, a single colony was picked and suspended in liquid Jensen's media in a sterile 150 mL Erlenmeyer flask covered with cotton to promote aeration in aseptic conditions. The culture was incubated overnight at 37° C with slow mixing and then diluted to an optical density OD₆₀₀ of 0.05. All handling of samples containing PAO1 $\Delta wspF \Delta psl P_{BADpel}$ cells were done in aseptic conditions to avoid contamination of the pure culture and inside a biosafety cabinet as a safety precaution.

4.2.2 Biofilm growth in flow cell chambers with continuous media flow

4.2.2.1 Flow cell design and experimental setup

In order to observe the samples under the microscope without disturbing the biofilm structure the flow cell chambers were custom designed and 3D printed. Figure 4.1 shows a picture of the assembled flow cell and a diagram with the specific dimensions of the design can be found in Appendix B.

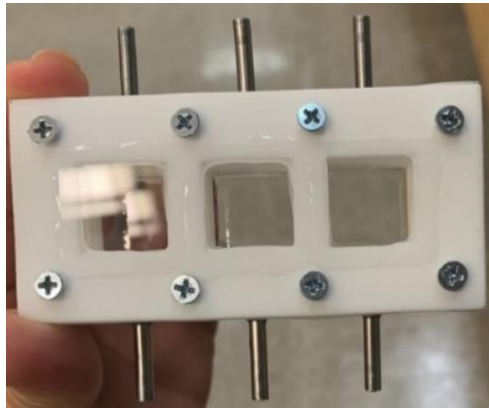


Figure 4.1: Custom designed flow cells. Each flow cell has 3 chambers for sample replicates and are sealed with glass coverslips to allow the in-situ visualization of the sample under the microscope.

The flow cell body was made of the polymer PA 2200, the external side stainless-steel tubes, designed for media flow, have a diameter of 3 mm and the screws to attach the top part to the bottom are 3/8 inches aluminum pan head Phillips style #4. The flow cell chambers were closed with glass cover slips of 0.17 mm thickness with dimensions of 22 mm x 22 mm (Millipore Sigma, C9802). To prevent media leaks and the contamination of the pure culture inside the flow cell chambers, a silicon sheet was placed in between the top and bottom parts of the flow cell body (without obstructing the wells) and the

flow cells were sealed with a clear waterproof silicone sealant. For media flow, translucent silicone tubes (OD= 5 mm, ID= 3mm) were connected to the stainless-steel side tubes of the flow cell and a peristaltic pump was used to provide a continuous media flow of 30 mL/hr through the chambers. Each flow cell was connected to a 2 L media bottle (with continuous mixing) to supply fresh media to all the chambers of the flow cell (3 chambers/ flow cell) and the outflow of each chamber was collected in a 10 L media bottle and treated as a biowaste. Figure 4.2 shows a picture of the experimental setup in the 37°C controlled temperature room.



Figure 4.2: Experimental setup to cultivate biofilms with continuous flow in custom designed flow cells.

The flow cell chambers were inoculated with a diluted fresh overnight culture of the PAO1 $\Delta_{wspF} \Delta_{psl} P_{BAD}pel$. The biofilms were cultivated in Jensen's minimal glucose media containing NaCl (85.6 mM), K_2HPO_4 (14.4 mM), ammonium sulfate (15.1 mM), glucose (0.3 mM), 0.5% (vol/vol) arabinose, $MgSO_4$ (1.33 mM), $CaCl_2$ (0.14 mM),

FeSO₄ (0.0039 mM) and ZnSO₄ (0.0085 mM) to promote biofilm formation (Jennings et al., 2015). To inoculate the flow cell chambers, 5 mL of the diluted bacterial inoculum was added to each flow cell chamber using a sterile syringe. Cells were allowed to attach to the glass coverslip substratum for 3 hours before starting the media flow. Previous studies have identified significant biofilm development at 48 hr of cultivation, for that reason, biofilms were grown for 48 and 96 hours in the controlled temperature room at 37°C and with a constant flow of fresh media (Allesen-Holm et al., 2006; Colvin et al., 2011; Jennings et al., 2015).

4.2.2.2 Biofilm treatment with cationic and anionic nanoparticles

To evaluate if NP accumulation in the biofilms stressed the bacteria and affected gene expression of key EPS production and quorum sensing systems, we exposed the biofilms cultivated in the flow cells to cationic and anionic nanoparticles.

Biofilms were cultivated for 48 and 96 hours in 3 flow cells for a total of 9 chambers with biofilm replicates. Two of the flow cells were treated with polystyrene NPs of 50 nm in 1 mM HEPES buffer and the other one was treated with just 1 mM HEPES buffer as a control (Figure 4.3).

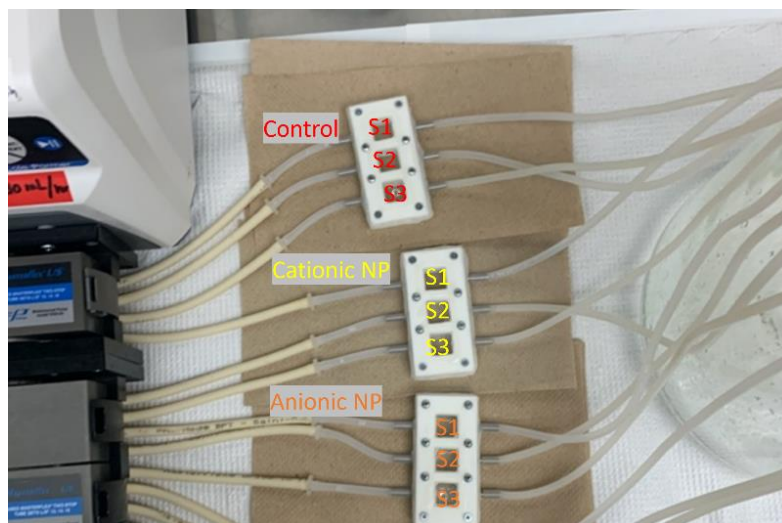


Figure 4.3: Diagram showing the flow cells exposed to NPs. The flow cell “Control” was treated with HEPES buffer, the “Cationic NP” with aminated polystyrene nanoparticles and the “Anionic NP” with carboxylated polystyrene nanoparticles. Each flow cell has 3 chambers allowing biological triplicates for each condition.

When the biofilms reached the desired age (48 or 96 hrs), with the help of a sterile syringe and without opening the flow cells, all nine chambers were washed with 5 mL of 1 mM HEPES buffer (pH 7.14) to wash out the suspended biomass. This washing step was intended to remove also all the liquid media in the chamber that could cause the NPs to aggregate. After the washing step, 5 mL of 1 mM HEPES buffer was added to each chamber of the “Control” flow cell. In the “Cationic NP” flow cell, a 5 mL of solution of positively charged fluorescent aminated polystyrene beads (Invitrogen FluoSpheres, max abs/em: 580/605 and $d = 64 \pm 3.4$ nm) was added while in “Anionic NP” flow cell, a 5 mL solution of negatively charged fluorescent carboxylated polystyrene beads (Invitrogen FluoSpheres, max abs/em: 580/605 and $d = 63 \pm 3.1$ nm) was used. The NPs were suspended in 1 mM HEPES buffer (pH 7.14) at a concentration of 100 mg/L. The results from the “Control” flow cell samples represented the normal expression of the

targeted genes when PAO1 $\Delta wspF \Delta psl P_{BADpel}$ grew under the specified conditions. After 6 hours of exposure to the NPs under static conditions, the flow cells were opened, and samples were collected for further extractions. Each experiment was repeated twice for each biofilm age.

4.2.3 Extracellular DNA and RNA extraction

After the biofilm samples were collected, the samples were centrifuged in order to separate the bacterial cells from the loosely bound extracellular polymeric substances (EPS). The supernatant part of the sample was used to extract and quantify the production of extracellular DNA release from the biofilm, and the cell pellet was used for RNA extraction from the bacteria cells. The RNA extraction procedure was performed immediately after sample collection using the QIAamp Viral RNA extraction kit from QIAGEN following the manufacturer recommended protocol (note that despite its name, this kit includes directions for isolating RNA from cell cultures). Briefly, each sample was first treated with DNase I to remove any contaminating genomic DNA and then the buffer AVL containing the RNA carrier, which increases binding of the bacterial RNA to the membrane and provides decoy RNA for any remaining active RNases, and the cell pellet were mixed and incubated for 10 min at room temperature for cell lysis. After centrifugation, ethanol (96 -100%) was added to increase the efficiency of the RNA isolation. Then, the lysate was added to the QIAamp Mini column and rinsed with the AW1 and AW2 buffers. Using buffer AVE the extracted RNA was eluted from the QIAamp Mini column. The RNA concentration was measured using the Qubit RNA HS Assay kit from Invitrogen with the Qubit Fluorometer. The messenger RNA (mRNA)

was then converted to single stranded complementary DNA (cDNA) suitable for the quantitative polymeric chain reaction (qPCR) with the enzyme reverse transcriptase using the High-Capacity cDNA Reverse Transcription Kit from Applied Biosystems. To synthesize cDNA from the RNA, we followed the protocol recommended by the manufacturer. In brief, the reverse transcription master mix was prepared by adding the recommended amounts of 10X RT buffer, 25X dNTP mix, 10X RT random primers, the MultiScribe reverse transcriptase and the necessary nuclease-free water for a total reaction volume of 10 μ L. In a 600 μ L microtube, the master mix was mixed with 10 μ L of the RNA sample and the reverse transcription reaction was performed in a thermal cycler following 3 steps, 25° C for 10 min, 37° C for 120 min and ending with 5 min at 85° C. The resulting cDNA concentration was quantified using the Qubit dsDNA HS Assay kit from Invitrogen with the Qubit Fluorometer and stored at -20° C for further qPCR experiments.

Extracellular DNA (eDNA) was extracted from the supernatant portion of the biofilm samples to avoid contamination with genomic DNA from inside the cells using the DNeasy® PowerSoil Pro Kit from QIAGEN following the manufacturer protocol. Briefly, solution CD1 was added to a PowerBead Pro Tube with 400 μ L of the sample, which was mixed using a vortexer and then centrifuged. This step is intended for cell lysis but even though there were no cells in the sample, we decided to include this step to avoid changes in the protocol and for sample homogenization. The supernatant was transferred to a new vial and solution CD2 was added to precipitate non-DNA material on the sample. The supernatant was then transferred to a new vial and the high salt solution CD3 was added. All of the sample was loaded into an MB Spin Column in which the

DNA was bound to the silica membrane. Using solution EA (wash buffer) and solution C5 (ethanol-based wash solution) the DNA retained on the column was washed and then eluted with solution C6 (10 mM Tris). The extracted eDNA was quantified using the Qubit dsDNA HS Assay kit. We used as a reference the eDNA concentration from the “Control” sample to determine if there was an increase or decrease in eDNA secretion due to the NPs presence.

4.2.4 Real-time quantitative PCR experiment

The effects of cationic and anionic polystyrene NPs on the expression of genes related to polysaccharide production and quorum sensing systems was assessed through qPCR experiments performed for both biofilm ages (48 and 96 hours). The expression of genes related to polysaccharide production was assessed using primers for the *pelA* gene (Colvin et al., 2011). PAO1 $\Delta wspF \Delta psl P_{BAD}pel$ is a strain with the arabinose-inducible *pel* operon, meaning that one of its principal polysaccharides is *Pel*, a cationic polysaccharide that can cross-link with eDNA (Jennings et al., 2015). To evaluate the effect of the NP’s presence on the expression of genes related to the quorum sensing system, we used specific primers for the *lasR* and *rhlR* genes (Colvin et al., 2011; Mellbye & Schuster, 2014). *LasR* and *rhlR* are the most well-known quorum sensing systems of *P. aeruginosa* that controls virulence factor production, swarming motility and biofilm development and maturation (Mellbye & Schuster, 2014). The genes *ampR* (ampicillin resistant gene) and *rpsL* (encodes the ribosomal S12 protein) were used as the reference transcripts (Colvin et al., 2011, 2012a). Table 4.1 summarizes the forward and reverse sequences of all the primers used.

Table 4.1: Primer sequences used in qPCR experiment.

gene	Forward (5' → 3')	Reverse (3' → 5')	Reference
<i>pelA</i>	CCTTCAGCCATCCGTTCTTCT	TCGCGTACGAAGTCGACCTT	(Colvin et al., 2011)
<i>ampR</i>	GCGCCATCCCTTCATCG	GATGTGACGCGGTTGTTG	
<i>rhlR</i>	ACCGCGAGATCCTGCAATG	TCAGGATGATGGCGATTTC	(Mellbye & Schuster, 2014)
<i>lasR</i>	TTTCTGGGAACCGTCCATCT	GCCGAGGCTTCCTCGAA	(Colvin et al., 2012a)
<i>rpsL</i>	GCTGTGCTCTTGACAGGTTGTG	GCAAACATCAACCAGCTGGTG	

Amplification of the cDNA templates was done with a StepOne Real Time PCR System from Applied Biosystems using iTaq Universal SYBR Green Supermix from BIORAD for dye-based detection. For each PCR reaction, 2 µL of cDNA template, 10 µL of 2X master mix, 1.8 µL of the reverse and forward primer (final concentration 450 nM) and 6.2 µL of RNase free water for a total reaction volume of 20 µL was used.

The real-time PCR conditions for the amplification of 16SrDNA gene was 600 s at 95 °C followed by 40 cycles: 15 s at 95 °C for denaturation, 60 s at 60 °C for annealing. One last step from 60 to 95 °C with an increase of 0.3 °C/s was added to obtain a melt curve.

The qPCR reaction conditions were an initial activation cycle of 600 s at 95 °C, followed by 35 cycles of 10 s at 95 °C for denaturation and 60 s at a specific temperature for annealing/extension for each gene. The annealing/extension temperatures were 60.5°C for *rhlR* and 60.0°C for *pelA*, *lasR*, *ampR* and *rpsL*. A melt curve analysis was performed using the temperature range of 60 °C to 95 °C at 0.3 °C/s intervals to verify the specific amplification of a single PCR product. Each plate run for each gene target included triplicates of non-template control (well without the cDNA template), 3 biological replicates with two technical replicates for each condition (control biofilm, aminated NP treated biofilm and carboxylated NP treated biofilm) and standard samples to generate

standard curves for the PCR efficiency estimation. Different genes were analyzed in different runs.

4.2.4.1 qPCR data analysis

The qPCR data was analyzed using relative quantification as explained in detail by Taylor et al., (2019). The gene of interest (*pelA*, *lasR*, *rhlR* and *rpsL*) was compared to the reference gene (*ampR*) to normalize the changes for each sample using the reaction efficiencies for each run calculated from the standard curves (for each gene, target and reference) using the following equation:

$$Efficiency = 10^{\left(-\frac{1}{slope}\right)} - 1 \quad (13)$$

Using the mean quantitative cycle (C_q) of the technical replicates for each biological replicate of the control sample and the NP treated sample the normalized fold expression of target genes was calculated using the following equation:

$$Normalized\ fold\ expression = \log_2 \left(\frac{(E_{target})^{\Delta C_{q_{target}}}}{(E_{ref})^{\Delta C_{q_{ref}}}} \right) \quad (14)$$

This equation considers the efficiency for the reference gene (E_{ref}) and the efficiency for the gene target (E_{target}).

4.2.5 Protein quantification

The total protein concentration in each sample fraction (unbound proteins from the sample supernatant and bound and intracellular proteins from the cell pellet) were

measured using the Qubit Protein Assay Kit with the Qubit Fluorometer using bovine serum albumin (BSA) as the standard.

4.2.6 Statistical analysis

For statistical comparisons of between the control and the NP treated samples in terms of the extracellular DNA concentration, the normalized fold expression of the *pelA*, *lasR*, *rhlR* and *rpsL* genes and the total protein concentration, a Two-Sample T-test was run in Minitab 19 using the average value and standard deviation of all three biological replicates from the two independent experiments.

4.3 Results and Discussion

4.3.1 Polystyrene nanoparticles are effective in downregulating *pelA*

We explored the impact of 50 nm cationic and anionic polystyrene nanoparticles (NPs) on the expression of *pelA* transcripts using qPCR. Figure 4.4 shows the normalized fold expression of *pelA* for each condition. *P. aeruginosa* strains have a highly conserved seven gene cluster that encodes proteins involved in exopolysaccharide *Pel* biosynthesis (Colvin et al., 2012b). *Pel* is a cationic exopolysaccharide that provides the primary structural scaffold for *P. aeruginosa* biofilms specially for the surface-attached submerged biofilms cultivated in flow cells and is important for initiating and maintaining cell to cell interactions for cell attachment to the surface (Colvin et al., 2011; Friedman & Kolter, 2004; Jennings et al., 2015). One of the hypotheses of this study is that NPs could be a stressor for the bacteria and lead to an increase in the production of polysaccharides. An increase in polysaccharide concentration could increase the degree

of cross-linking (DCL) (see Chapter 2) between EPS components which may restrict diffusion processes in the matrix. In the younger biofilms (48 hrs) samples, no statistically significant changes were identified between the unexposed biofilms (Control) and the NP treated biofilm samples (COOH⁻ and NH₃⁺). However, in the older biofilms (96 hrs), the *pelA* transcripts produced by untreated biofilms were significantly higher than the NP treated samples (p-value NH₃⁺ = 0.03 and p-value COOH⁻ = 0.04). These results suggest that aminated and carboxylated polystyrene nanoparticles are effective in down-regulating *pelA* independent of particle surface functionalization. It has been proposed that *Pel A* is a protein located in the periplasm related polymer (*Pel*) chain length regulation but it is not clear if a decrease in the expression of the *pelA* gene will lead to a decrease in the overall *Pel* production (in terms of concentration) or if only the polymer chain length will be affected (Colvin et al., 2013; Marmont et al., 2017). Further experiments can focus on evaluating the effects on the biofilm composition due to the downregulation of *pelA* by cationic and anionic NP in mature biofilms using extraction and analytical methods to quantify *Pel* (Jennings et al., 2015).

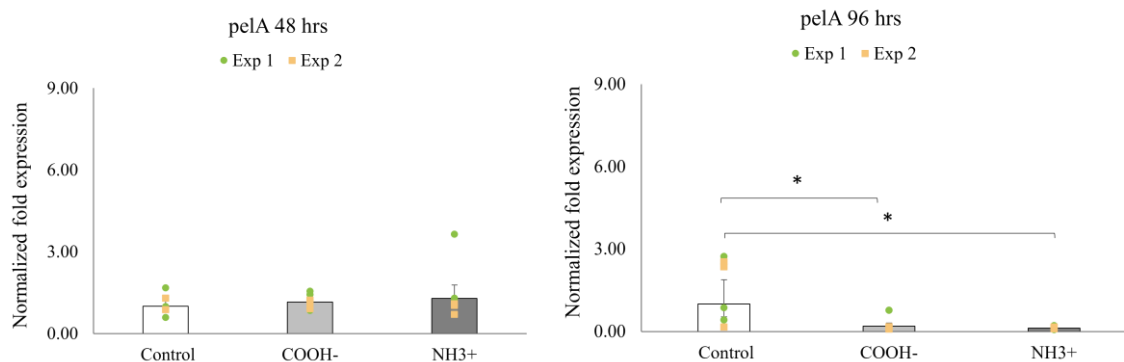


Figure 4.4: Normalized fold expression of *pelA* transcription by PAO1 $\Delta wspF \Delta psl P_{BADpel}$ bacterial strain for unexposed biofilms (Control) and NP treated biofilm samples (aminated polystyrene (NH_3^+) and carboxylated polystyrene (COOH^-)). The values correspond to two independent experiments and triplicate biological samples for each experiment for each condition (green and yellow symbols indicate the two independent experiments). The qPCR results were normalized to the results for the reference gene *ampR*. The error bars represent the standard error of the mean of 6 biological samples (3 from each experimental replicate). Asterisks indicate statistical significance, * for $p \leq 0.05$ and ** for $p \leq 0.01$.

According to the results, polystyrene NPs may not affect the initial stages of PAO1 $\Delta wspF \Delta psl P_{BADpel}$ transcription of *Pel* associated genes independent of the particle surface properties (Figure 4.4). However, cells in mature biofilms may be threatened by aminated and carboxylated modified polystyrene NPs as shown by the decrease in *pelA* transcriptomes after NP exposure. As shown in previous studies of *Pel* mutants (Friedman & Kolter, 2004), in addition to EPS biosynthesis *Pel* genes are also required for the formation of carbohydrate-containing compounds that encase the bacterial cells. A decrease in polysaccharides production due to the presence of polystyrene NPs could disrupt the carbohydrate layer encasing the bacteria resulting in an increase in susceptibility to antibiotics. In a previous study, it was found that for *P. aeruginosa* strains PAO1 and PA14 in biofilms *Pel* protects the bacteria from the antibiotic tobramycin (Colvin et al., 2011). The decrease in *pelA* transcripts after NP (aminated and

carboxylated) exposure could have implications in efforts towards biofilm control depending on the *P. aeruginosa* strain. For the case of the PAO1 strain, the reduction in *Pel* doesn't affect the growth of the biofilm but in other *P. aeruginosa* strains (e.g., PA14) the decrease in *Pel* production can prohibit the biofilms from growing larger (Colvin et al., 2011). However, further studies are needed to test these hypotheses, for example, studies to measure *Pel* production and biofilm growth (e.g., biofilm thickness and dispersion) after the NP exposure.

4.3.2 Carboxylated polystyrene nanoparticles can decrease *lasR* gene expression

In addition to the effect of aminated and carboxylated polystyrene NPs on the expression of *pelA* we evaluated their effects on the expression of *lasR* and *rhlR* genes. LasR is one of most well-known quorum-sensing systems of *P. aeruginosa* that controls virulence factor production, swarming motility, and biofilm maturation. Bacterial cell density is monitored by signaling molecules, in the case of *P. aeruginosa*, the homoserine lactones (HSLs). At a certain cell density, *lasR* responds to an increase in biomass and the cells disperse from the biofilm through the quorum-sensing influence. The results of qPCR experiments from the expression of *lasR* are presented in Figure 4.5. After the biofilm's exposure to aminated-modified polystyrene (NH₃⁺) and carboxylated-modified polystyrene (COOH⁻), only the older biofilms (96 hrs) treated with carboxylated NPs showed a significant decrease in the expression of *lasR* (p-value_{COOH} = 0.02).

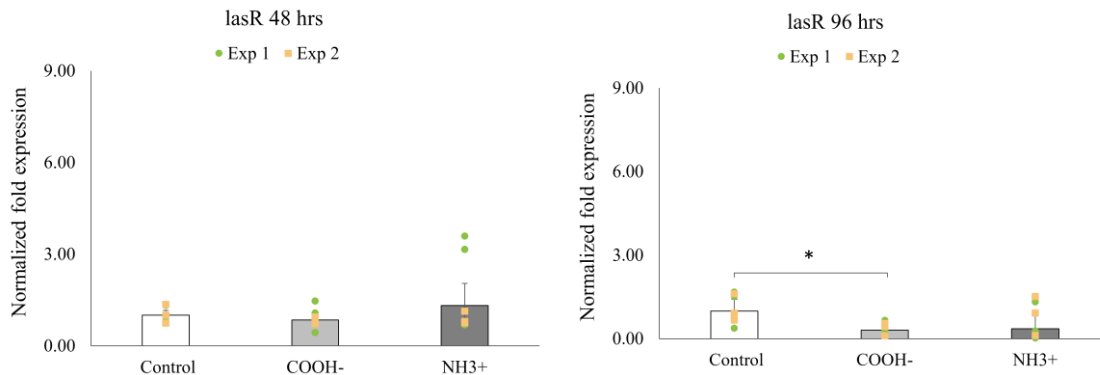


Figure 4.5: Normalized fold expression of *lasR* transcription by PAO1 $\Delta wspF \Delta psl$ P_{BADpel} bacterial strain of unexposed biofilms (Control) and NP treated biofilm samples (aminated- modified polystyrene (NH₃⁺) and carboxylated-modified polystyrene (COOH⁻)). The values correspond to triplicates of biological samples for each condition for two independent experiments normalized to the reference gene *ampR*. The error bars represent the standard error of the mean of 6 biological samples (3 from each experimental replicate). Asterisks indicate statistical significance, * for $p < 0.05$ and ** for $p < 0.01$.

In addition to *lasR*, we assessed the expression of *rhlR* after the exposure of the biofilms to NPs. RhlR regulates rhamnolipid biosynthesis thereby affecting biofilm maintenance. Rhamnolipid is a bacterial surfactant that helps to regulate the biofilm channels for nutrients and metabolic waste transport (Maunder & Welch, 2017). LasR and RhlR are arranged in a hierarchical regulatory cascade in most of the *P. aeruginosa* isolates with LasR at the top, which means that generally a decrease in *lasR* gene expression (as seen in the 96 hrs biofilms treated with carboxylated NPs) is likely to affect the expression of *rhlR* (Wagner, Bushnell, Passador, Brooks, & Iglewski, 2003). There were no statistically significant differences in the normalized fold expression of *rhlR* in any of the biofilms (48 hrs and 96 hrs old) treated with NPs compared to the untreated biofilms (Control) (Figure 4.6).

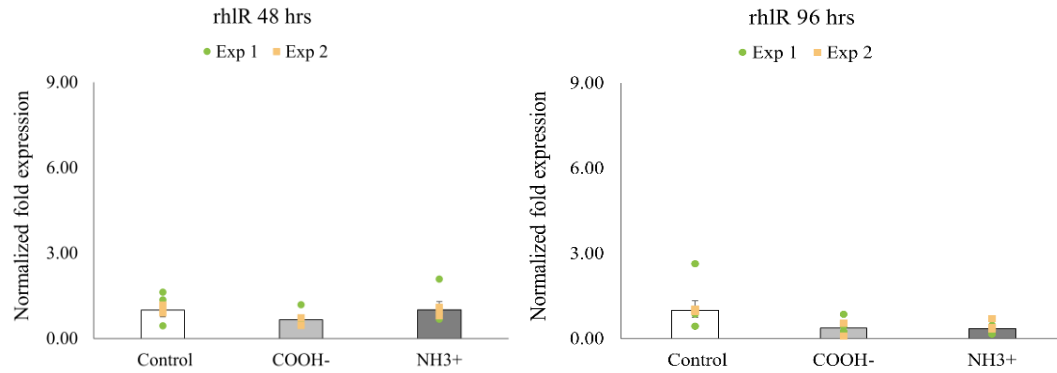


Figure 4.6: Normalized fold expression of *rhIR* transcription in the PAO1 $\Delta wspF \Delta psl P_{BADpel}$ bacterial strain for unexposed biofilms (Control) and NP treated biofilm samples (aminated- modified polystyrene (NH₃⁺) and carboxylated-modified polystyrene (COOH⁻)). The values correspond to triplicates of biological samples under each condition for two independent experiments normalized to the reference gene *ampR*. The error bars represent the standard error of the mean of 6 biological samples (3 from each experimental replicate). Asterisks indicate statistical significance, * for $p < 0.05$ and ** for $p < 0.01$.

The observed downregulation of *lasR* in the 96 hrs biofilms treated with carboxylated NPs did not cause an effect in the expression of *rhIR*. According to Soto-Aceves et al. (2019), the hierarchy of LasR and RhIR systems in *P. aeruginosa* could be strain dependent and should be revised after finding in their experiments the expression of RhIR in a *lasR* mutant strain.

Quorum-sensing signals can regulate extracellular DNA (eDNA) production. In the literature different mechanisms have been proposed to explain eDNA production such as autolysis and active secretion, but a common point in these studies is that eDNA is produced by a subpopulation of cells when the biofilm reaches a certain density in response to quorum-sensing signals. The *Las* and the quinolone signals (PQS) quorum sensing systems have been identified with eDNA production (Nakamura et al., 2008). In this study, the eDNA concentration was quantified for each condition (with and without

NP treatment) and the concentration was similar in 48 hrs and 96 hrs old biofilms as shown in Figure 4.7. There was no statistically significant difference between the eDNA concentration for biofilms treated with aminated and carboxylated polystyrene NPs and untreated biofilms. According to these results, even though the *Las* system is related to eDNA production, the decrease in the normalized fold expression of *lasR* due to carboxylated NP exposure in the 96 hrs biofilm samples did not have any significant effect on eDNA production. There is a base level of eDNA, production of which is independent of the quorum-sensing signals during the logarithmic growth phase, but cells in the biofilms of this study have already passed that stage (Allesen-Holm et al., 2006).

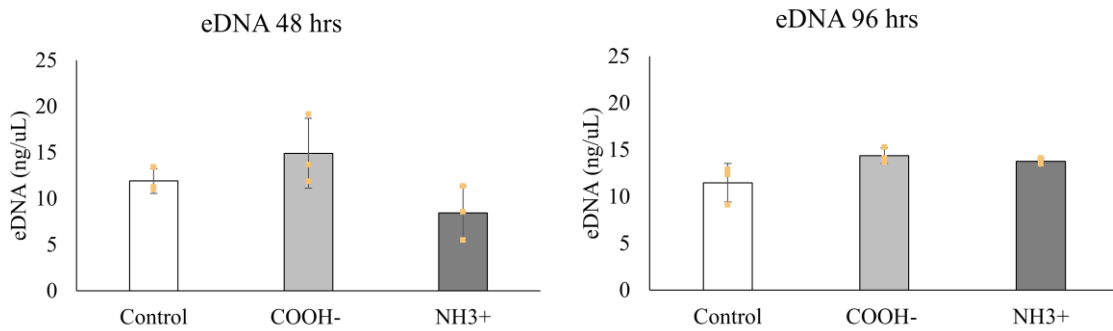


Figure 4.7: Concentration of extracellular DNA extracted from PAO1 $\Delta wspF \Delta psl$ P_{BADpel} unexposed (Control) and NP treated (aminated- modified polystyrene (NH₃⁺) and carboxylated-modified polystyrene (COOH⁻) biofilms. The values correspond to triplicates of biological samples under each condition for two independent experiments. The error bars represent the standard deviation of 6 biological samples (3 from each experimental replicate).

4.3.3 Aminated polystyrene nanoparticles can increase the *rpsL* gene expression

In this study, we quantified the expression of two reference (i.e., housekeeping) genes, *ampR* and *rpsL*, by the PAO1 $\Delta wspF \Delta psl$ P_{BADpel} strain under the conditions mentioned

in Section 4.2.2. The gene *ampR* is an ampicillin resistant gene and the *rpsL* is the gene for expression of the 30S ribosomal protein S12 which is important for maintaining translational accuracy. For the appropriate normalization of the genes expression, it is necessary that the expression of the reference genes stay constant under the experimental conditions (Derveaux, Vandesompele, & Hellemans, 2010). However, in this study the *rpsL* gene is not a good reference gene because in the 48 hrs biofilm samples after exposure to aminated polystyrene NPs there was a significant increase (p-value_{Exp1}=0.01, p-value_{Exp2}=0.02) in *rpsL* transcript absolute copy number in both independent experimental replicates (Experiment 1 and Experiment 2) (Figure 4.8).

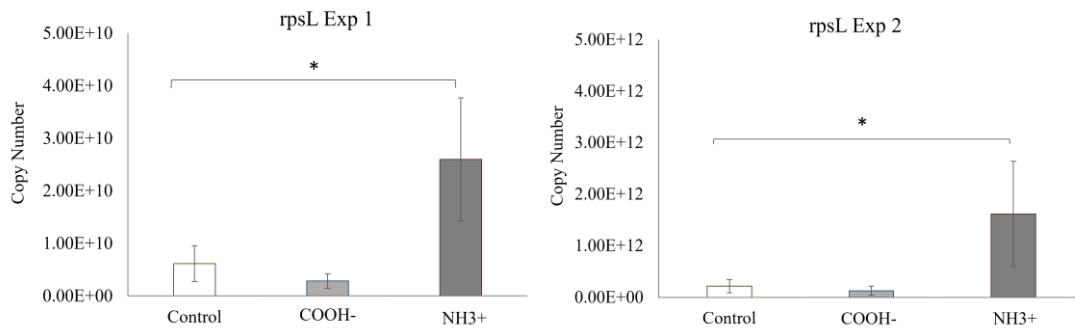


Figure 4.8: Absolute copy number of *rpsL* transcripts in the PAO1 $\Delta wspF \Delta psl P_{BADpel}$ bacterial strain for unexposed 48 hrs biofilms (Control) and NP treated 48 hrs biofilm samples (aminated- modified polystyrene (NH₃⁺) and carboxylated-modified polystyrene (COOH⁻)). The bar corresponds to the average of three biological samples under each condition. Experiment 1 and 2 are independent experimental replicates. The error bars represent the standard deviation. Asterisks indicate statistical significance, * for p < 0.05 and ** for p < 0.01.

The fold expression of *rpsL* transcriptions, normalized to the reference gene *ampR*, are presented in Figure 4.9. While a significant increase in *rpsL* transcription was observed at 48 hrs, for more mature biofilms (96 hrs old) there was no statistically significant

difference between the normalized fold expression of *rpsL* in biofilms treated with aminated and carboxylated polystyrene NPs and untreated biofilms. Increase in the expression of ribosomal subunits could increase ribosome concentrations thereby increasing total protein synthesis in the bacteria. In support of this idea, the increase in expression of the *rpsL* gene was reflected in the total protein concentration measured in the cell pellet portion of the 48 hrs biofilm samples treated with aminated NPs (Figure 4.10).

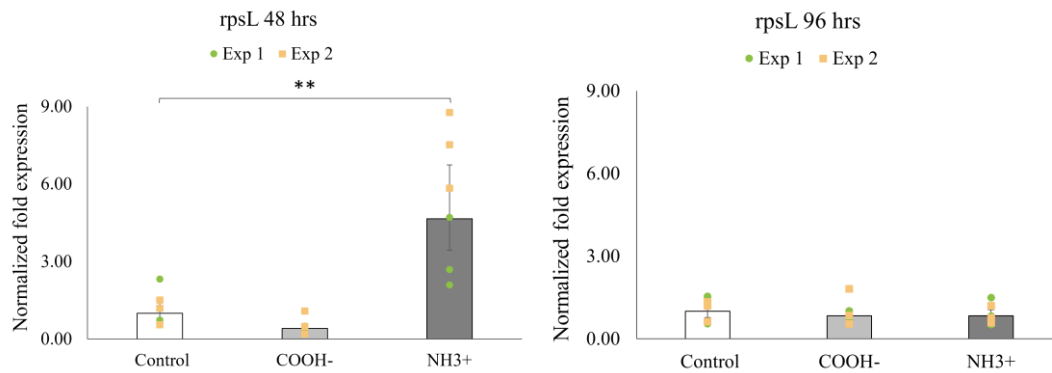


Figure 4.9: Normalized fold expression of *rpsL* transcription by the PAO1 $\Delta wspF \Delta psl P_{BADpel}$ bacterial strain for unexposed biofilms (Control) and NP treated biofilm samples (aminated- modified polystyrene (NH₃⁺) and carboxylated-modified polystyrene (COOH⁻)). The values correspond to triplicates of biological samples under each condition for two independent experiments normalized to the reference gene *ampR*. The error bars represent the standard error of the mean of 6 biological samples (3 from each experimental replicate). Asterisks indicate statistical significance, * for $p < 0.05$ and ** for $p < 0.01$.

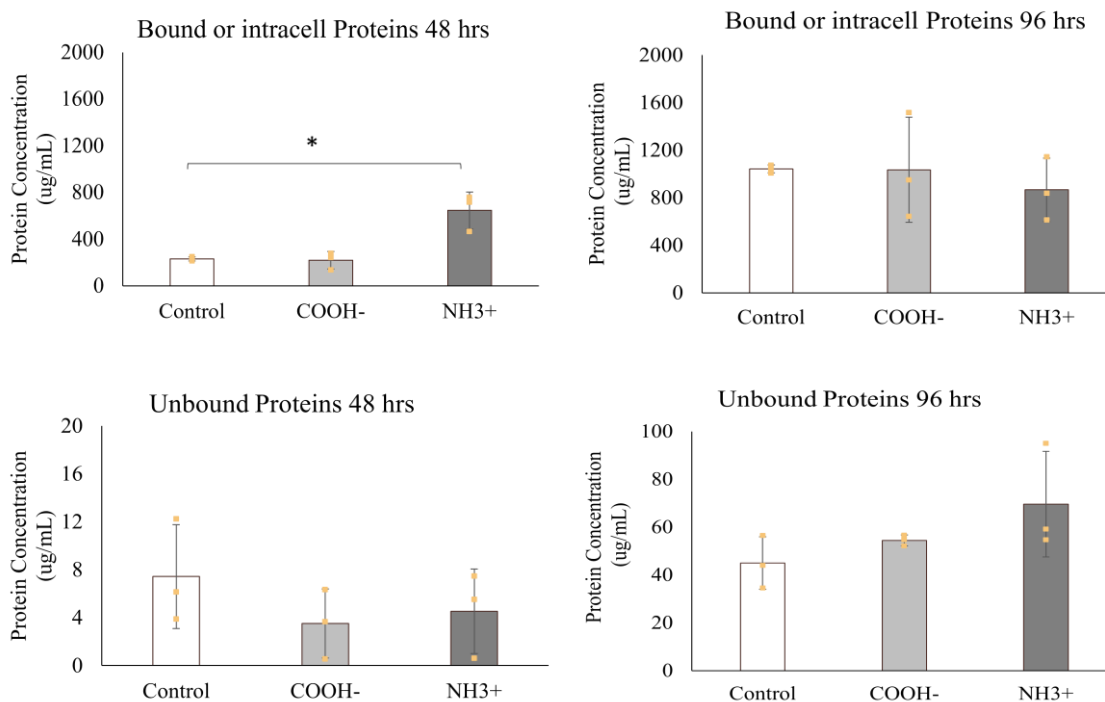


Figure 4. 10: Total protein concentration measured in the biofilm samples. The concentration of intracellular proteins and protein bound to the bacteria were measured in the cell pellet collected from the biofilm samples while the unbound proteins were measured in the sample supernatant using the Qubit protein assay kit. The values correspond to triplicates of biological samples under each condition for two independent experiments. The error bars represent the standard deviation of 6 biological samples (3 from each experimental replicate). Asterisks indicate statistical significance, * for $p < 0.05$ and ** for $p < 0.01$.

Gram-negative bacteria, like *P. aeruginosa* have a thin cell wall with a peptidoglycan layer and a lipopolysaccharide outer membrane which makes them more susceptible to NPs than Gram-positive bacteria which have a peptidoglycan layer on their surface. The negatively charged lipopolysaccharide outer membrane of *P. aeruginosa* can have electrostatic attractive interactions with the positively charge aminated NPs. For example, chitosan-based NPs, which contain amine groups, have been broadly used as drug delivery systems and display intrinsic antibacterial and antibiofilm activity due to their

polycationic nature capable which is associated with bacterial membrane disruption (Ilk, Sağlam, Özgen, & Korkusuz, 2017). Dynamic light scattering (DLS) Malvern Zetasizer NS (Worcestershire, U.K.) was used to measure the zeta potential and hydrodynamic diameter of the *P. aeruginosa* cells and the NPs. In 1 mM HEPES at 37° C, PAO1 $\Delta wspF$ Δpsl P_{BADpel} cells, the aminated polystyrene NPs and the carboxylated polystyrene NPs have zeta potential of -26 ± 1.7 mV, $+25 \pm 3.3$ mV and -34 ± 3.1 mV respectively. The average size of the cells increased from 515 ± 147 nm to $1,113 \pm 376$ when exposed to the aminated polystyrene NPs which is likely a result of NP attachment to the cell wall. As mentioned in the introduction, NPs can cause oxidative stress in cells producing damage to DNA, RNA, lipids and proteins. Aminated polystyrene nanoparticles have been found to induce ROS in an in vitro model of HeLa cells (Sharma, Gorey, & Casey, 2019). In response to ROS bacteria have antioxidant defense systems to protect the cells. In a previous study, researchers found that OxyR, a transcriptional regulator that can up-regulate the expression of defensive genes in *P. aeruginosa* when the cell is in contact with H₂O₂, is associated with the transcriptional regulation of *rpsL* (Hildebrand, Cornelis, Charlier, Hassett, & Ha, 2012). The authors hypothesized that in oxidative stress conditions *rpsL* would be under expressed based on previous studies where the protein synthesis was inhibited in response to oxidative stress by H₂O₂ (Palma, Deluca, Worgall, & Quadri, 2004). The qPCR experimental results in this study showed an increase in the expression of *rpsL* and in the intracellular/cell bound total protein concentration. Further studies are needed to elucidate the mechanisms behind this behavior in the *rpsL* transcription and identify possible explanations, like for example, if the aminated particles can cause errors in the bacterial translation and produce defective proteins like

the ribosome targeting aminoglycoside antibiotics (Glupeczynski, 1999; Pelchovich, Schreiber, Zhuravlev, & Gophna, 2013).

4.4 Conclusion

This study provides insights into the effects of biofilm exposure to aminated and carboxylated polystyrene nanoparticles and how biofilm maturity could play a role in cellular protection. Polystyrene NPs did not significantly affect younger biofilms (48 hrs) of PAO1 $\Delta wspF \Delta psl P_{BADpel}$ but in more mature biofilms (96 hrs) there was a decrease in *pelA* transcription after NP exposure independently of the particle surface properties. However, transcription levels of *lasR* and *rpsL* were dependent on NP surface functionalization. Carboxylated polystyrene nanoparticles decreased *lasR* gene expression in 96 hrs old biofilms while in younger, 48 hrs old, biofilms aminated polystyrene nanoparticles increased *rpsL* gene transcription. These results suggest that even simple polystyrene NPs may be stressors for *P. aeruginosa* and lead to changes in the production of polysaccharides and quorum sensing signals, but the effects will depend on NP surface charge, gene function and biofilm age, which were the variables considered in this study.

Further studies are needed to identify the mechanisms and processes behind the behaviors identified in this study after the PAO1 $\Delta wspF \Delta psl P_{BADpel}$ exposure to polystyrene NPs and the direct implications on biofilm architecture and metabolic efficiency. In order to identify the mechanisms that are causing the down and up regulation of the genes a similar approach to the one used in previous Chapters in where the system was simplified to two or three components could be used. A systematically increase in complexity of the

biological system combined with viability assays and gene expression analysis can help to understand if what is affecting the gene transcription is a direct interaction of the NP with the cells or if it is induced as a response of the cell due to NPs interaction with other biofilm components.

To understand the complex system of biofilms, it would be useful to know the quantity of basic biofilm components (e.g., number of viable cells (CFU) and concentration of EPS components), the spatial distribution of cells and the 3 dimensional characteristics of biofilm architecture (Kassinger & Hoek, 2020). Studies designed to quantify the effects in the biofilm properties due the down and upregulation of genes caused by the NP precedence could help to identify the consequences of the results observed in this study. For example, the effects on the biofilm composition due to the downregulation of *pelA* by cationic and anionic NP in mature biofilms could be evaluated using extraction and analytical methods to quantify *Pel* (Jennings et al., 2015) to identify changes in biofilm composition, and experiments to measure the biofilm dispersal and maturity could help to elucidate the implications of the quorum sensing genes downregulation in the biofilm growth mechanisms.

In addition, studies with changes in the bacterial strain, growth conditions, biofilm exposure time to the NPs and NP's solution chemistry and concentration could help to determine how bacterial resilience and biofilm properties (charge, composition and physical properties) changes as a function of the environmental conditions that can regulate the bacteria metabolic capabilities and change the NP properties (charge, size and surface chemistry).

CHAPTER 5

DIFFUSION OF POLYSTYRENE NANOPARTICLES IN PSEUDOMONAS AERUGINOSA BIOFILMS AS A FUNCTION OF PARTICLE CHARGE AND BIOFILM MATURITY

5.1 Introduction

Biofilms are complex structures of microorganisms embedded in a heterogeneous matrix of macromolecules well known as extracellular polymeric substances (EPS). In previous studies of nanoparticles and biofilm interactions, it has been shown that EPS can affect the deposition and diffusion rate of nanoparticles (McGill et al. 2009; Ikuma et al. 2014; Thuptimdang et al. 2015). But EPS is a complex matrix with multiple components (proteins, lipids, nucleic acids and various polysaccharides). To reduce the complexity, researchers have simplified the matrix by studying biofilms using model matrices similar to the alginate study presented in Chapter 3 (Ikuma, Madden, Decho, & Lau, 2014; Rodríguez-Suárez, Butler, Gershenson, & Lau, 2020; Wloka et al., 2004). However, the microorganisms intrinsic to biofilms can change EPS properties across the different stages of biofilm formation and maturation and through cellular responses to environmental stimulus. Due to these variations in biofilm physicochemical properties, there are few experimental studies of diffusion modes in natural biofilms, even in the simplest living biofilms formed by a single microorganism species under controlled conditions. Studies that can characterize NP diffusion in the context of environmental biofilm development and alterations in natural biofilm properties over time could help

improve our understanding of the fate and transport of NPs in environmental and engineered systems.

5.1.2 Specific Objectives

We previously used alginate cross-linked with calcium as a model to describe biofilms (Chapter 2 and 3) which can be considered passive because any changes were a result of the chemistry of the surrounding environment. Natural biofilms are much more dynamic and active with responsive interchange between the microbial inhabitants and the biofilm structure (Chapter 4). The mobility of nanoparticles in biofilms will be dictated by the physicochemical properties of the particle but also the time and environment dependent biofilm properties. In this study, we used *Pseudomonas aeruginosa* biofilms, similar to the ones used in Chapter 4, to characterize the diffusion of aminated and carboxylated modified polystyrene nanoparticles. The specific objectives of this study were:

- 1) to characterize the diffusion of polystyrene nanoparticles in *Pseudomonas aeruginosa* biofilms as a function of particle charge and,
- 2) to identify the role of biofilm maturity in the diffusion coefficients and diffusive mode of the nanoparticles.

Combined with the results in Chapter 4, these studies provide a window into the complex interplay between nanoparticles, microbial transcription, and biofilm architecture.

5.2 Materials and Methods

5.2.1 Biofilm cultivation and nanoparticle treatment

For this study, we cultivated *Pseudomonas aeruginosa* biofilms following the same methods detailed in Chapter 4. Briefly, the flow cell chambers were inoculated with a diluted fresh overnight culture of the PAO1 $\Delta wspF \Delta psl P_{BADpel}$. The biofilms were cultivated in Jensen's minimal glucose media to promote biofilm formation (Jennings et al., 2015). To inoculate the flow cell chambers, a volume of 5 mL of the diluted bacterial inoculum was added to each flow cell chamber. Cells were allowed to attach to the glass coverslip substratum for 3 hours before starting the media flow. Biofilms were grown for 48 and 96 hours in a controlled temperature room at 37°C and with a constant flow of fresh media. Biofilms were cultivated for 48 and 96 hours in 3 flow cells for a total of 9 chambers with biofilm replicates (See Figure 4.3). When the biofilms reached the desired age (48 hrs or 96 hrs), all nine chambers containing biofilms were washed with 5 mL of 1 mM HEPES buffer (pH 7.14) and after the washing step, 5 mL of 1 mM HEPES (pH 7.14) buffer was added to each chamber of the "Control" flow cell. In the "Cationic NP" flow cell, 5 mL of solution of positively charged fluorescent aminated modified polystyrene beads (Invitrogen FluoSpheres, max abs/em: 580/605 and $d = 64 \pm 3.4$ nm) were added while in "Anionic NP" flow cell, negatively charged fluorescent carboxylated modified polystyrene beads (Invitrogen FluoSpheres, max abs/em: 580/605 and $d = 63 \pm 3.1$ nm) were added. The NPs were suspended in 1 mM HEPES buffer (pH 7.14) at a concentration of 100 mg/L. The microscopy data was recorded after 6 hours of biofilm exposure to the NPs under static conditions. The experiment was repeated twice for each biofilm age (Experiment 1 and 2).

5.2.2 Microscopic data acquisition

The samples were observed, without opening the flow cells or disturbing the biofilm, using the Nikon CrestV2 Spinning disk confocal, which is a low-light technique appropriate for live cells imaging, with a sCMOS Prime 95B camera. For each biofilm sample, 6,000 frames of data were collected at a rate of 100 frames/s using an Apo TIRF 100x NA 1.49 objective at the point in the z axis in where the fluorescence from the NPs were first observed ($z = 4500 \pm 703 \mu\text{m}$, relative to the coverslip). The red fluorescent NPs were excited with a 561 nm laser and a laser power of 38 mW (50% of the maximum, 75 mW, fiber output for 561 nm), for both, the aminated and carboxylated modified polystyrene nanoparticles. For each sample three fields of view of 256 x 256 pixels (0.11 $\mu\text{m}/\text{pixel}$) were recorded to collect images from different locations of the biofilm. The samples from the “Control” flow cell, was observed to account for any background fluorescence.

5.2.3 Methods used for the microscopy data analysis

To characterize NP diffusion and the structural features of 48 and 96 hrs PAO1 $\Delta wspF$ Δpsl P_{BADpel} biofilms, the microscopic images were analyzed using correlation analysis and single particle tracking. Two-dimensional pair correlation function (2D-pCF) was used to generate connectivity maps. A detailed description of this method can be found in Chapter 1. 2D-pCF was an appropriate method to visualize features of the biofilm matrix that require high spatial resolution (e.g., barriers for NP diffusion) because it does not rely on a spatial average. The analysis was performed using a pCF pixel distance of 4, detecting temporally and spatially correlating fluorescence at a random adjacent location

at a maximum distance of 0.44 μm (4 pixels) away. For the connectivity maps, the arrow length (line length) selected was 5 pixels (0.55 μm).

Single particle tracking (SPT) was used to analyze individual tracks of the NPs moving through the biofilm, obtain mean square displacement (MSD) curves and to perform a particle count. The SPT analysis was done using the algorithm in the NIS-Elements software (Nikon's universal software platform) (Jaqaman et al., 2009). Please refer to Chapter 1, section 1.4.1, for more details of this algorithm. For this study, a random motion model was selected, and it allowed gaps in tracks of a maximum size of 10 frames based on the average time a particle stayed visible in the microscopic images. All trajectories longer than 50 frames were selected; shorter tracks were not considered in the analysis.

For the identification and visualization of the spatial distribution of diffusion modes and NP diffusion coefficients (D), an image Mean Square Displacement (iMSD) analysis was performed. One of the advantages of using iMSD, as discussed in Chapter 1, is that it is based on the calculation of mean square displacements (MSD) allowing the visualization of the distribution of diffusion coefficients in the form of maps (Malacrida, Rao, et al., 2018). The iMSD method was used to identify and visualize the spatial distribution of diffusion modes and the diffusion coefficients (D) of NPs moving in the 48 and 96 hrs old biofilm samples. For the iMSD analysis, a region of interest (ROI) of 32 x 32 pixel and a moving window with an ROI overlap of $\frac{1}{4}$ (8 X 8 pixels) was selected for the scanning analysis. The data was analyzed using the "all models" option for diffusion (free diffusion, confined, and partially confined) because a wide variety of diffusion behaviors was observed in the microscopic images.

5.2.4 Statistical Analysis

Statistical analysis comparing the difference between the histograms of diffusion coefficients obtained by the iMSD analysis was performed in R using the permutation test of symmetry where the levels of the various conditions were treated as having paired or repeated data. The R coding for this analysis can be found in the Appendix C. If the p-value was lower than 0.05 then the null hypothesis that there was no difference between the distributions was rejected.

5.3 Results and Discussion

5.3.1 Aminated and carboxylated nanoparticles can bind to EPS components in biofilms

After 6 hours of exposure to aminated and carboxylated polystyrene NPs, the biofilm samples were observed under the Nikon CrestV2 Spinning disk confocal. The samples from the “Control” flow cell, were observed to quantitate any background fluorescent from the biofilm. No significant fluorescence emission from the biofilm only control samples were detected for 561 nm laser wavelength excitation. Representative images collected from samples of biofilms with NPs is presented in Figure 5.1. The number of particles in the field of view was lower for biofilm samples with aminated NPs compared to biofilm samples with carboxylated NPs. The average number of particles obtained from a single particle tracking (SPT) analysis are presented in Table 5.1. Similar trends were found in Experiment 1 and 2, however, more NPs (aminated and carboxylated) were detected in Experiment 2. Particle aggregation or possible NP binding to biofilm components was observed in all the 48 hrs and 96 hrs biofilm samples. Before adding the

NP solution to the flow cell chamber, a wash step was performed to reduce aggregation of the NPs due to the cultivation media. If the wash step was effective removing the liquid media in the chamber, it is possible that the carboxylated and aminated NPs observed (Figure 5.1) bound to biofilm components by electrostatic potentials. In the case of the PAO1 $\Delta wspF \Delta psl P_{BADpel}$ strain, the biofilm matrix contains negatively charge components (e.g., eDNA) as well as positively charged polysaccharides (e.g., *Pel*). In 1 mM HEPES (pH = 7.14) at 37° C the aminated polystyrene NPs and the carboxylated polystyrene NPs have zeta potentials of $+25 \pm 3.3$ mV and -34 ± 3.1 mV.

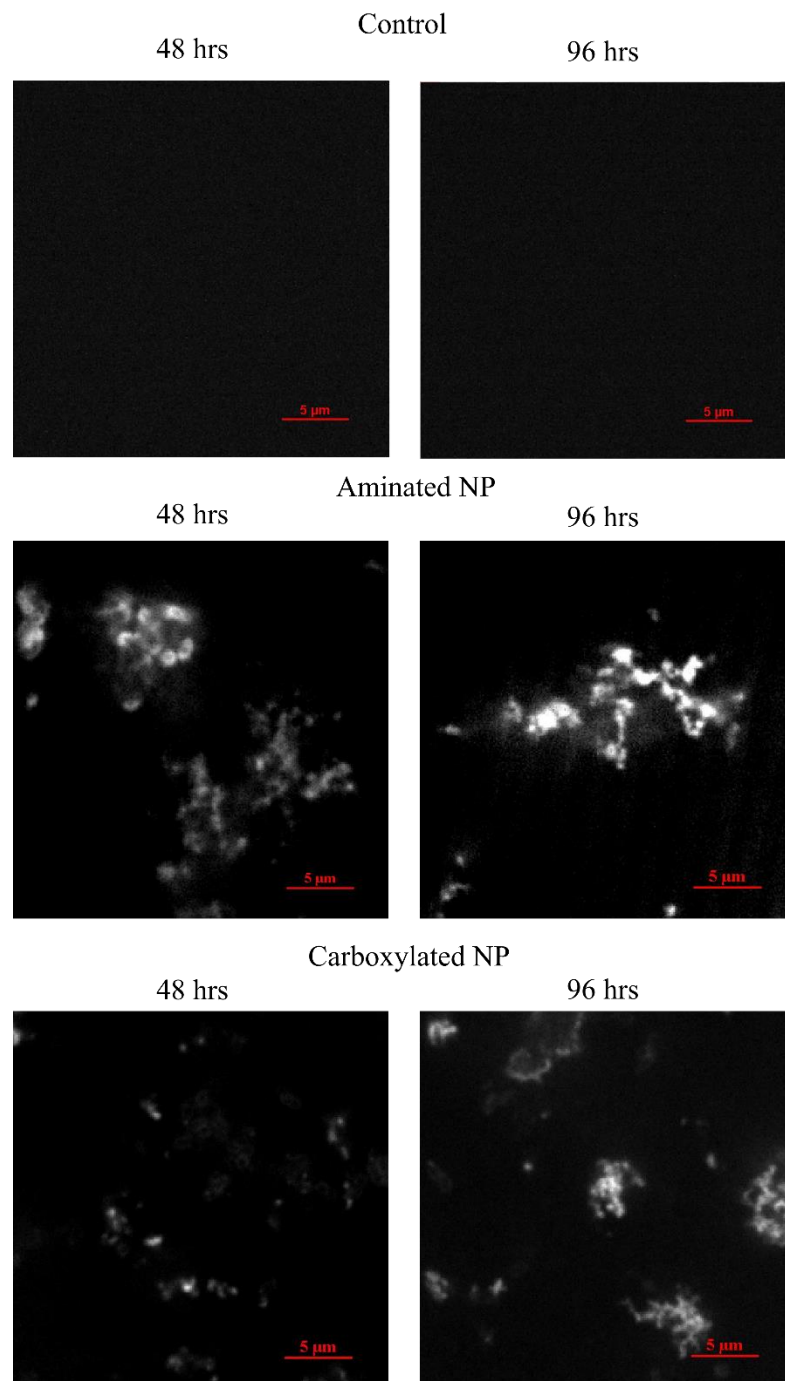


Figure 5.1: Microscopy images from one field of view for each condition considered in this study. The fluorescent areas (white areas) are the aminated and carboxylated nanoparticles excited with a 561 nm laser. A control sample of a biofilm without nanoparticles was observed to identify possible background fluorescence emitted from the biofilm components. The scale bar (red) in each image is 5 μm and the images were recorded at a depth of $z = 4500 \pm 703 \mu\text{m}$.

Birjiniuk et al., (2014) previously identified a strong dependence between carboxylated NPs mobility in biofilms with the particle interactions with charged portions of the EPS. The EPS components are mostly negatively charge. However, PAO1 $\Delta wspF \Delta psl$ P_{BADpel} is a *Pel* overproducer strain when cultivated with the arabinose inducer (Stewart, 2003) and attractive forces between the cationic exopolysaccharide *Pel* and the carboxylated NPs are expected (Jennings et al., 2015). This probable attraction likely explains the apparent binding of carboxylated NPs to the biofilm matrix. An electrostatic potential between the NPs and bacterial cells can also lead to NP binding. The zeta potential of PAO1 $\Delta wspF \Delta psl$ P_{BADpel} cells in 1 mM HEPES (pH 7.14) of -26 ± 1.7 mV and the increase in size of PAO1 $\Delta wspF \Delta psl$ P_{BADpel} cells after its exposure to aminated NPs (from 515 ± 147 nm to $1,113 \pm 376$ nm) observed by DLS (Chapter 4) suggest that aminated particles can bind to the bacterial cells and to EPS components.

Table 5.1: Average number of aminated and carboxylated polystyrene NPs identified in a microscopy video of 6,000 frames (3 minutes) for the 48 hr and 96 hr biofilm samples. The average values are considering 3 fields of view from each sample in an area of $793 \mu\text{m}^2$. Experiment 1 and 2 are independent experimental replicates.

Condition		48 hr biofilm	96 hr biofilm
Experiment 1	NH_3^-	36 ± 6	35 ± 33
	COOH^-	63 ± 25	152 ± 27
Experiment 2	NH_3^-	52 ± 20	62 ± 13
	COOH^-	84 ± 36	190 ± 43

The connectivity maps, which illustrate the space in the biofilm network that the NPs are able to access (biofilm voids), are presented in Figure 5.2. In the studies of NP diffusion in a model alginate matrix (Chapter 3), we identified clear differences in the areas the particles were able to access in a heterogeneous polymeric matrix due to the differences in particle size. In this study the particles have similar size ($d_{\text{NH}_3^+} = 64 \pm 3.4$ nm and $d_{\text{COOH}^-} = 63 \pm 3.1$ nm) and the only difference between them is the functional groups at the particle surface. There are no clear differences in the connectivity maps suggesting that the particle charge doesn't affect the types (in terms of shape and size) of areas the NPs can access. However, the connectivity maps show different void shapes and sizes likely indicating the heterogeneity of the void spaces in these bacterial biofilms.

There are no clear differences between connectivity maps for the 48 hr biofilms and the 96 hr biofilm, which could mean that the matrix structural changes due to biofilm maturity doesn't affect the voids that the 50 nm particle can access. In our previous study, we used NPs with different diameters to identify voids of different sizes in a model polysaccharide, similar studies using more particle sizes could help to identify changes in biofilm voids as the bacterial biofilms mature.

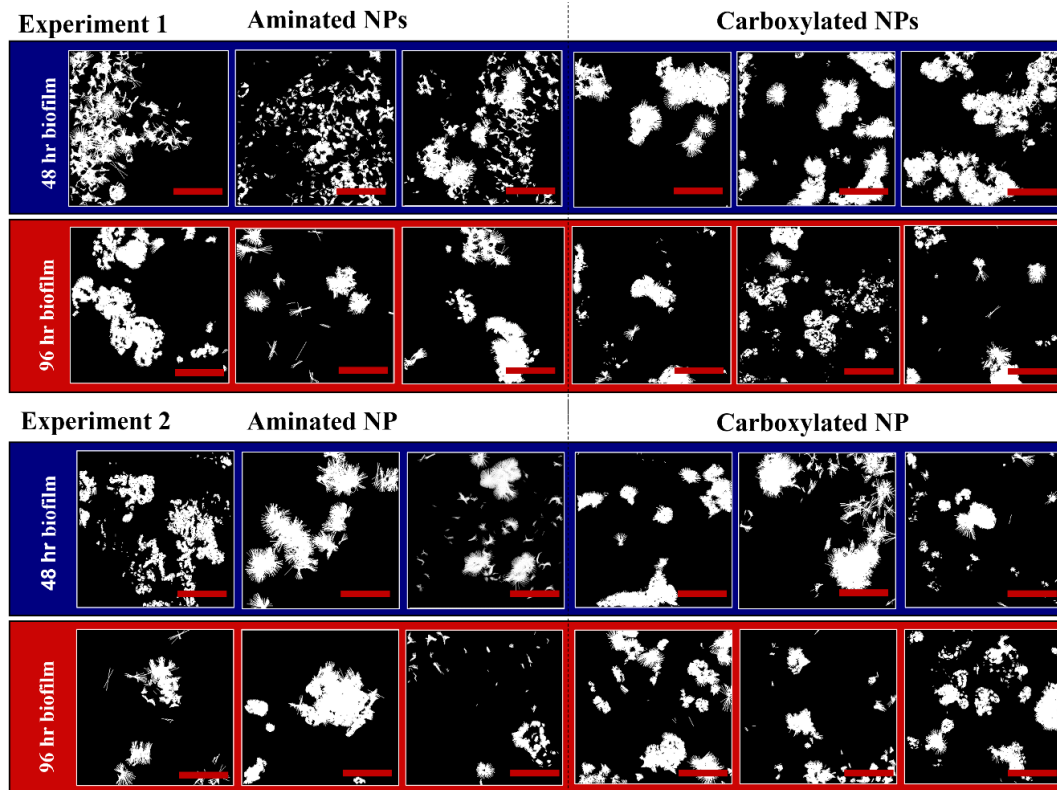


Figure 5.2: Connectivity maps for all three fields of view ($28.2 \mu\text{m} \times 28.2 \mu\text{m}$) obtained by 2D-pCF analysis for the aminated and carboxylated NPs at a depth of $z = 4500 \pm 703 \mu\text{m}$. The two top rows correspond to biofilms from Experiment 1 and the two bottom rows to biofilms from Experiment 2. Experiment 1 and 2 are experimental replicates. Each row shows each field of view analyzed for the 48 hr biofilm samples (blue) and the 96 hr biofilms samples (red). The scale bar (red) in each map is $10 \mu\text{m}$.

5.3.2 Nanoparticle diffusion in biofilms depends on biofilm maturity and particle charge

The diffusion of aminated and carboxylated NPs in PAO1 $\Delta wspF \Delta psl P_{BADpel}$ was characterized in terms of diffusion coefficients (D) calculated from the microscopy images using the image mean square displacement analysis (iMSD). The visual maps of D revealed spatial variability in NP diffusion coefficients throughout the biofilm network (Figure 5.3 and 5.4). The overall behavior of the aminated and carboxylated nanoparticles

in Experiments 1 and 2 was similar, the D for aminated NPs in 48 hr biofilms samples were lower (p-value_{Exp1} = 0.003, p-value_{Exp2} = 0.001) than the D for the carboxylated NPs and similar diffusion coefficients were calculated for both types of NPs diffusing in 96 hr biofilm samples (p-value_{Exp1} = 0.866, p-value_{Exp2} = 0.146). These results concur with a previous study of NPs diffusing in 2 day old *Escherichia coli* biofilms, where the carboxylated NPs were more mobile than aminated NPs (Birjiniuk et al., 2014). The observation that anionic particles have similar diffusion coefficients to cationic particles in 96 hr biofilms could be due cationic and anionic patches that EPS components could have at the nanoscale that may be more significant in more mature biofilms (Ikuma et al., 2014). The average D values were not exactly the same for both experimental replicates, agreeing with previous experiments that have identified variability in biofilms produced from the same monoculture (Peulen & Wilkinson, 2011). However, when comparing the D distributions between samples from Experiment 1 and 2, there was no statistical difference (all p-value between samples replicates were > 0.05). As observed with the alginate model biofilms, the use of distributions instead of average values to characterize NP diffusion and compare biofilm replicates highlights the intrinsic heterogeneity (microdomains) of the biofilm matrix. Moving towards using distributions of D instead of effective D values to compare results from diffusion studies in heterogeneous matrixes (under similar conditions) could reduce the discrepancies between D values in biofilm replicates that researchers have previously reported (Peulen & Wilkinson, 2011). Peulen & Wilkinson (2011) studied the diffusion of carboxylated polystyrene NPs of 57 nm in 9-15 hrs old biofilms of *P. fluorescence* under static conditions using fluorescence correlation spectroscopy. The calculated D was higher ($D = 5.4 \mu\text{m}^2/\text{s}$) compared to the

values we obtained in this study ($D = 0.31 - 0.68 \mu\text{m}^2/\text{s}$), but this could be due to the difference in bacterial strain, time of NP exposure, and biofilm age and cultivation conditions considered in both studies which are all factors that can affect biofilm physicochemical properties.

The diffusion coefficients values for the carboxylated polystyrene NPs in this study are less than the ones obtained for 20 nm and 100 nm particles with similar chemical composition diffusing in alginate (with and without calcium cross-linking), previously presented in Chapter 3, but greater than the D calculated for the 200 nm ones. In bacterial biofilms, it is reasonable to have lower D than in a single component polymeric matrix due to the interaction between EPS components (proteins, nucleic acids, lipids and polysaccharides) that could affect the viscosity, pseudoplasticity and elasticity of the matrix (Benigar et al., 2016) and restrict NP mobility.

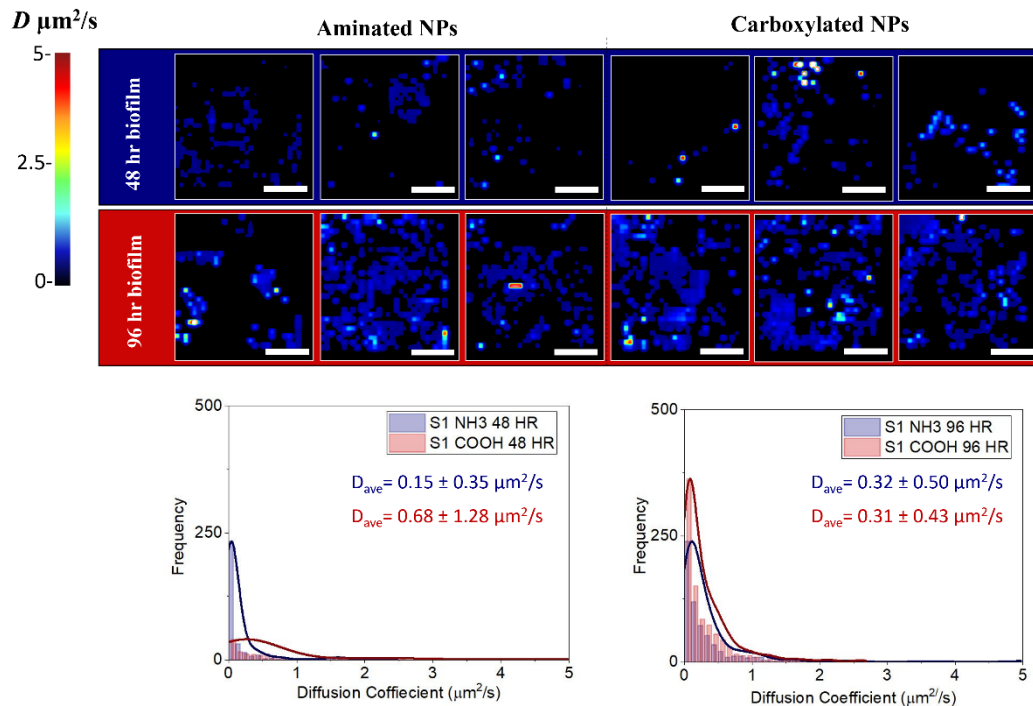


Figure 5.3: Visual maps and diffusion coefficient histograms for the aminated and carboxylated polystyrene nanoparticles at diffusing at a depth of $z = 4500 \pm 703 \mu\text{m}$. The diffusion coefficients were obtained from the iMSD analysis from Experiment 1. The bars are histograms with bins sizes of $0.1 \mu\text{m}^2/\text{s}$. The lines are kernel (Scott) probability density estimates of the diffusion coefficient (D) distributions. Each row shows the maps from the 48 hr and 96 hr biofilm samples. The D map color scale goes from black to red. The red areas are the areas with higher D values (faster diffusion) and the darker areas the ones with the lower D values (slower diffusion). The color-coded values in the distribution graphs are average values of the D distributions taking into consideration all 3 fields of view analyzed. The scale bar (white) in each map is $10 \mu\text{m}$.

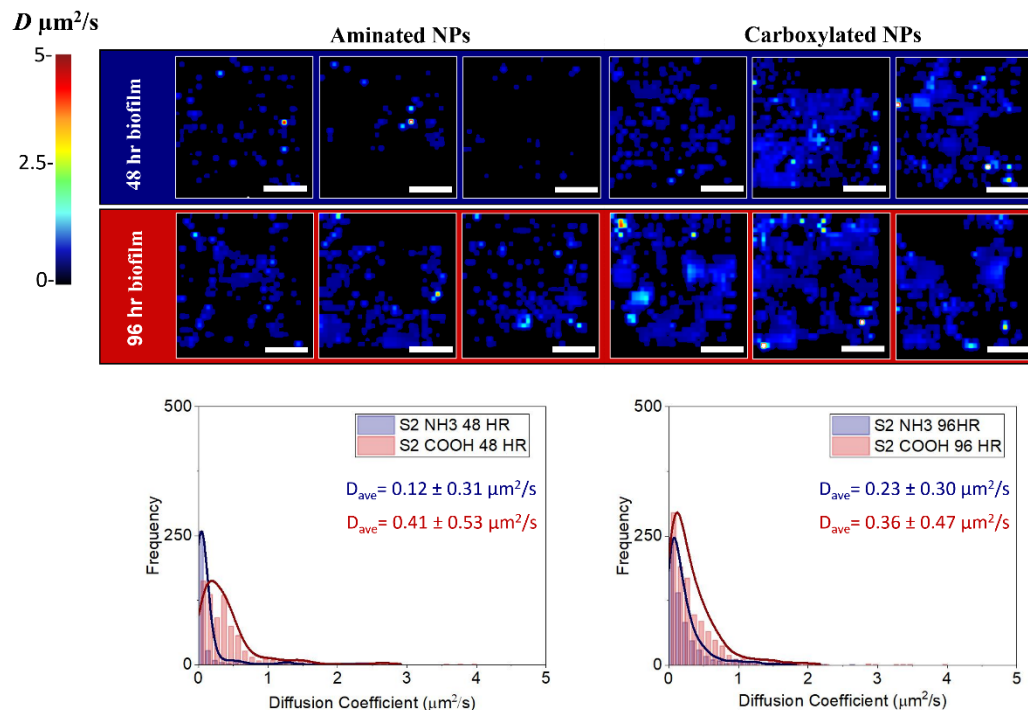


Figure 5.4: Visual maps and diffusion coefficient histograms for the aminated and carboxylated polystyrene nanoparticles nanoparticles at diffusing at a depth of $z = 4500 \pm 703 \mu\text{m}$. The diffusion coefficients were obtained from the iMSD analysis from Experiment 2. The bars are histograms with bins sizes of $0.1 \mu\text{m}^2/\text{s}$. The lines are kernel (Scott) probability density estimates of the diffusion coefficient (D) distributions. Each row shows the maps from the 48 hrs and 96 hrs biofilm samples. The D maps color scale goes from black to red. The red areas are the areas with higher D values and the darker areas the ones with the lower D values. The color-coded values in the distribution graphs are average value of the D distributions taking in consideration all 3 fields of view analyzed. The scale bar (white) in each map is $10 \mu\text{m}$.

5.3.3 Nanoparticles can display different diffusion modes in biofilm matrices

Similar to the results from the alginate study presented in Chapter 3, when NPs diffuse in a biofilm heterogeneous matrix, NPs can be free diffusing, confined by the biofilm matrix or confined for a period of time before resuming free diffusion. From the iMSD analysis, maps of diffusion modes were obtained and presented in Figure 5.5. Overall, the modes of NP diffusion changed as a function of the biofilm maturity. For both the aminated and

carboxylated NPs, partial confinement areas (red) increased in the 96 hr biofilm when compared to the 48 hr biofilms. However, the percent of the maps showing confinement increased for the carboxylated NPs but decreased for the aminated ones. These results are consistent with the D values presented in Figure 5.3 and 5.4 in where the D of the carboxylated NPs decrease in mature biofilms compared to the D in younger biofilms and for the aminated NPs the D increase in the 96 hrs biofilms (mature).

In Experiment 2, biofilms formed by the same *P. aeruginosa* strain under the same conditions used in Experiment 1, the changes in the modes of diffusion were different. In Experiment 2, the observed increase in D for the aminated NPs (Figure 5.4) in the more mature biofilms, seems to be related to an increase in the areas of free diffusion instead of in the areas of partial confinement. In the case of the carboxylated NPs, the D for NP diffusion in the 48 hr biofilms was lower in Experiment 2 compared to Experiment 1 ($D_{\text{Exp1}} = 0.68 \pm 1.28 \mu\text{m}^2/\text{s}$ and $D_{\text{Exp2}} = 0.41 \pm 0.53 \mu\text{m}^2/\text{s}$, p-value= 0.0003), which seems to be related with the increase in areas of partial confinement observed in the 48 hr biofilms in Experiment 2 (Figure 5.6). These differences between experimental replicates emphasizes again the variability that biofilms can have even when formed in similar, well-controlled conditions and by the same microorganism. In addition, these results suggest that even in matrices where the NPs have similar average diffusion coefficients, the modes of diffusion could be different.

Changes in the diffusion modes between biofilms with different age could be related to the possible binding of the NPs to the biofilm components which can make NP movement dependent on the movement of cells and other components of the biofilm matrix. This mechanism was presented previously as the mobility of the bound complex.

If a particle is bound to a biofilm component that is itself diffusing, then the particle will be taken along with that component's translational motion (Sprakel et al., 2007). If the cationic particles are for example, bound to the PAO1 $\Delta wspF \Delta psl P_{BADpel}$ cells, then the NP diffusion could be slowed down because the cells move more slowly than the NPs. In a previous study of single microcolony diffusion in *P. aeruginosa* biofilms the diffusion coefficients depended on the microcolony size and were close to the values obtained in the biofilm samples from this study, for larger microcolonies $D = 0.28 \pm 0.12 \mu\text{m}^2/\text{s}$ and for smaller ones $D = 0.49 \pm 0.25 \mu\text{m}^2/\text{s}$ (Sankaran, Tan, But, Cohen, & Rice, 2019).

If the NP is bound to a polymer, then the DCL of the polymer could influence the overall NP diffusion coefficient (D). If carboxylated NPs were able to bind to the cationic polysaccharide (*Pel*) produced by PAO1 $\Delta wspF \Delta psl P_{BADpel}$, this could explain why the areas of confinement increased in the 96 hrs biofilm samples. Polymers with lower DCL that are weakly physically cross-linked and flexible will allow faster polymer dynamics which might increase the probability of escape from confinement (Witten & Ribbeck, 2017). In this case, the confinement mode of the carboxylated NP diffusion could increase due to an increase in the *Pel* DCL due to the biofilm maturity.

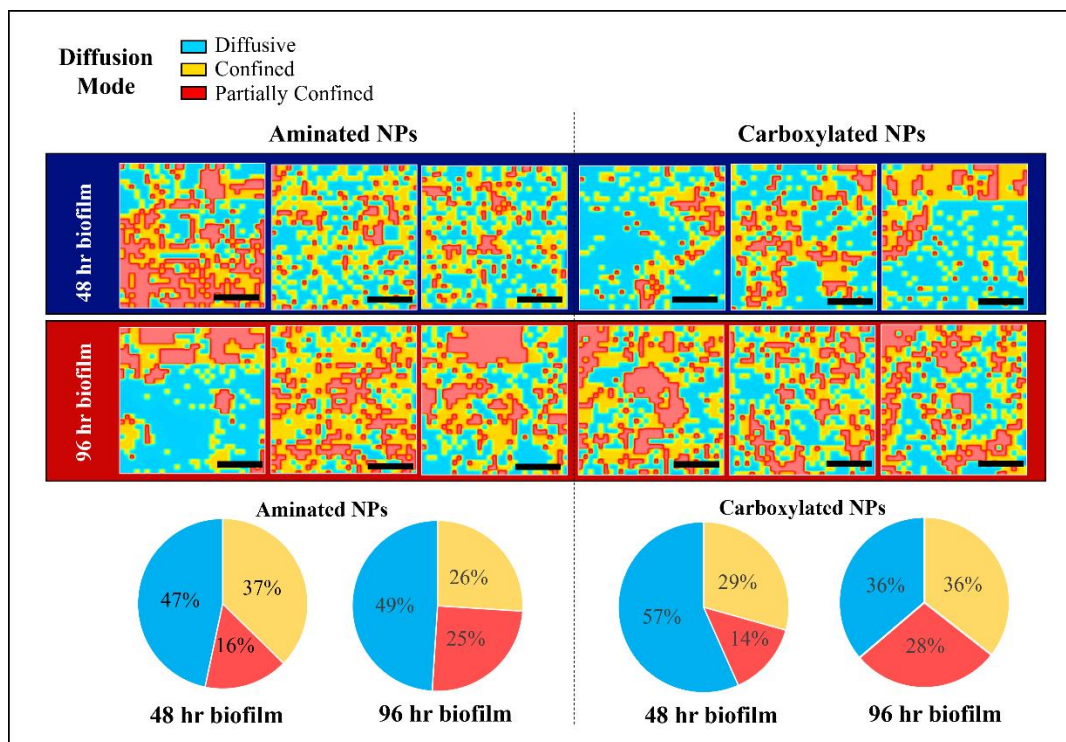


Figure 5.5: Maps of diffusion modes, freely diffusive (blue), confined (yellow) and partially confined (red). Each row shows each field of view analyzed for the 48 hr biofilms and the 96 hr biofilm samples in Experiment 1. The pie charts represent the average percentage (of the three fields of view analyzed) showing free diffusion (blue), confined (yellow) or partially confined (red) areas for each type of NP. The scale bar (black) in each map is 10 μm and the z depth was $4500 \pm 703 \mu\text{m}$.

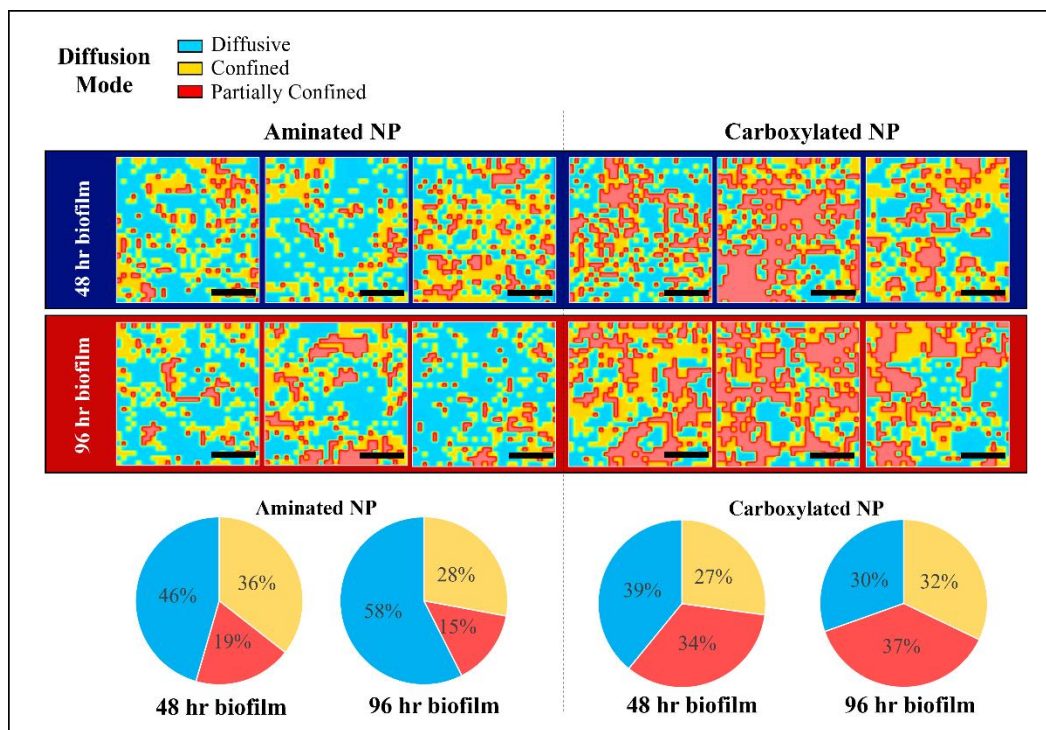


Figure 5.6: Maps of the distribution of diffusion modes, freely diffusive (blue), confined (yellow) and partially confined (red). Each row shows each field of view analyzed for the 48 hrs biofilms and the 96 hrs biofilms samples in Experiment 2. The pie charts represent the average percentage (of the three field of views analyzed) of free diffusion (blue), confined (yellow) or partially confined (red) areas for each type of NP considered. The scale bar (black) in each map is 10 μm and the z depth was $4500 \pm 703 \mu\text{m}$.

The iMSD is a correlation method that reports on the average diffusion behavior (in two dimensions) at each point of the image, providing a better understanding of how particles move in an specific spatial location in the biofilms (Digiacomio et al., 2016). For a more detailed analysis that includes the timescale of the diffusion behaviors, a combination of correlation methods with single particle tracking (SPT) should be used. Figure 5.7 and Figure 5.8 shows the mean square displacement (MSD) for Experiment 1 and 2 biofilms. The MSD curves obtained from SPT agree with the trends in the diffusion coefficient (D) values obtained from the iMSD analysis. Figure 1.6 from Chapter 1 shows the MSD

curves behaviors for each diffusion mode (free diffusion, confined and partially confined). The aminated NPs have more linear MSD curves in the 96 hr biofilms than in the 48 hr biofilm samples which agrees with the increase in D in the 96 hr biofilms. In the case of the carboxylated NPs, D was lower in the more mature biofilms which concurs with the increase in flat MSD curves in the MSD graphs (Figure 5.7 and 5.8). These MSD graphs allow you to see the time scale for confinement. The timescale for each particle to shift from one diffusion mode to a different one (represented in the MSD curve by changes in the slope) is unique for each particle and seems to depend on the local physicochemical features of the network where the particle is located. Because the biofilm matrix is heterogeneous and has structural and chemical microdomains MSDs with different behaviors for each individual particle are expected.

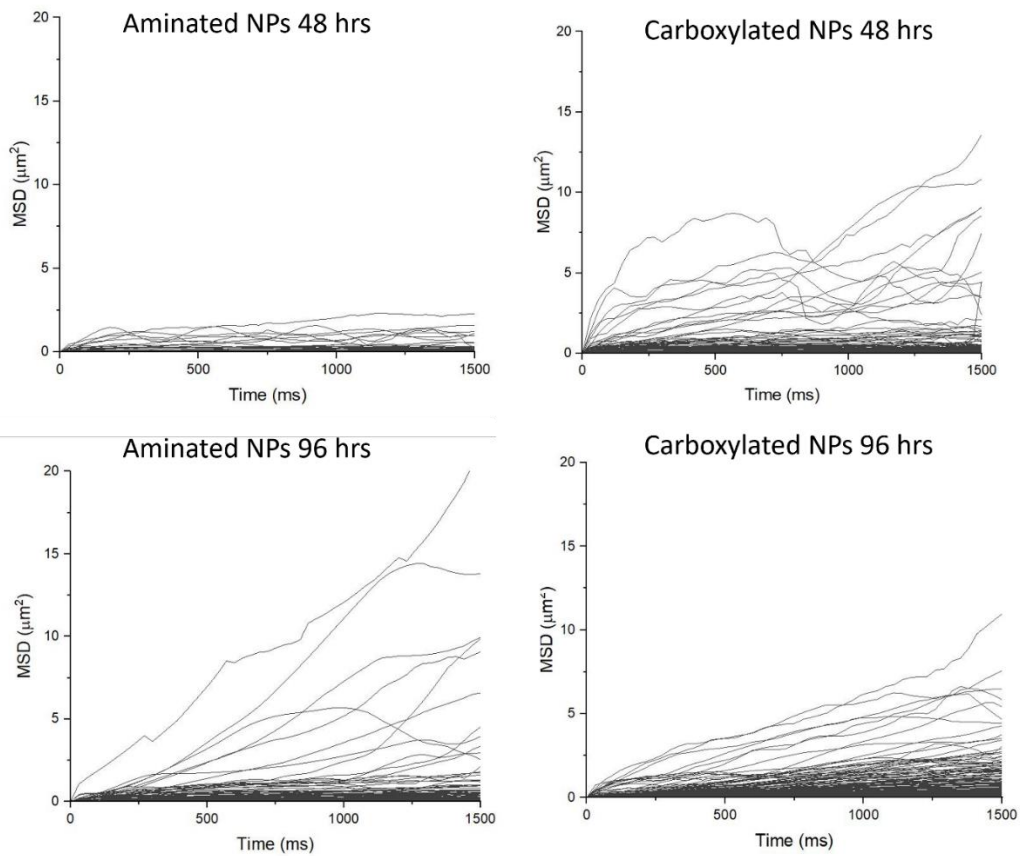


Figure 5.7: The graphs show the Mean Square Displacement (MSD) in time obtained from the SPT analysis from Experiment 1 biofilm samples. All three fields of view were plotted in the same graph for each nanoparticle considered in this study and the z depth was $4500 \pm 703 \mu\text{m}$.

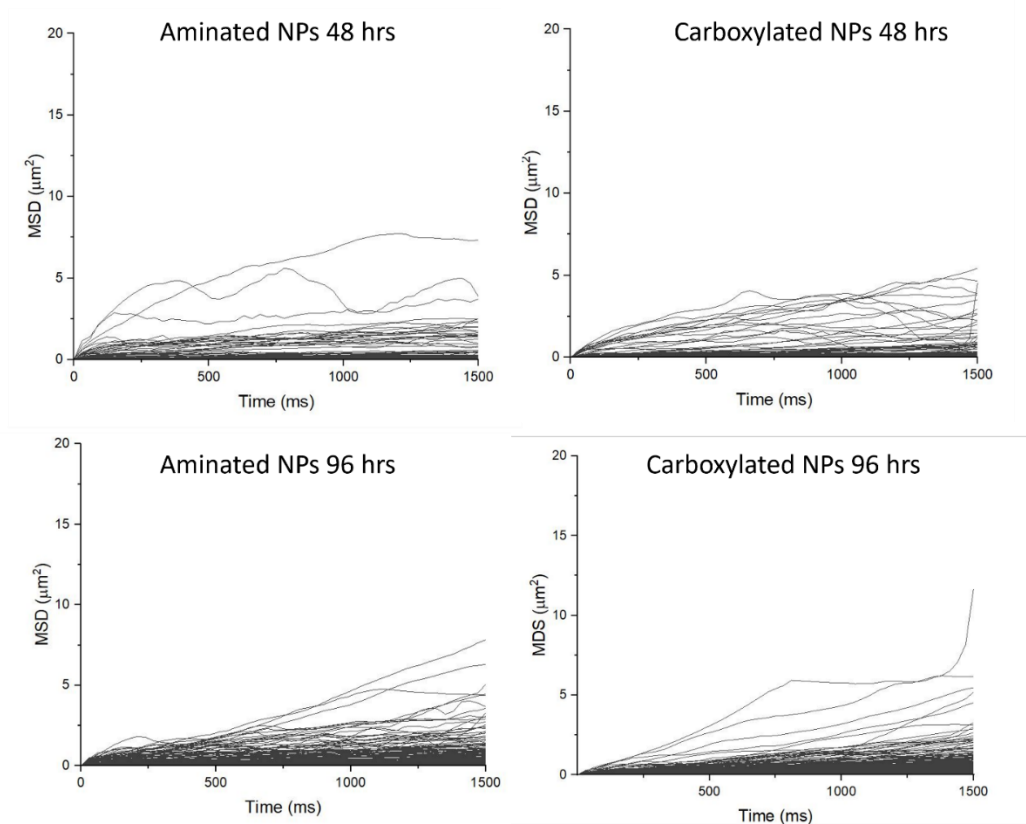


Figure 5.8: The graphs show the Mean Square Displacement (MSD) in time obtained from the SPT analysis from Experiment 2 biofilm samples. All three fields of view were plotted in the same graph for each nanoparticle considered in this study and the z depth was $4500 \pm 703 \mu\text{m}$.

Peulen & Wilkinson, (2011), concluded that considering only biofilm viscosity and tortuosity is enough to accurately describe the diffusion of NPs in biofilms. As mentioned before, if NPs get attached to cells or other biofilms components it is possible that the dynamic movement of these components can alter the diffusion of the NP and decrease the D of the NPs. In terms of the EPS architecture, the NPs may be able to reach areas of the biofilm that a particle at the bacterial size ($> 500 \text{ nm}$) would not be able to reach (See results from Chapter 3). In this study, the tracks of NP motion were obtained from the SPT analysis and are presented in polar graph in Figure 5.9 and 5.10. The tracks for the

aminated NPs in the 48 hr biofilm samples are short and thick while in the 96 hr biofilms the tracks are longer, and all the tracks seems to have similar twisting patters. In the case of the carboxylated NPs, in 48 hr biofilm samples the tracks are longer and non-directional, but in the 96 hr samples the tracks are shorter, thicker and have a variety of patterns. A twisting pattern have been previously identified in holographic 3D tracking of *P. aeruginosa* cells swimming behaviors (Vater et al., 2014). To elucidate how the movement of the NPs that can bind to cells might be affected by cellular movement, further experiments (for example tracking fluorescently labeled bacteria) that allow direct comparisons between cell and fluorescent particle motion would be useful.

The correlation methods are based on fluctuations in the fluorescence intensity, which mean that particles must be moving to be considered in the analysis. However, SPT accounts for all the particles with the fluorescent intensity inside the selected threshold including the particles that are moving and the ones that are not moving or barely moving. For this reason, SPT is an appropriate method to characterize the net behavior of nanoparticles with high spatial resolution in heterogeneous samples like biofilms, but only in samples where the particle density allows the localization of individual NPs.

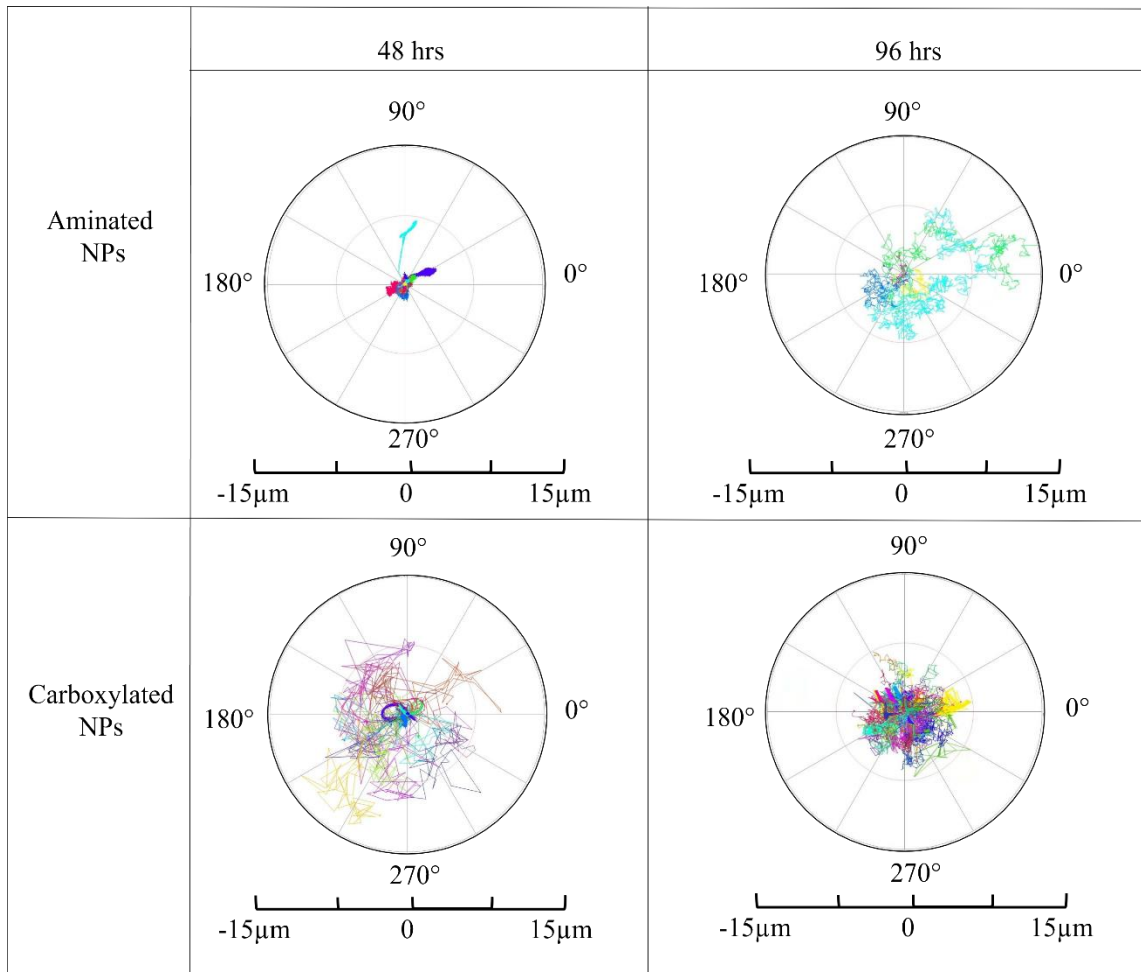


Figure 5.9: Polar graphs of individual tracks (from SPT) for all three fields of view from Experiment 1 biofilms at a z depth of $4500 \pm 703 \mu\text{m}$. Each track has an assigned color that represents a single nanoparticle with the origin representing the nanoparticle initial position. All the nanoparticle tracks for the three fields of view are presented in the polar graph for each nanoparticle considered.

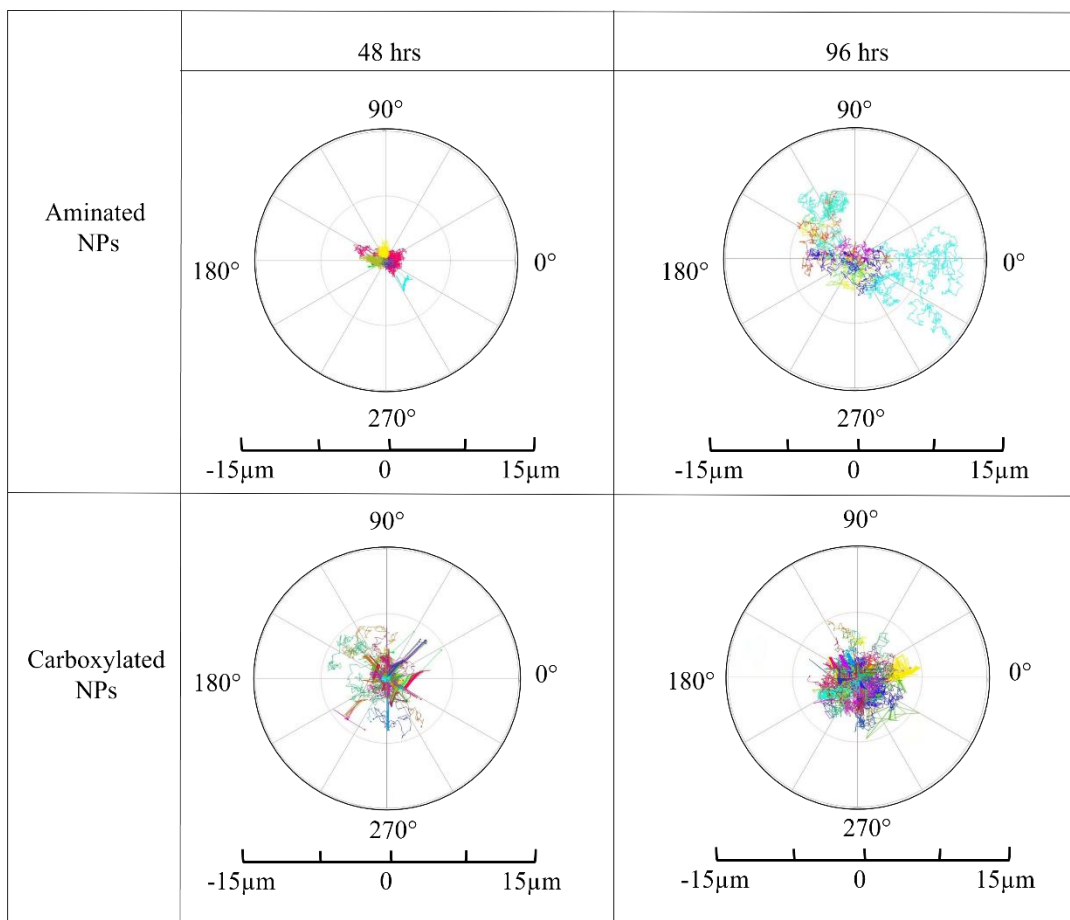


Figure 5.10: Polar graphs of individual tracks (from SPT) of all three fields of view from Experiment 2 biofilms at a z depth of $4500 \pm 703 \mu\text{m}$. Each track has an assigned color that represents a single nanoparticle with the origin representing the nanoparticle initial position. All the nanoparticle tracks for the three fields of view are presented in the polar graph for each nanoparticle considered.

5.4 Conclusion

In this study we have characterized the diffusion of aminated and carboxylated polystyrene nanoparticles as a function of *P. aeruginosa* biofilm maturity and the results from this study provide a deeper knowledge of how the interactions of the particles with biofilm components can affect the diffusion of NPs in natural biofilms. The diffusion of NPs in biofilms depends on the NP chemical composition and also on the properties of

the biofilm that depend on biofilm maturity (age). The aminated NPs have lower diffusion coefficients in 48 hr biofilms compared to carboxylated NPs, while in more mature biofilms the diffusion coefficients did not depend on the particle charge. The diffusion of both types of NPs could be influenced by electrostatic interactions between the carboxylated or aminated NPs and biofilm components. However, the particle charge doesn't affect the types (in terms of shape and size) of areas the particle can access as suggested by similarities in the connectivity maps in the biofilm samples. The NP diffusion modes changed as a function of biofilm maturity and particle functional group. The aminated and carboxylated NPs partial confinement areas increased in the 96 hr biofilm when compared to the 48 hr biofilms, but in the case of the confinement areas, they increased for the carboxylated NPs but decreased for the aminated ones. In terms of diffusion coefficients, there were no statistical difference between the D distributions from Experiment 1 and 2. The use of distributions instead of average values to characterize NP diffusion and compare biofilm replicates will help to illuminate the intrinsic heterogeneity (microdomains) of the biofilm matrix. However, NP diffusion modes were affected by variability that biofilms can have even when formed in similar conditions and by the same microorganism.

CHAPTER 6

CONCLUSIONS

The fate and transport of nanoparticles (NPs) in the environment is hard to predict due to the highly variable environmental conditions and the long list of unique properties and composition that NPs can exhibit. When nanoparticles meet biofilms, they first deposit and accumulate in the matrix and then they diffuse through the extracellular polymeric substances (EPS) matrix if the conditions are favorable. This research highlights the importance of the biofilm matrix properties in evaluating and predicting NP transport leads to a better understanding of the natural spatial heterogeneity of the EPS, how local structural micro-domains affect the mobility of NPs in biofilms and provides a window into the complex interplay between nanoparticles, microbial transcription, and biofilm architecture.

In heterogeneous matrices like biofilms, the degree of cross-linking (DCL) of the EPS components and the NP size can limit the accumulation of NPs, depending on the size of the particle relative to the void space of the matrix. A higher DCL will reduce the interstitial space between the EPS polymer chains limiting the concentration of NPs that can get into the matrix. Another factor that can influence NP deposition in biofilms is the electrostatic interactions which are influenced by the free functional groups of the polymeric matrix and the surrounding bulk solution chemistry. A low DCL will result in polysaccharides with a higher concentration of free functional groups, resulting in an increase in NP deposition if electrostatic forces are favorable. The favorable or

unfavorable electrostatic forces will highly depend on the surrounding bulk solution chemistry which affect polysaccharide and NPs properties, like the surface charge. Biofilms are ubiquitous in nature in where the concentration of biofilm cross-linking agents such as calcium and other EPS component with cross-linking, will vary depending on the conditions of the system, which mean that EPS DCL controlled by the nature of the surrounding bulk solution chemistry could influence the deposition of NPs in biofilms. Also, due to the interactions between EPS components (proteins, nucleic acids, lipids and polysaccharides) the DCL can affect the viscosity, pseudoplasticity and elasticity of the matrix and restrict NP mobility. These results suggest, that the DCL of the EPS biofilm matrix could be manipulated to increase or decrease the deposition of NPs into the biofilm taking in consideration also the NP physicochemical properties (e.g., surface chemistry, charge and size).

After NP deposition into the biofilm matrix the average diffusion coefficient of NPs will increase as the NP size decrease. However, a simple inverse trend between NP size and diffusion coefficient cannot be inferred. The scale of the accessible area for diffusion relative to the NP size is important and could influence modes of diffusion which cannot be assumed to be isotropic. Real biofilms are dynamic and active with responsive interchange between the microbial inhabitants and the biofilm structure, and the mobility of nanoparticles will be dictated by the physicochemical properties of the particle but also the time and environment dependent biofilm properties. NP diffusion modes can be affected by the variability that biofilms can have even when formed in similar conditions and by the same microorganism. However, the use of distributions instead of average values to characterize NP diffusion and compare biofilm replicates could help to

illuminate the intrinsic heterogeneity (microdomains) of the biofilm matrix and can provide experimental data to develop mathematical biofilm models that consider the variable diffusivity modes of solutes within biofilms. In addition, in the results obtained in this study, all sizes of particles under study experienced a degree of confinement and partial confinement. Therefore, diffusion in heterogeneous matrices (like alginate) cannot be assumed to be isotropic. Different modes of diffusion should be taken into consideration in biofilm modeling including confinement and partial confinement which could help to characterize better the movement of particles in heterogeneous matrices.

When nanoparticles accumulate in biofilms, their presence can be a stressor to the cells and can affect the expression of genes related to extracellular polymeric substances production and quorum sensing systems. Depending on NP surface charge, gene function and biofilm age, even simple polystyrene NPs can be stressors for bacterial cells and lead to changes in the production of polysaccharides and quorum sensing signals which could end up affecting biofilm architecture and metabolic efficiency. Further studies are needed to identify the mechanisms and processes behind the behaviors identified in this study after the PAO1 $\Delta wspF \Delta psl P_{BAD}pel$ exposure to polystyrene NPs and to quantify the effects in the biofilm properties due the down and upregulation of genes caused by the NP presence, which could help to identify the consequences of the results presented. To understand the complex system of biofilms, it would be useful to know the quantity of basic biofilm components (e.g., number of viable cells (CFU) and concentration of EPS components), the spatial distribution of cells and the 3 dimensional characteristics of biofilm architecture (Kassing & Hoek, 2020). An increase in polysaccharide

concentration could increase the DCL between EPS components which may restrict diffusion processes in the matrix while a decrease in polysaccharide production due to the presence of polystyrene NPs could prohibit biofilm development and increase bacteria susceptibility to unfavorable conditions or antibiotics.

In general, biofilms are complex matrices that due to their intrinsic heterogeneity and dynamic and active responses to environmental changes increase the complexity of studies related with NPs accumulation and transport in biofilms. It is hard to generalize the behavior of NPs in biofilms because the environmental conditions, the EPS physicochemical properties, the bacterial metabolic capabilities, and the NPs properties, all play a role in the NP-biofilm interactions, which should all be taken in consideration when evaluating NPs-biofilm interactions.

APPENDIX A

RAW TIRF MICROSCOPY IMAGES FROM CHAPTER 3

This appendix is a compilation of the raw TIRF microscopy images for each particle size considered in the study presented in Chapter 3 about the heterogeneous diffusion of polystyrene nanoparticles through an alginate matrix cross-linked with calcium ions.

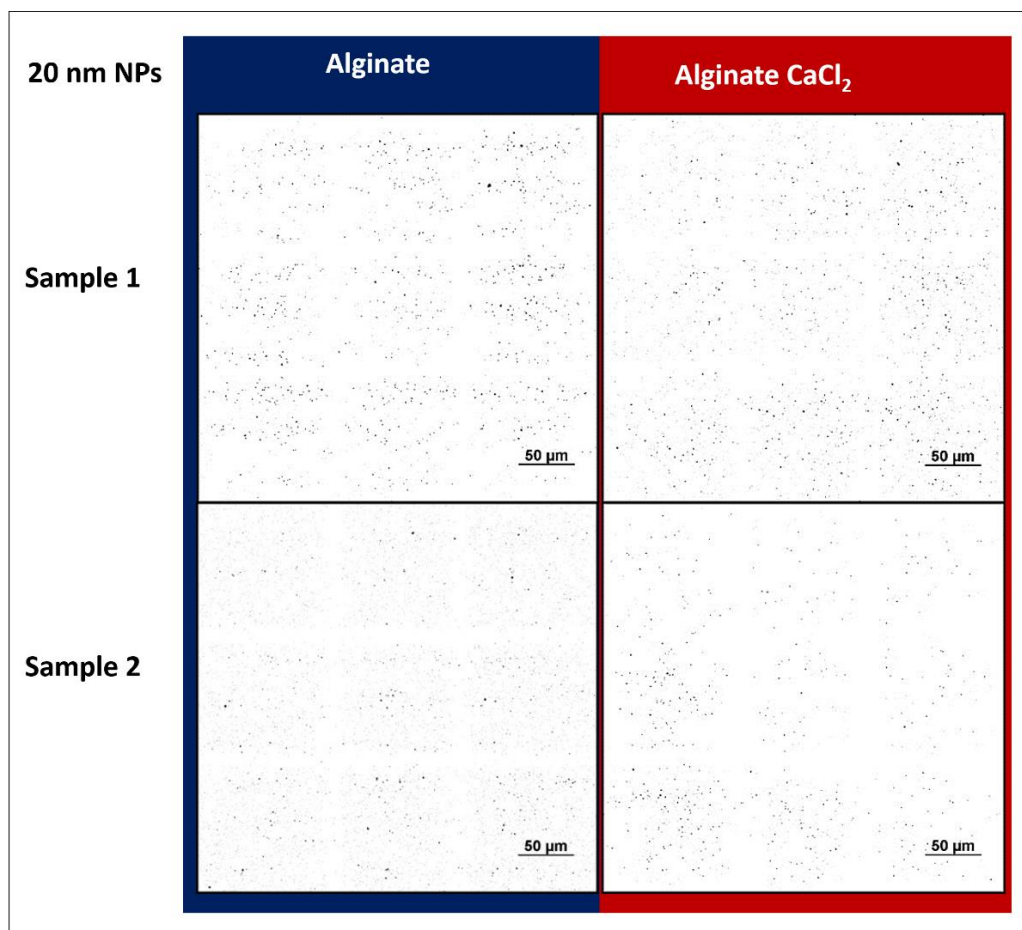


Figure A.1: Images of the 20 nm particles from two independent samples. 80% of the total area of each sample was used for the particle count. The images were color inverted for visualization purposes, but the analysis was done with the images in their original colors (white particles and black background). The scale bar is 50 μm.

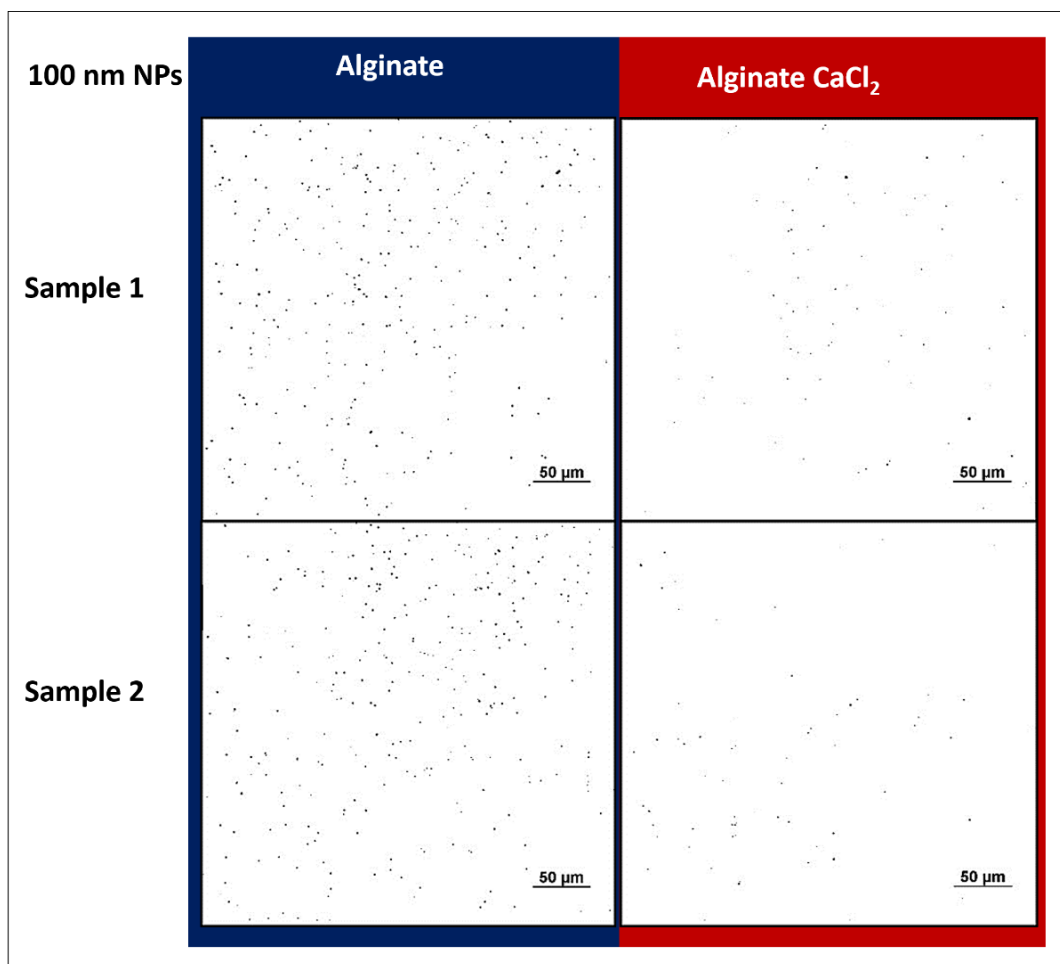


Figure A.2: Images of the 100 nm particles from two independent samples. 80% of the total area of each sample was used for the particle count. The images were color inverted for visualization purposes, but the analysis was done with the images in their original colors (white particles and black background). The scale bar is 50 μm .

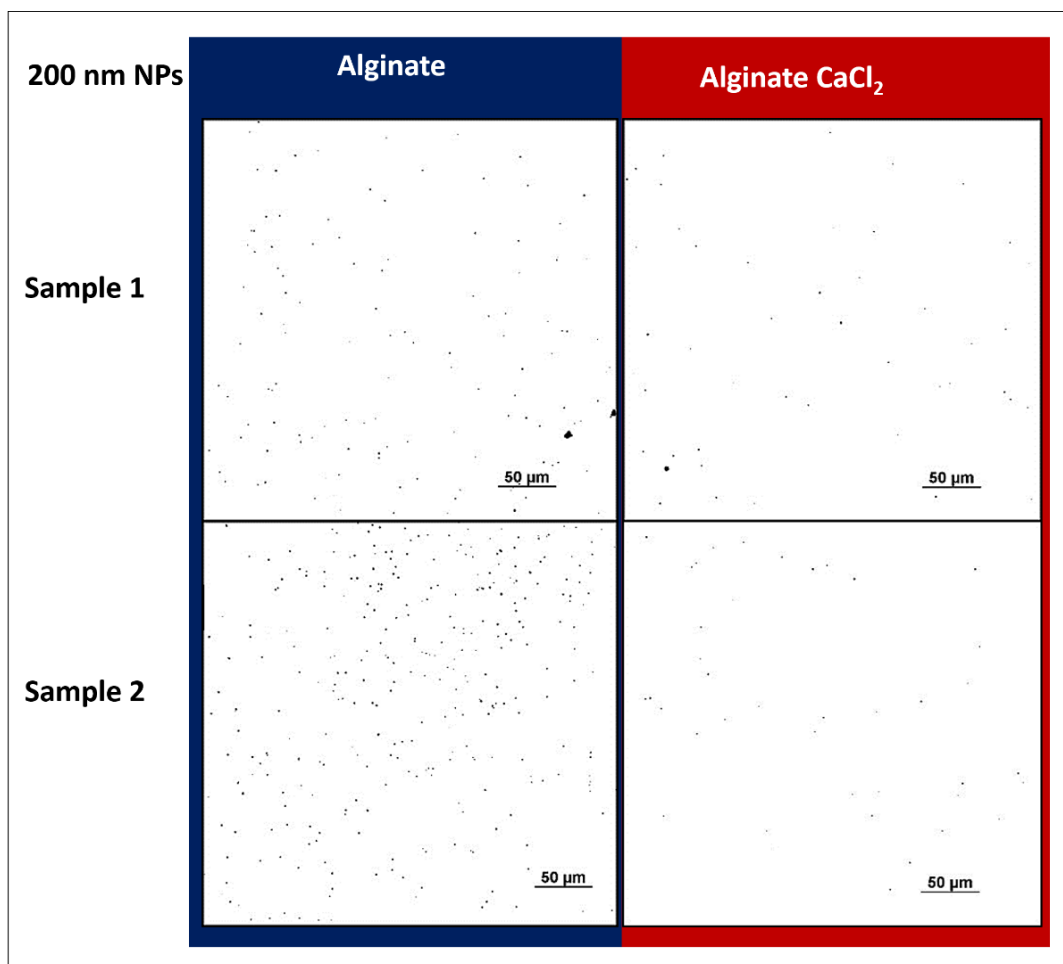


Figure A.3: Images of the 200 nm particles from two independent samples. 80% of the total area of each sample was used for the particle count. The images were color inverted for visualization purposes, but the analysis was done with the images in their original colors (white particles and black background). The scale bar is 50 μm .

APPENDIX B

FLOW CELLS DESIGN

The flow cells chambers used for this study were custom designed, and 3D printed in order to observe the samples under the microscope without disturbing the biofilms' structure. In this appendix we included 2D and 3D schematics with the specific dimensions of the design (Figures B.1, B.2, B.3 and B.4). The flow cells were made of the polymer PA 2200, the external side stainless-steel tube has a diameter of 3 mm (outer diameter) and the screws to attach the top part with the bottom are the 3/8 inches pan head Phillips style #4 made of aluminum. The flow cell chambers were closed with glass cover slips of 0.17 mm thickness with dimensions of 22 mm x 22 mm. To prevent media leaks and the contamination of the pure culture inside the flow cell chambers, a silicon sheet was placed in between the top and bottom part of the flow cell and then the flow cells were sealed with a clear waterproof silicone sealant.

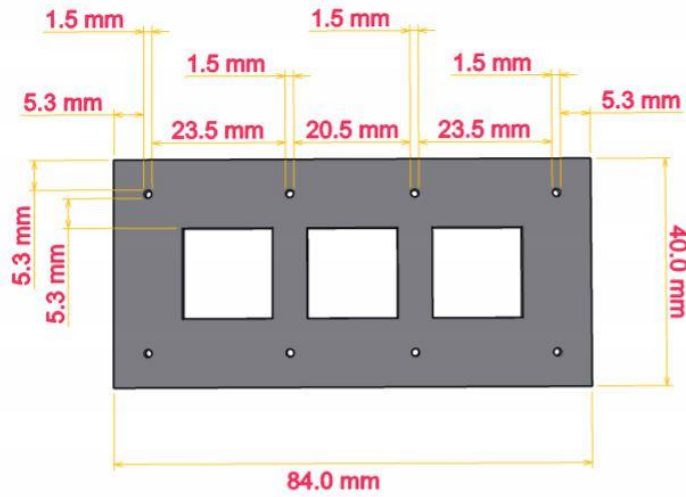


Figure B.1: 2D Schematic with the specific dimensions of the flow cells lid. In the Phillips style #4 of 3/8 inches screws were 1.5 mm drilled holes the Phillips style #4 of 3/8 inches screws were screwed to close the flow cell.

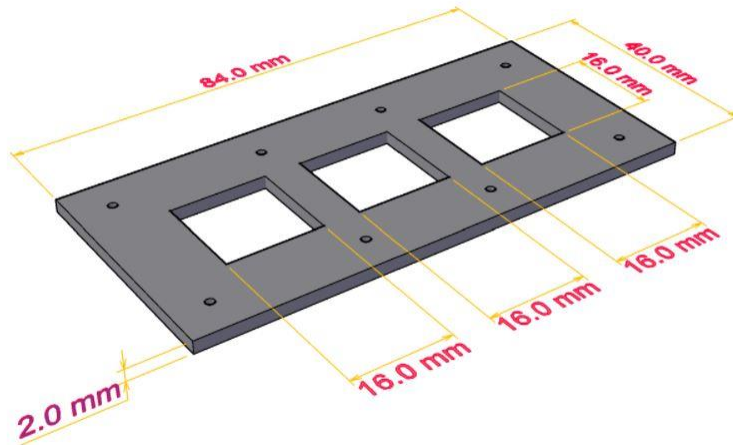


Figure B.2: 3D Schematic with the specific dimensions of the flow cells lid. The 22 X 22 cover glass slide were glued over the 16.0 mm squares to seal the flow cell chamber but at the same time allow microscopic visualization.

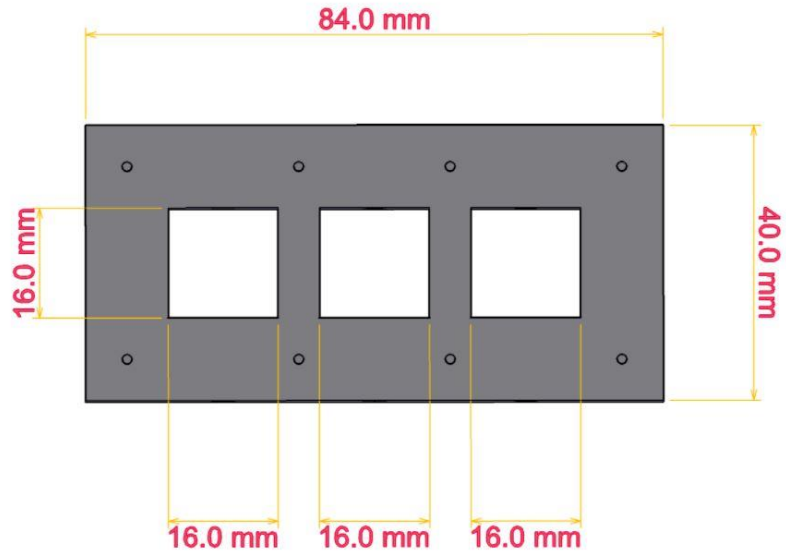


Figure B.3: 2D Schematic with the specific dimensions of the flow cells bottom. The 22 X 22 cover glass slide were glued over the 16.0 mm squares to seal the flow cell chamber but at the same time allow microscopic visualization.

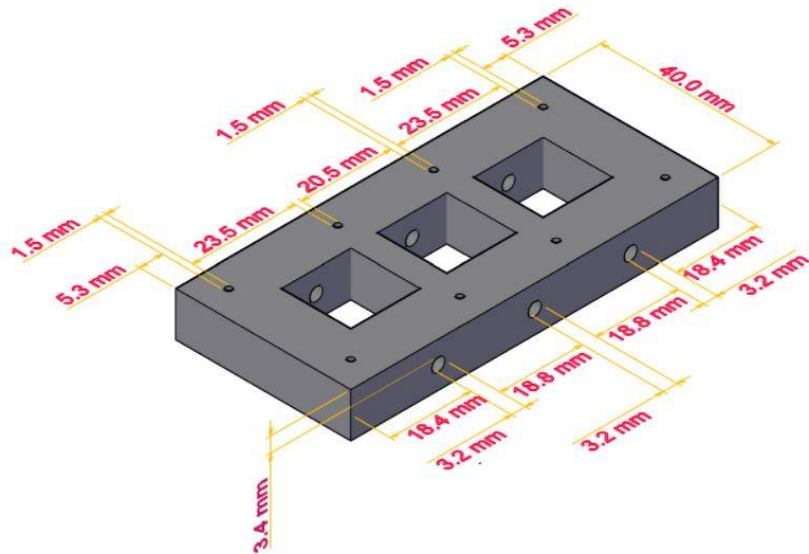


Figure B.4: 3D Schematic with the specific dimensions of the flow cells bottom. In the 3/8 inches Phillips style #4 screws were 1.5 mm holes to close the flow cell. The silicone tubing was connected to the external side stainless-steel tube (OD= 3.2 mm, ID= 3.0 mm) that was glued to the 3.2 mm side holes

APPENDIX C

STATISTICAL ANALYSIS OF DIFFUSION COEFFICIENT DISTRIBUTIONS

This appendix contains the R code used for identifying statistical differences between the diffusion coefficient distributions in Chapter 3 and Chapter 5. The codes used the packages *base*, *datasets*, *graphics*, *grDevices*, *methods*, *stats* and *utils*. The analysis is based on the permutation test of symmetry where the levels of the various conditions were treated as having paired or repeated data. The code was written by Daveed Goldenberg from the Statistical Consulting group at UMass Amherst.

```
1 ---
2 title: "R Notebook"
3 output: html_notebook
4 ```{r}
5 data_file_name_here <- read.csv('newdata.csv', header = T)
6 ```
7 ```{r}
8 data_file_name_here <- data_file_name_here [-c(931,932,933,934),]
9 ```{r}
10 Function_to_use <- function(a,b){
11   N1 <- length(a[!is.na(a)])
12   N2 <- length(b[!is.na(b)])
13   avgdist <- replicate(100000, {
14     all <- sample(c(a[!is.na(a)], b[!is.na(b)] ))
15     new1 <- all[1:N1]
16     new2 <- all[(N1 + 1): N2]
17     return(mean(new1, na.rm = T) - mean(new2, na.rm = T))
18   })
19   hist(avgdist)
20   obs <- mean(b, na.rm = T) - mean(a, na.rm = T)
21   abline(v = obs, col = 'red', lwd=2)
22   p.value <- (sum(abs(avgdist) > abs(obs)) + 1) / (length(avgdist) + 1)
23   return(p.value)
24 }
25 ```{r}
26 function_to_use(data_file_name_here $col1name, data_file_name_here $col2name)
```

BIBLIOGRAPHY

- Allesen-Holm, M., Barken, K. B., Yang, L., Klausen, M., Webb, J. S., Kjelleberg, S., Tolker-Nielsen, T. (2006). A characterization of DNA release in *Pseudomonas aeruginosa* cultures and biofilms. *Molecular Microbiology*, *59*(4), 1114–1128.
- Amsden, B. (1999). An Obstruction-Scaling Model for Diffusion in Homogeneous Hydrogels. *Macromolecules*, *32*(3), 874–879.
- Avellan, A., Simonin, M., McGivney, E., Bossa, N., Spielman-Sun, E., Rocca, J. D., Lowry, G. V. (2018). Gold nanoparticle biodissolution by a freshwater macrophyte and its associated microbiome. *Nature Nanotechnology*, *13*(11), 1072.
- Babayekhorasani, F., Dunstan, D. E., Krishnamoorti, R., & Conrad, J. C. (2016). Nanoparticle diffusion in crowded and confined media. *Soft Matter*, *12*(40), 8407–8416.
- Banerjee, D., & Sengupta, S. (2011). Chapter 12 - Nanoparticles in Cancer Chemotherapy. In A. B. T.-P. in M. B. and T. S. Villaverde (Ed.), *Nanoparticles in Translational Science and Medicine* (Vol. 104, pp. 489–507).
- Battin, T. J., Kammer, F. v. d., Weilhartner, A., Ottofuelling, S., & Hofmann, T. (2009). Nanostructured TiO₂: Transport Behavior and Effects on Aquatic Microbial Communities under Environmental Conditions. *Environmental Science & Technology*, *43*(21), 8098–8104.
- Beech, I. B. (2004). Corrosion of technical materials in the presence of biofilms - current understanding and state-of-the art methods of study. *International Biodeterioration & Biodegradation*, *53*(3), 177–183.
- Benigar, E., Zupančič Valant, A., Dogsa, I., Sretenovic, S., Stopar, D., Jamnik, A., & Tomšič, M. (2016). Structure and Dynamics of a Model Polymer Mixture Mimicking a Levan-Based Bacterial Biofilm of *Bacillus subtilis*. *Langmuir*, *32*(32), 8182–8194.
- Billingsley, M. M., Riley, R. S., & Day, E. S. (2017). Antibody-nanoparticle conjugates to enhance the sensitivity of ELISA-based detection methods. *PLOS ONE*, *12*(5), e0177592.
- Birjiniuk, A., Billings, N., Nance, E., Hanes, J., Ribbeck, K., & Doyle, P. S. (2014). Single particle tracking reveals spatial and dynamic organization of the *Escherichia coli* biofilm matrix. *New Journal of Physics*, *16*, 1–13.

- Braccini, I., & Pérez, S. (2001). Molecular Basis of Ca²⁺ Induced Gelation in Alginates and Pectins: The Egg-Box Model Revisited. *Biomacromolecules*, 2(4), 1089–1096.
- Brown, A. N., Smith, K., Samuels, T. A., Lu, J., Obare, S. O., & Scott, M. E. (2012). Nanoparticles functionalized with ampicillin destroy multiple-antibiotic-resistant isolates of *Pseudomonas aeruginosa* and *Enterobacter aerogenes* and methicillin-resistant *Staphylococcus aureus*. *Applied and Environmental Microbiology*, 78(8), 2768–2774.
- Bundschuh, M., Filser, J., Lüderwald, S., Mckee, M. S., Metreveli, G., Schaumann, G. E., Wagner, S. (2018). Nanoparticles in the environment : where do we come from , where do we go to ? *Environmental Sciences Europe*, 30(6), 1–17.
- Cai, L., Panyukov, S., & Rubinstein, M. (2011). Mobility of Nonsticky Nanoparticles in Polymer Liquids. *Macromolecules*, 44, 7853–7863.
- Cheng, N.-S. (2008). Formula for the Viscosity of a Glycerol–Water Mixture. *Industrial & Engineering Chemistry Research*, 47(9), 3285–3288.
- Choi, J. H., Kim, S. O., Linardy, E., Dreaden, E. C., Zhdanov, V. P., Hammond, P. T., & Cho, N. J. (2015). Influence of pH and Surface Chemistry on Poly(l -lysine) Adsorption onto Solid Supports Investigated by Quartz Crystal Microbalance with Dissipation Monitoring. *Journal of Physical Chemistry B*, 119(33), 10554–10565.
- Chompoosor, A., Saha, K., Ghosh, P. S., Macarthy, D. J., Miranda, O. R., Zhu, Z.-J., Rotello, V. M. (2010). The role of surface functionality on acute cytotoxicity, ROS generation and DNA damage by cationic gold nanoparticles. *Small (Weinheim an Der Bergstrasse, Germany)*, 6(20), 2246–2249.
- Colvin, K. M., Alnabelseya, N., Baker, P., Whitney, J. C., Lynne Howell, P., & Parsek, M. R. (2013). PelA deacetylase activity is required for pel polysaccharide synthesis in *Pseudomonas aeruginosa*. *Journal of Bacteriology*, 195(10), 2329–2339.
- Colvin, K. M., Gordon, V. D., Murakami, K., Borlee, B. R., Wozniak, D. J., Wong, G. C. L., & Parsek, M. R. (2011). The pel polysaccharide can serve a structural and protective role in the biofilm matrix of *Pseudomonas aeruginosa*. *PLoS Pathogens*, 7(1), e1001264.
- Colvin, K. M., Irie, Y., Tart, C. S., Urbano, R., Whitney, J. C., Ryder, C., Parsek, M. R. (2012a). The Pel and Psl polysaccharides provide *Pseudomonas aeruginosa* structural redundancy within the biofilm matrix. *Environmental Microbiology*, 14(8), 1913–1928.

- Colvin, K. M., Irie, Y., Tart, C. S., Urbano, R., Whitney, J. C., Ryder, C., Parsek, M. R. (2012b). The Pel and Psl polysaccharides provide *Pseudomonas aeruginosa* structural redundancy within the biofilm matrix. *Environmental Microbiology*, *14*(8), 1913–1928.
- Conrad, J. C., & Poling-Skutvik, R. (2018). Confined Flow: Consequences and Implications for Bacteria and Biofilms. *Annual Review of Chemical and Biomolecular Engineering*, *9*(1), 175–200.
- Crocker, J. C., & Grier, D. G. (1996). Methods of Digital Video Microscopy for Colloidal Studies. *Journal of Colloid and Interface Science*, *179*(1), 298–310.
- Dale, A. L., Casman, E. A., Lowry, G. V, Lead, J. R., Viparelli, E., & Baalousha, M. (2015). Modeling Nanomaterial Environmental Fate in Aquatic Systems. *Environmental Science & Technology*, *49*, 2587–2593.
- Davey, R. J., Digman, M. A., Gratton, E., & Moens, P. D. J. (2018). Quantitative image mean squared displacement (iMSD) analysis of the dynamics of profilin 1 at the membrane of live cells. *Methods*, *140–141*, 119–125.
- De Kerchove, A. J., & Elimelech, M. (2006). Structural growth and viscoelastic properties of adsorbed alginate layers in monovalent and divalent salts. *Macromolecules*, *39*(19), 6558–6564.
- Decho, A. W. (1990). Microbial exopolymer secretions in ocean environments - their role(s) in food webs and marine processes. *Oceanography and Marine Biology*, *28*, 73–153.
- Derveaux, S., Vandesomepele, J., & Hellemans, J. (2010). How to do successful gene expression analysis using real-time PCR. *Methods*, *50*(4), 227–230.
- Desmau, M., Carboni, A., Bars, M. Le, Doelsch, E., Benedetti, M. F., Auffan, M., Gelabert, A. (2020). *How Microbial Biofilms Control the Environmental Fate of Engineered Nanoparticles ?* *8*(July), 1–20.
- Devaraj, A., Buzzo, J. R., Mashburn-Warren, L., Gloag, E. S., Novotny, L. A., Stoodley, P., Goodman, S. D. (2019). The extracellular DNA lattice of bacterial biofilms is structurally related to Holliday junction recombination intermediates. *Proceedings of the National Academy of Sciences*, *116*(50), 25068 LP – 25077.
- Di Rienzo, C., Gratton, E., Beltram, F., & Cardarelli, F. (2013). Fast spatiotemporal correlation spectroscopy to determine protein lateral diffusion laws in live cell membranes. *Proceedings of the National Academy of Sciences*, *110*(30), 12307–12312.

- Digiaco, L., Digman, M. A., Gratton, E., & Caracciolo, G. (2016). Development of an image Mean Square Displacement (iMSD)-based method as a novel approach to study the intracellular trafficking of nanoparticles. *Acta Biomaterialia*, *42*, 189–198.
- Digman, M. A., & Gratton, E. (2009). Imaging barriers to diffusion by pair correlation functions. *Biophysical Journal*, *97*(2), 665–673.
- Dixon, M. C. (2008). Quartz Crystal Microbalance with Dissipation Monitoring : Enabling Real-Time Characterization of Biological Materials and Their Interactions. *Journal of Biomolecular Techniques*, *19*, 151–158.
- Ehrenberg, M., & Rigler, R. (1974). Rotational brownian motion and fluorescence intensify fluctuations. *Chemical Physics*, *4*(3), 390–401.
- El Mansouri, N.-E., & Salvadó, J. (2007). Analytical methods for determining functional groups in various technical lignins. *Industrial Crops and Products*, *26*(2), 116–124.
- Erdim, E., Badireddy, A. R., & Wiesner, M. R. (2015). Characterizing reactive oxygen generation and bacterial inactivation by a zerovalent iron-fullerene nano-composite device at neutral pH under UV-A illumination. *Journal of Hazardous Materials*, *283*, 80–88.
- Ferry, J., Craig, P., Hexel, C., Sisco, P., Frey, R., Pennington, P., J Shaw, T. (2009). Transfer of gold nanoparticles from the water column to the estuarine food web. In *Nature nanotechnology* (Vol. 4).
- Flemming, H. C., Wingender, J., Szewzyk, U., Steinberg, P., Rice, S. A., Kjelleberg, S. (2016). Biofilms: an emergent form of bacterial life. *Nature Reviews Microbiology*, *14*(9), 563–575.
- Flemming, H. C., & Wingender, J. (2010). The biofilm matrix. *Nature Reviews Microbiology*, *8*(9), 623–633.
- Friedman, L., & Kolter, R. (2004). Genes involved in matrix formation in *Pseudomonas aeruginosa* PA14 biofilms. *Molecular Microbiology*, *51*(3), 675–690.
- Fulaz, S., Vitale, S., Quinn, L., & Casey, E. (2019). Nanoparticle – Biofilm Interactions : The Role of the EPS Matrix. *Trends in Microbiology*, *27*(11), 915–926.
- Georgiades, P., Pudney, P. D. A., Thornton, D. J., & Waigh, T. A. (2013). Particle Tracking Microrheology of Purified Gastrointestinal Mucins. *Biopolymers*, *101*(4), 366–377.

- Giese, B., Klaessig, F., Park, B., Kaegi, R., Steinfeldt, M., Wigger, H., Gottschalk, F. (2018). Risks, Release and Concentrations of Engineered Nanomaterial in the Environment. *Scientific Reports*, 8(1), 1–18. Retrieved from
- Glupczynski, Y. (1999). Minireview Aminoglycosides : Activity and Resistance. *Antimicrobial Agents and Chemotherapy*, 43(4), 727–737.
- Golmohamadi, M., Clark, R. J., Veinot, J. G. C., & Wilkinson, K. J. (2013). The role of charge on the diffusion of solutes and nanoparticles (silicon nanocrystals, nTiO₂, nAu) in a biofilm. *Environmental Chemistry*, 10(1), 34–41.
- Guibal, E. (2004). Interactions of metal ions with chitosan-based sorbents: a review. *Separation and Purification Technology*, 38, 43–74.
- Hansing, J., Ciemer, C., Kim, W. K., Zhang, X., Derouchey, J. E., & Netz, R. R. (2016). Nanoparticle filtering in charged hydrogels: Effects of particle size, charge asymmetry and salt concentration. *The European Physical Journal E*, 39(53), 1–13.
- Hansing, J., Duke, J. R., Fryman, E. B., Derouchey, J. E., & Netz, R. R. (2018). Particle Diffusion in Polymeric Hydrogels with Mixed Attractive and Repulsive Interactions [Rapid-communication]. *Nano Letters*, 18, 5248–5256.
- Hebert, B., Costantino, S., & Wiseman, P. W. (2005). Spatiotemporal image correlation spectroscopy (STICS) theory, verification, and application to protein velocity mapping in living CHO cells. *Biophysical Journal*, 88(5), 3601–3614.
- Hessler, C. M., Wu, M.-Y., Xue, Z., Choi, H., & Seo, Y. (2012). The influence of capsular extracellular polymeric substances on the interaction between TiO₂ nanoparticles and planktonic bacteria. *Water Research*, 46(15), 4687–4696.
- Hildebrand, F., Cornelis, P., Charlier, D., Hassett, D., & Ha, S. (2012). Global regulation of gene expression by OxyR in an important human opportunistic pathogen. *Nucleic Acids Research*, 40(10), 4320–4333.
- Hochella, M. F., Spencer, M. G., & Jones, K. L. (2015). Nanotechnology: nature’s gift or scientists’ brainchild? *Environmental Science: Nano*, 2(2), 114–119.
- Höök, F., Kasemo, B., Nylander, T., Fant, C., Sott, K., & Elwing, H. (2001). Variations in Coupled Water, Viscoelastic Properties, and Film Thickness of a Mefp-1 Protein Film during Adsorption and Cross-Linking: A Quartz Crystal Microbalance with Dissipation Monitoring, Ellipsometry, and Surface Plasmon Resonance Study. *Analytical Chemistry*, 73(24), 5796–5804.

- Ikuma, K., & Lau, B. L. T. (2013). Water constituents that affect the performance of nanomaterials. In *Future Science Book Series. Applications of Nanomaterials for Water Quality* (pp. 86–98).
- Ikuma, K., Madden, A. S., Decho, A. W., & Lau, B. L. T. (2014). Deposition of nanoparticles onto polysaccharide-coated surfaces: implications for nanoparticle–biofilm interactions. *Environmental Science: Nano*, *1*(2), 117–122.
- Ilk, S., Sağlam, N., Özgen, M., & Korkusuz, F. (2017). Chitosan nanoparticles enhances the anti-quorum sensing activity of kaempferol. *International Journal of Biological Macromolecules*, *94*, 653–662.
- Jaqaman, K., Loerke, D., Mettlen, M., Kuwata, H., Schmid, S. L., & Danuser, G. (2009). Robust single particle tracking in live cell time-lapse sequences. *Nat Methods*, *5*(8), 695–702.
- Jennings, L. K., Storek, K. M., Ledvina, H. E., Coulon, C., Marmont, L. S., Sadovskaya, I., Parsek, M. R. (2015). Pel is a cationic exopolysaccharide that cross-links extracellular DNA in the *Pseudomonas aeruginosa* biofilm matrix. *Proceedings of the National Academy of Sciences*, *112*(36), 11353–11358.
- K. Y. Lee, D. J. M. (2012). Alginate : properties and biomedical applications. *Progress in Polymer Science (Oxford)*, *37*(1), 106–126.
- Kaplan, J. B. (2010). Biofilm Dispersal : Mechanisms, Clinical Implications, and Potential Therapeutic Uses. *J Dent Res.*, *89*(3), 205–218.
- Kassinger, S. J., & Hoek, M. L. Van. (2020). Biofilm architecture : An emerging synthetic biology target. *Synthetic and Systems Biotechnology*, *5*, 1–10.
- Khan, I., Saeed, K., & Khan, I. (2019). Nanoparticles : Properties, applications and toxicities. *Arabian Journal of Chemistry*, *12*(7), 908–931.
- Kilan, K., & Warszyński, P. (2014). Thickness and permeability of multilayers containing alginate cross-linked by calcium ions. *Electrochimica Acta*, *144*, 254–262.
- Kim, B., Park, C.-S., Murayama, M., & Hochella, M. F. (2010). Discovery and Characterization of Silver Sulfide Nanoparticles in Final Sewage Sludge Products. *Environmental Science & Technology*, *44*(19), 7509–7514.
- Kim, J. I., Park, H. G., Chang, K. H., Nam, D. H., & Yeo, M. K. (2016). Trophic transfer of nano-TiO₂ in a paddy microcosm: A comparison of single-dose versus sequential multi-dose exposures. *Environmental Pollution*, *212*, 316–324.

- Kirstein, J., Platschek, B., Jung, C., Brown, R., Bein, T., & Bräuchle, C. (2007). Exploration of nanostructured channel systems with single-molecule probes. *Nature Materials*, 6(4), 303–310.
- Kisley, L., Brunetti, R., Tauzin, L. J., Shuang, B., Yi, X., Kirkemide, A. W., Landes, C. F. (2015). Characterization of Porous Materials by Fluorescence Correlation Spectroscopy Super-resolution Optical Fluctuation Imaging. *ACS Nano*, 9(9), 9158–9166.
- Kroll, A., Behra, R., Kaegi, R., & Sigg, L. (2014). Extracellular Polymeric Substances (EPS) of Freshwater Biofilms Stabilize and Modify CeO₂ and Ag Nanoparticles. *Plos One*, 9(10).
- Li, Y., Zhang, W., Niu, J., & Chen, Y. (2013). Surface-Coating-Dependent Dissolution, Aggregation, and Reactive Oxygen Species (ROS) Generation of Silver Nanoparticles under Different Irradiation Conditions. *Environmental Science & Technology*, 47(18), 10293–10301.
- Liao, Y., Yang, S. K., Koh, K., Matzger, A. J., & Biteen, J. S. (2012). Heterogeneous single-molecule diffusion in one-, two-, and three-dimensional microporous coordination polymers: Directional, trapped, and immobile guests. *Nano Letters*, 12(6), 3080–3085.
- Lieleg, Oliver; Ribbeck, K. (2011). Biological Hydrogels as Selective Diffusion Barriers. *Trends Cell Biol.*, 21(9), 543–551.
- Magde, D., Elson, E., & Webb, W. W. (1972). Thermodynamic Fluctuations in a Reacting System---Measurement by Fluorescence Correlation Spectroscopy. *Phys. Rev. Lett.*, 29(11), 705–708.
- Malacrida, L., Hedde, P. N., Ranjit, S., Cardarelli, F., & Gratton, E. (2018). Visualization of barriers and obstacles to molecular diffusion in live cells by spatial pair-cross-correlation in two dimensions. *Biomedical Optics Express*, 9(1), 303.
- Malacrida, L., Rao, E., & Gratton, E. (2018). Comparison between iMSD and 2D-pCF analysis for molecular motion studies on in vivo cells: The case of the epidermal growth factor receptor. *Methods*, 140–141, 74–84.
- Marmont, L. S., Whitfield, G. B., Rich, J. D., Yip, P., Giesbrecht, L. B., Stremick, C. A., Howell, P. L. (2017). PelA and PelB proteins form a modification and secretion complex essential for Pel polysaccharide-dependent biofilm formation in *Pseudomonas aeruginosa*. *The Journal of Biological Chemistry*, 292(47), 19411–19422.

- Matsukawa, M., & Greenberg, E. P. (2004). Putative exopolysaccharide synthesis genes influence *Pseudomonas aeruginosa* biofilm development. *Journal of Bacteriology*, *186*(14), 4449–4456.
- Mattheyses, A., Simon, S., & Z Rappoport, J. (2010). Imaging with Total Internal Reflection Fluorescence Microscopy for the Cell Biologist. *Journal of Cell Science*, *123*, 3621–2628.
- Maunder, E., & Welch, M. (2017). Matrix exopolysaccharides; the sticky side of biofilm formation. *FEMS Microbiology Letters*, *364*(13).
- McGill, S. L., Cuylear, C. L., Adolphi, N. L., Osiński, M., & Smyth, H. D. C. (2009). Enhanced drug transport through alginate biofilms using magnetic nanoparticles. *Proceedings of SPIE*, *7189*, 718918.
- Mellbye, B., & Schuster, M. (2014). Physiological framework for the regulation of quorum sensing-dependent public goods in *Pseudomonas aeruginosa*. *Journal of Bacteriology*, *196*(6), 1155–1164.
- Merakchi, A., Bettayeb, S., Drouiche, N., & Adour, L. (2019). Cross - linking and modification of sodium alginate biopolymer for dye removal in aqueous solution. *Polymer Bulletin*, *76*(7), 3535–3554.
- Miller, K. P., Wang, L., Chen, Y., Pellechia, P. J., Benicewicz, B. C., & Decho, A. W. (2015). Engineering nanoparticles to silence bacterial communication. *Frontiers in Microbiology*, *6*(March), 1–7.
- Moens, P. D. J., Digman, M. A., & Gratton, E. (2015). Modes of diffusion of cholera toxin bound to GM1 on live cell membrane by image mean square displacement analysis. *Biophysical Journal*, *108*(6), 1448–1458.
- Nakamura, S., Higashiyama, Y., Izumikawa, K., Seki, M., Takeya, H., Yamamoto, Y., ... Kohno, S. (2008). The roles of the quorum-sensing system in the release of extracellular DNA, lipopolysaccharide, and membrane vesicles from *Pseudomonas aeruginosa*. *Japanese Journal of Infectious Diseases*, *61*(5), 375–378.
- Olsson, A. L. J., Quevedo, I. R., He, D., Basnet, M., & Tufenkji, N. (2013). Using the quartz crystal microbalance with dissipation monitoring to evaluate the size of nanoparticles deposited on surfaces. *ACS Nano*, *7*(9), 7833–7843.
- Osifo, P. O., Webster, A., van der Merwe, H., Neomagus, H. W. J. P., van der Gun, M. A., & Grant, D. M. (2008). The influence of the degree of cross-linking on the adsorption properties of chitosan beads. *Bioresource Technology*, *99*(15), 7377–7382.

- Palma, M., Deluca, D., Worgall, S., & Quadri, L. E. N. (2004). Transcriptome Analysis of the Response of *Pseudomonas aeruginosa* to Hydrogen Peroxide. *Journal of Bacteriology*, 186(1), 248–252.
- Park, H. G., Kim, J. I., Chang, K. H., Lee, B. C., Eom, I. C., Kim, P., Yeo, M. K. (2018). Trophic transfer of citrate, PVP coated silver nanomaterials, and silver ions in a paddy microcosm. *Environmental Pollution*, 235, 435–445.
- Patil, M. A., & Parikh, P. A. (2014). Investigation on likely effects of Ag, TiO₂, and ZnO nanoparticles on sewage treatment. *Bulletin of Environmental Contamination and Toxicology*, 92(1), 109–114.
- Peijnenburg, W. J. G. M., Baalousha, M., Chen, J., Chaudry, Q., Kammer, F. V. O. N. D. E. R., Kuhlbusch, T. A. J., Wang, Z. (2015). A Review of the Properties and Processes Determining the Fate of Engineered Nanomaterials in the Aquatic Environment. *Critical Reviews in Environmental Science and Technology*, 45, 2084–2134.
- Pelchovich, G., Schreiber, R., Zhuravlev, A., & Gophna, U. (2013). The contribution of common rpsL mutations in *Escherichia coli* to sensitivity to ribosome targeting antibiotics. *International Journal of Medical Microbiology*, 303(8), 558–562.
- Perrier, F., Baudrimont, M., Mornet, S., Mesmer-Dudons, N.; Lacomme, S., Etcheverria, B., Simon, O., & Feurtet-Mazel, A. (2018). Gold nanoparticle trophic transfer from natural biofilm to grazer fish. *Gold Bulletin*, 51(4), 163–173.
- Petersen, N., Hddelius, P. L., Wiseman, P. W., & Seger, O. (1993). Quantitation of Membrane Receptor Distributions by Image Correlation Spectroscopy : Concept and Application. *Biophysical Journal*, 65(September), 1135–1146.
- Peulen, T.-O., & Wilkinson, K. J. (2011). Diffusion of Nanoparticles in a Biofilm. *Environmental Science & Technology*, 45(8), 3367–3373.
- Poling-Skutvik, R., Mongcopa, K. I. S., Faraone, A., Narayanan, S., Conrad, J. C., & Krishnamoorti, R. (2016). Structure and Dynamics of Interacting Nanoparticles in Semidilute Polymer Solutions. *Macromolecules*, 49(17), 6568–6577.
- Renslow, R. S., Majors, P. D., Mclean, J. S., Fredrickson, J. K., Ahmed, B., & Beyenal, H. (2010). In Situ Effective Diffusion Coefficient Profiles in Live Biofilms Using Pulsed-Field Gradient Nuclear Magnetic Resonance. *Biotechnology and Bioengineering*, 106(6), 928–937.
- Rička, J., & Tanaka, T. (1984). Swelling of Ionic Gels: Quantitative Performance of the Donnan Theory. *Macromolecules*, 17(12), 2916–2921.

- Richter, R., Mukhopadhyay, A., & Brisson, A. (2003). Pathways of Lipid Vesicle Deposition on Solid Surfaces: A combined QCM-D and AFM Study. *Biophysical Journal*, 85(5), 3035-3047.
- Rodríguez-Suárez, J. M., Butler, C. S., Gershenson, A., & Lau, B. L. T. (2020). Heterogeneous Diffusion of Polystyrene Nanoparticles through an Alginate Matrix: The Role of Cross-linking and Particle Size. *Environmental Science & Technology*, 54(8), 5159–5166.
- Sankaran, J., Tan, N. J. H. J., But, K. P., Cohen, Y., & Rice, S. A. (2019). Single microcolony diffusion analysis in *Pseudomonas aeruginosa* biofilms. *Npj Biofilms and Microbiomes*, 35, 1–10.
- Schierz, A., Espinasse, B., Wiesner, M. R., Bisesi, J. H., Sabo-Attwood, T., & Ferguson, P. L. (2014). Fate of single walled carbon nanotubes in wetland ecosystems. *Environmental Science-Nano*, 1(6), 574–583.
- Schug, H., Isaacson, C. W., Sigg, L., Ammann, A. A., & Schirmer, K. (2014). Effect of TiO₂ Nanoparticles and UV Radiation on Extracellular Enzyme Activity of Intact Heterotrophic Biofilms. *Environmental Science & Technology*, 48(19), 11620–11628.
- Sevcu, A., El Temsah, Y. S., Joner, E. J., & Cernik, M. (2011). Oxidative stress induced in microorganisms by zero-valent iron nanoparticles. *Microbes and Environments*, 26(4), 271–281.
- Sharma, A., Gorey, B., & Casey, A. (2019). In vitro comparative cytotoxicity study of aminated polystyrene, zinc oxide and silver nanoparticles on a cervical cancer cell line. *Drug and Chemical Toxicology*, 42(1), 9–23.
- Shen, H., Tauzin, L. J., Baiyasi, R., Wang, W., Moringo, N., Shuang, B., & Landes, C. F. (2017). Single Particle Tracking: From Theory to Biophysical Applications. *Chemical Reviews*, 117(11), 7331–7376.
- Shivashankarappa, A. (2015). Study on Biological Synthesis of Cadmium Sulfide Nanoparticles by *Bacillus licheniformis* and Its Antimicrobial Properties against Food Borne Pathogens. *Nanoscience and Nanotechnology Research*, 3(1), 6–15.
- Skoog, D. A., West, D. M., & Holler, F. J. (1996). *Fundamentals of Analytical Chemistry* (seventh ed). New York, NY: Saunders College Publisher.

- Soto-Aceves, M. P., Cocotl-Yañez, M., Merino, E., Castillo-Juárez, I., Cortés-López, H., González-Pedrajo, B., Soberón-Chávez, G. (2019). Inactivation of the quorum-sensing transcriptional regulators LasR or RhlR does not suppress the expression of virulence factors and the virulence of *Pseudomonas aeruginosa* PAO1. *Microbiology (Reading, England)*, *165*(4), 425–432.
- Sprakel, J., Gucht, J. Van Der, Stuart, M. A. C., & Besseling, N. A. M. (2007). Rouse Dynamics of Colloids Bound to Polymer Networks. *Physical Review Letters, The American Physical Society*, *99*(20), 208301–208304.
- Stewart, P. S. (1998). A Review of Experimental Measurements of Effective Diffusive Permeabilities and Effective Diffusion Coefficients in Biofilms. *Biotechnology and Bioengineering*, *59*(3), 261–272.
- Stewart, P. S. (2003). Diffusion in biofilms: Why is diffusion an important process? *Journal of Bacteriology*, *185*(5), 1485–1491.
- Tang, J., Zhu, N. Y., Zhu, Y., Zamir, S. M., & Wu, Y. H. (2018). Sustainable pollutant removal by periphytic biofilm via microbial composition shifts induced by uneven distribution of CeO₂ nanoparticles. *Bioresource Technology*, *248*, 75–81.
- Taylor, S. C., Nadeau, K., Abbasi, M., Lachance, C., Nguyen, M., & Fenrich, J. (2019). The Ultimate qPCR Experiment: Producing Publication Quality, Reproducible Data the First Time. *Trends in Biotechnology*, *37*(7), 761–774.
- Theocharis, A. D., Skandalis, S. S., Gialeli, C., & Karamanos, N. K. (2016). Extracellular matrix structure. *Advanced Drug Delivery Reviews*, *97*, 4–27.
- Toole, G. A. O. (2003). *To Build a Biofilm*. *American Society for Microbiology*, *185*(9), 2687–2689.
- Vandeventer, P. E., Lin, J. S., Zwang, T. J., Nadim, A., Johal, M. S., & Niemz, A. (2012). Multiphasic DNA Adsorption to Silica Surfaces under Varying Buffer, pH, and Ionic Strength Conditions. *The Journal of Physical Chemistry*, *116*, 5661–5670.
- Vater, S. M., Weiße, S., Maleschlijski, S., Lotz, C., Koschitzki, F., Schwartz, T., Rosenhahn, A. (2014). Swimming Behavior of *Pseudomonas aeruginosa* Studied by Holographic 3D Tracking. *PLOS ONE*, *9*(1), e87765.
- Visser, A. J. W. G., & Hink, M. A. (1999). New Perspectives of Fluorescence Correlation Spectroscopy. *Journal of Fluorescence*, *9*(1), 81–87.

- von der Kammer, F., Ferguson, P. L., Holden, P. A., Masion, A., Rogers, K. R., Klaine, S. J., Unrine, J. M. (2012). Analysis of engineered nanomaterials in complex matrices (environment and biota): general considerations and conceptual case studies. *Environmental Toxicology and Chemistry*, 31(1), 32–49.
- von Moos, N., & Slaveykova, V. I. (2014). Oxidative stress induced by inorganic nanoparticles in bacteria and aquatic microalgae, state of the art and knowledge gaps. *Nanotoxicology*, 8(6), 605–630.
- Wagner, V. E., Bushnell, D., Passador, L., Brooks, A. I., & Iglewski, B. H. (2003). Microarray analysis of *Pseudomonas aeruginosa* quorum-sensing regulons: effects of growth phase and environment. *Journal of Bacteriology*, 185(7), 2080–2095.
- Wang, H., Wilksch, J. J., Chen, L., Tan, J. W. H., Strugnell, R. A., & Gee, M. L. (2016). Influence of Fimbriae on Bacterial Adhesion and Viscoelasticity and Correlations of the Two Properties with Biofilm Formation. *ACS Langmuir*, (33), 100–106.
- Westmeier, D., Hahlbrock, A., Reinhardt, C., Fröhlich-Nowoisky, J., Wessler, S., Vallet, C., Stauber, R. H. (2018). Nanomaterial–microbe cross-talk: physicochemical principles and (patho)biological consequences. *Chem. Soc. Rev.*, 47(14), 5312–5337.
- Wingender, J., Neu, T. R., & Flemming, H. C. (1999). Microbial extracellular polymeric substances: characterization, structure, and function. In *Springer*.
- Witten, J., & Ribbeck, K. (2017). The particle in the spider’s web: transport through biological hydrogels. *Nanoscale*, 9(24), 8080–8095.
- Wloka, M., Rehage, H., Flemming, H. C., & Wingender, J. (2004). Rheological properties of viscoelastic biofilm extracellular polymeric substances and comparison to the behavior of calcium alginate gels. *Colloid and Polymer Science*, 282(10), 1067–1076.
- Yaqoob, A. A., Ahmad, H., Parveen, T., Ahmad, A., & Oves, M. (2020). Recent Advances in Metal Decorated Nanomaterials and Their Various Biological Applications : A Review. *Frontiers in Chemistry, Nanoscience*, 8(May), 1–23.
- Yaroslavov, A. A., Kuchenkova, O. Y., Okuneva, I. B., Melik-nubarov, N. S., & Kozlova, N. O. (2003). Effect of polylysine on transformations and permeability of negative vesicular membranes. *1611*, 44–54.